Interplay between creep/aseismic deformation, earthquakes and fluids in fault zones, with a special emphasis on the North Anatolian fault zone, Turkey

Maor Kaduri

To cite this version:

Maor Kaduri. Interplay between creep/aseismic deformation, earthquakes and fluids in fault zones, with a special emphasis on the North Anatolian fault zone, Turkey. Earth Sciences. Université Grenoble Alpes, 2017. English. NNT : 2017GREAU040 . tel-01778040

HAL Id: tel-01778040
https://theses.hal.science/tel-01778040
Submitted on 25 Apr 2018

Communauté
UNIVERSITÉ Grenoble Alpes

THÈSE

Pour obtenir le grade de

DOCTEUR DE LA COMMUNAUTE UNIVERSITE GRENOBLE ALPES

Spécialité : **Terre Solide (CETSOL)**

Arrêté ministériel : 25 mai 2016

Présentée par

Maor Kaduri

Thèse dirigée par **François Renard**
et co-dirigée par **Jean-Pierre Gratier et Cécile Lasserre**

préparée au sein de **l'Institut des Sciences de la Terre**
dans **l'École Doctorale Terre - Univers - Environnement**

Interplay between aseismic creep deformation, earthquakes and fluids in fault zones, with a special emphasis on the North Anatolian fault zone, Turkey

Thèse soutenue publiquement le **18 décembre 2017**,
devant le jury composé de :

M. Renaud Toussaint
Président du jury, Directeur de Recherche, Université de Strasbourg, CNRS, France
Mme Renée Heilbronner
Rapporteur du jury, Professeur, University of Basel, Switzerland
M. Daniel Koehn
Rapporteur du jury, Professeur, University of Glasgow, Scotland, UK
M. François Renard
Directeur de thèse, Professeur, ISTerre, Université Grenoble Alpes, France & University of Oslo, Norway
M. Jean-Pierre Gratier
Co-Directeur de thèse, Professeur Emérite, ISTerre, Université Grenoble Alpes, France
Mme Cécile Lasserre
Co-Directeur de thèse, Chargée de Recherche, ISTerre, Université Grenoble Alpes / CNRS, France

Acknowledgments

All what I have done in this framework was made with a lot of love, patience and hope, that was accompanied and supported by lovely people. More than scientific development, this work was a great opportunity to grow in multiple directions and help me to prepare myself for the next level. This PhD project started with fieldwork that rapidly turn into fascinating adventure along the North Anatolian Fault, visiting remote places and enjoying the landscape, interaction with kind folks, and intellectual scientific challenges. Then, it continued with participation in several international conferences and six workshops in wonderful places like Israel, La Palma, Turkey, Poland, France and the North Pole, that allowed me to meet a lot of people and build a worldwide network of friends and colleagues.

Therefore, first I would like to express my deep gratitude to my supervisors: François Renard, Jean-Pierre Gratier and Cécile Lasserre for choosing me for this position, and for their support anytime and everywhere, and to Ziyadin Çakir for the fruitful collaboration that we have together. I will remember Jean-Pierre for his cosmic optimism, positive spirits, and for sharing with me his time during my research, and supporting with good advice. Thanks for teaching me how to perform successful research, and spending time with me in both field and lab. I will remember Francois for his infinite support, being there 24/7 helping with anything. Especially during the writing process, preparation for presentations in international conferences, and being a great source of inspiration. Thanks for all the discussions of motivation, and for sharing a wonderful moments in any opportunity. I will remember Cécile for her positive feedback, interesting discussions about geodesy and her support. Thanks for sharing with me your time with useful conversation. I will remember Ziyadin for being one of the greatest field chauffeurs ever! Thanks for joining us for the field work, helping to communicate with the locals and driving us to remote outcrops in middle of nowhere.

I would like to thank the jury members: Renaud Toussaint, Renée Heilbronner and Daniel Koehn for their constructive feedback.

In the lab: I would like to thanks Anne-Marie Boullier for useful discussions and for let me use her thin section scanner. Thanks to Nathaniel Findling, Valerie Magnin and

Valentina Batanova for technical support with sample preparation and XRD and EPMA analytical measurements

I would like to thank all of my international friends in Grenoble for sheering with me lovely moments, and for cheering me up during my PhD. among them: Frans, Ellie, Natalie, Margarita, Claudia, Hugo, Eric, Paul, Gosia, Ana, Ayumi, Tobias, Anca, Jacques, Ben, Thu, Clara, Josefine, Alba and many others.

Finally, I would like to thank my wonderful family for their huge hugs.

Abstract

Aseismic fault creep in the upper crust is a key deformation process along tectonic plate boundaries. It contributes to the energy budget during the seismic cycle, delaying or triggering the occurrence of large earthquakes. One of the greatest challenges is to understand which parameters control the partition between seismic and aseismic deformation in active faults, such as lithology or stress-driven transformations at all scales and how this partition evolves with time. Geological observations along the North Anatolian Fault in Turkey combined with laboratory analyses and imaging techniques performed in the present study shed new light on these mechanisms of fault creep. Moreover, the relationship between finite strain and mass change was compared with geodesy data in order to understand the evolution of these creep mechanisms since the beginning of this fault displacement.

A clear correlation is shown between shallow creep and near-surface fault gouge composition: seismic segments of the fault are mostly composed of massive limestone without clay gouges, whereas aseismic creeping segments comprising clay gouges result from a progressive change of volcanic rocks. Within these creeping zones, anastomosing cleavage develops during the first stage of deformation, leading to tectonic layering that forms a foliation, oblique at first and then sub-parallel to the fault. This foliation accommodates part of the aseismic creep by pressure solution. Consequently, the soluble minerals such as quartz and feldspars are dissolved, leading to the passive concentration of phyllosilicates in the gouges where alteration transformations by fluid flow produce low friction clay minerals. At the same time damage zones are fractured and fractures are sealed by carbonates. As a result, these mineralogical and structural transformations weaken the gouge and strengthen the damage zone leading to the change from diffuse to localized seismic-aseismic zones.

Models integrating finite strain and mass change reveal two spatial scales of strain that correspond to the alternation of two types of shear bands, with cleavages oriented either oblique or sub-parallel to the fault zone. Various total strain values were estimated in order to calculate the aseismic part of the total 80 km displacement along the locked and creeping sections. The aseismic strain fraction of the total tectonic strain in the fault depends on the fault lithology and varies from 0.002% in seismic zones made of limestone to 25±16% in the creeping zones made of volcanic rocks..

Résumé

Le fluage asismique des failles dans la croûte supérieure est un mécanisme de déformation crucial le long des limites des plaques tectoniques. Il contribue au bilan énergétique du cycle sismique, retardant ou déclenchant le développement des grands tremblements de terre. Un enjeu majeur est de comprendre quels sont les paramètres qui contrôlent la partition entre déformations sismiques et asismiques dans les failles actives tels que la lithologie ou les transformations sous contrainte à toutes échelles et comment cette partition évolue dans le temps. Des observations géologiques réalisées dans ce travail le long de la Faille Nord Anatolienne en Turquie, combinées à des analyses de laboratoire et des traitements d'images, permettent de donner un éclairage nouveau sur ces mécanismes de fluage. En plus, les relations entre déformation finie et transfert de matière ont été utilisées en parallèle avec des données géodésiques pour comprendre l'évolution de ces mécanismes de fluage depuis le début du déplacement de cette faille.

Une corrélation claire est observée entre fluage superficiel et composition des gouges de la faille : les segments sismiques sont composés de calcaires massifs sans gouge de faille argileuse alors que les segments asismiques qui fluent comprennent des gouges argileuses résultant de la transformation progressive de roches volcaniques. Dans ces zones de fluage une schistosité espacée se développe durant le premier stade de la déformation conduisant à un litage tectonique de type foliation, au début oblique puis subparallèle à la faille, qui accommode une part de la déformation asismique par dissolution cristallisation sous contrainte. En conséquence, les minéraux solubles comme le quartz et les feldspaths sont dissous conduisant à la concentration passive des phyllosilicates dans les gouges de failles qui sont ensuite altérés par des circulations de fluides produisant des minéraux argileux à faible friction. Dans le même temps les zones endommagées autour de la gouge sont fracturées et les fractures scellées par des carbonates. Ces transformations minérales et structurales amollissent les gouges de failles et durcissent les zones endommagées conduisant à une évolution de la déformation sismique – asismique de diffuse à localisée.

Des modèles qui intègrent déformation finie et transfert de matière révèlent deux échelles d'espace de la déformation qui correspondent à une alternance de deux types de bandes de cisaillement avec une schistosité soit oblique soit subparallèle à la faille. Diverses valeurs de la déformation finie ont été estimées pour calculer la proportion de déplacement asismique par rapport au déplacement total sismique et asismique de la faille (80 km). Cette proportion qui dépend de la lithologie de la zone de faille varie de 0.002% dans les zones sismiques calcaires à 25±16% dans les zones asismiques des roches volcaniques.

Table of Contents

Chapter 1

1. Introduction

Creep deformations (i.e. slow aseismic localized deformation along a fault) are commonly observed in the Earth's upper crust (Chen and Bürgmann, 2017), and take place in widespread geological phenomena such as during the seismic cycle, fault displacement, compaction of sedimentary basin, landslides, or glaciers dynamics. These creep phenomena directly or indirectly affect human activities, for example earthquake hazards, energy supply from geothermy and hydrocarbon reservoirs, and other natural resources such as mines or hydroelectric dams. Studies of creep of rocks span many discipline and approaches such as laboratory experiment, numerical modeling and geodesy, seismology and geology observations. Despite the variety of approaches and data collected, many fundamental questions remain to be unsolved on the mechanical origin of creep. The present thesis focuses on a creeping section of the North Anatolian fault in Turkey. The main goal is to characterize the interplay between creep/aseismic deformation, earthquakes and fluids in fault zones, along this fault.

The thesis contains an introduction, two chapters written as manuscripts, and a conclusion. Chapter 2 is published in the Journal of Geophysical Research; Chapter 3 is written as a manuscript to be submitted to Tectonophysics. These two chapters represent the main outcome of the present thesis.

1.1 Earthquakes and creep along the North Anatolian Fault

The North Anatolian Fault (NAF) in Turkey is one of the few unique locations worldwide that can be used as a natural laboratory to scope many aspects related to the mechanisms of earthquakes, creep and faulting. In the past decades, studies have focused on the active tectonics of this region and have revealed three key observations: (1) a sequence of nine large earthquakes that have migrated westward in the past century (Stein et al., 1997); (2) two creeping segments were detected (Hussain et al., 2016b; Kaneko et al., 2013); (3) an anticlockwise rotation of the entire Anatolian plate controls the large scale loading of the plate boundary (Reilinger et al., 2010, 1997) **(Fig. 1.1)**.

The westward progression of nine major earthquake ruptures sequence (with M>6.7) is as a result of mechanical instabilities where each earthquake has loaded a new portion of the fault, accumulated stress there, and brought it towards failure, following a cascade sequence **(Fig. 1.1)**. By extrapolating the tectonic loading to the west of Turkey, an earthquake of great magnitude is expected to nucleate close to Istanbul (13 million inhabitants) in a near future. On land two segments of the fault are creeping aseismically. The first segment, called the Ismetpasa segment, is located between the city of Gerede and the village of Mulayim. It is creeping at least since the M=7.2 earthquake of Bolu–Gerede occurred in 1944 **(Fig. 1.2).** The second creeping segment, called the Izmit segment, is located between the lake of Sapanca and extent to the west to the city of Izmit. It propagates toward to Sea of Marmara where a seismic gap has been described (Meghraoui et al., 2012). This segment is creeping aseismically since the 1999 M=7.4 Izmit earthquakes and its rate varies along strike **(Fig 1.2b-c)**.

On one hand, the existence of such creep has implications for the seismic hazard in this region. On the other hand, creep may transfer stress and control the nucleation of large earthquakes. Because, the creeping segments dissipate part of the tectonic strain energy on the fault; such mechanical behavior represents a paradigm shift on the rheology of active faults and tectonic plate boundaries. Furthermore, GPS measurements confirmed that the Anatolian plate rotates anticlockwise by an almost completely elastic deformation (Reilinger et al., 2010). The western part of the NAF experiences regional extension while the eastern part is under compressional strain, with shortening rate axes oriented at ~45° to the NAF. In addition, the orientations of the interseismic strain rate axes and sense of rotation rates are consistent with geological structures (Allmendinger et al., 2007). This effect has an impact on fault deformation in both short and long them. Therefore, identifying and characterizing creep on these fault segments, as well as understanding the deformation mechanisms at the origin of this mechanical creep behavior represents a major open question that remains to be solved. Despite the significant information provided by the geodetic data, there is a lack of knowledge concerning the mechanism of creep and on its evolution with time. The present work aims at completing this missing knowledge by the geological study of the microstructures and mineral compositions of the NAF and their evolution with time since the beginning of the NAF fault development.

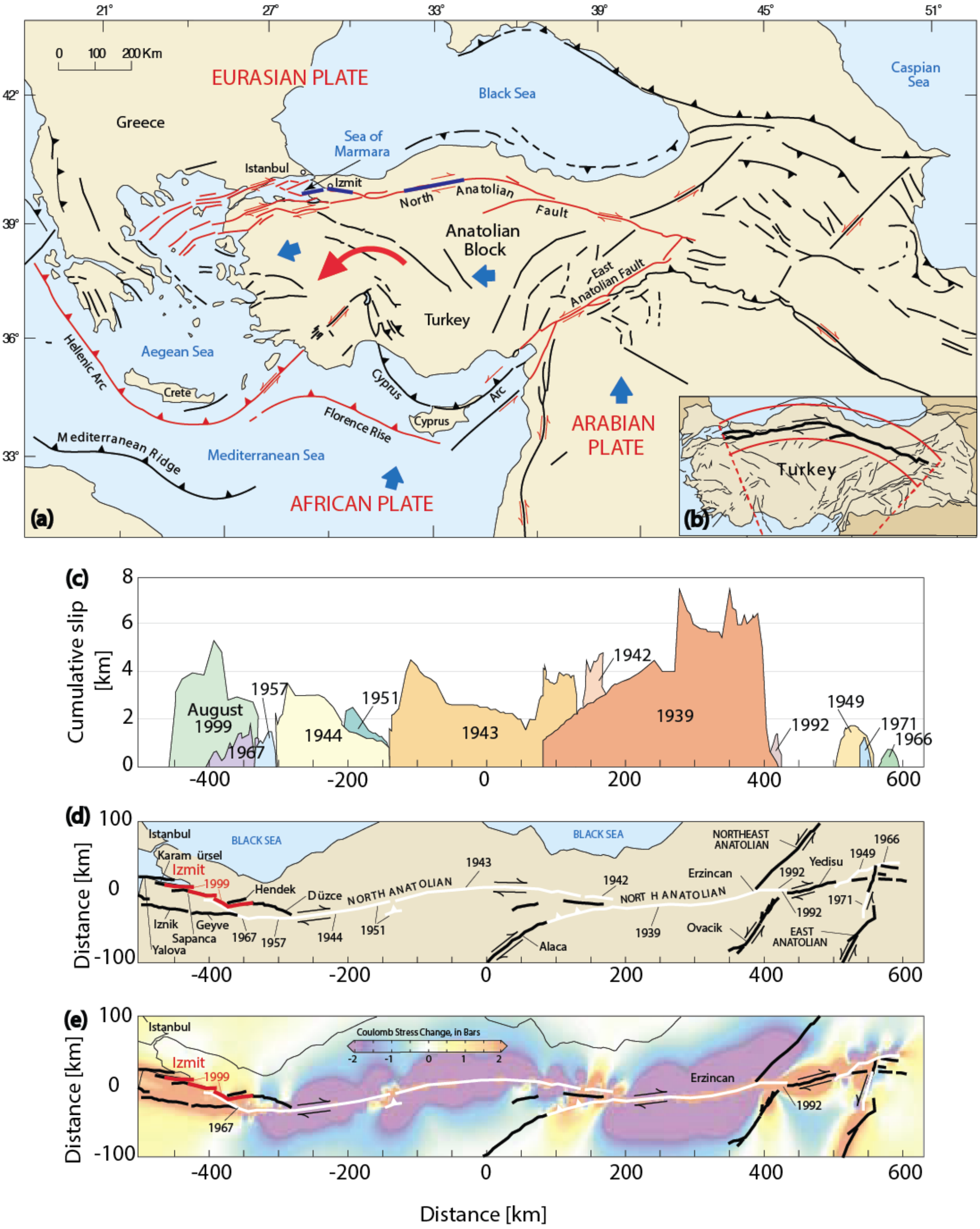

Figure.1.1 (a) Tectonic setting of the Anatolian plate. (b) Location map of the North Anatolian Fault. (c) Cumulative slip of the westward migrating earthquakes with M>6.7. (d) The location of westward migrating earthquakes along the fault. (e) Coulomb failure model that predicted the 1999 Izmit earthquake, adapted from (Holzer et al., 1999; Stein et al., 1997). The cumulative stress changes were caused by large earthquakes since 1939. An extension perpendicular to the fault combined with contraction stress along the Izmit section led to the loading of the Izmit fault where the 1999 earthquake occurred.

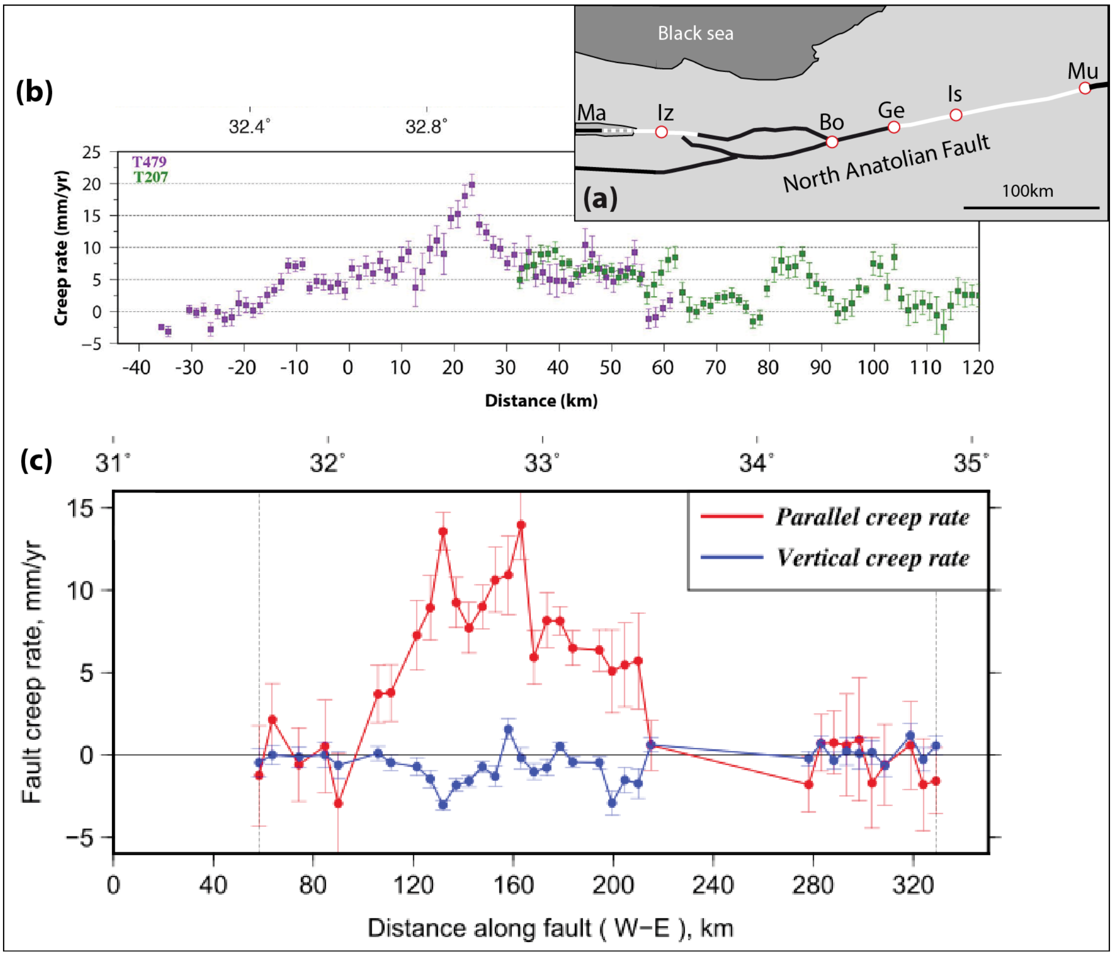

Figure. 1.2 The creep rate as function of distance along the North Anatolian Fault (a) Location of the two creeping segments (white): Izmit and Ismetpasa, Ma = Marmara Sea, Iz = Izmit, Bo = Bolu, Ge = Gerede, Is = Ismetpasa Mu = Mulayim. (b) Creep rate along the Gerede to Mulayim Ismetpasa segment (adapted from Cetin et al., 2014) (c) Creep velocity along the Ismetpasa segment described with two velocity components parallel and vertical to the fault. Adapted from Hussain et al. (2016a).

1.2 The seismic cycle and creep

Plate tectonics motion provides the forces at the origin of earthquakes and controls most of the rock deformation budget in the Earth's upper crust. Tectonic loading builds up stresses that accumulate elastic strains on faults over geological time scale which are then released during earthquakes. Usually, this phenomenon is modeled using the elastic rebound approach (Reid, 1910). Deformations during the so-called earthquake cycle can be divided into three major time steps: during, before and after an earthquake and are called the co-seismic, inter-seismic and post-seismic periods, respectively (Scholz, 2002). Creep deformations (permanent or transient) might occur at any time of those stages (Thatcher, 1993). It can also be described as a fault-weakening behavior that may generate slow earthquakes (Ikari et al., 2013).

The slip rate on a fault is a key parameter that controls its seismic potential. Fault slip rates are used as proxies to estimate recurrence times of characteristic earthquakes, which are the starting point for seismic hazard assessment. In the absence of aseismic creep, faults are locked and accumulate strain at the rate of interseismic tectonic loading. This loading, imposed by boundary conditions far away from the fault or below it, is often considered as having a constant rate. Conversely, the dissipation of the tectonic loading on faults displays a wide variety of rates: sub-shear to super-shear ruptures propagation during earthquakes, earthquake swarms, slow earthquakes and tremors, post-seismic afterslip, and aseismic creep (Beroza and Ide, 2011). Several of these mechanical behaviors may happen at different spatial positions and at different times along the same fault.

Two end-member hypotheses could explain the seismic silence of several segments along active faults. Firstly, it can be hypothesized that slip along such segments occurs entirely by aseismic creep. Secondly, these segments may be completely locked and thus represent an earthquake or 'seismic' gap. In many fault zones around the world, geodetic data have been used to decipher between these alternatives. Remote sensing and geodesy have proved being major players to reveal that large strike-slip faults could creep during inter-seismic periods **(Fig. 1.3)**, as it has already been evidenced in subduction zones (Rogers and Dragert, 2003).

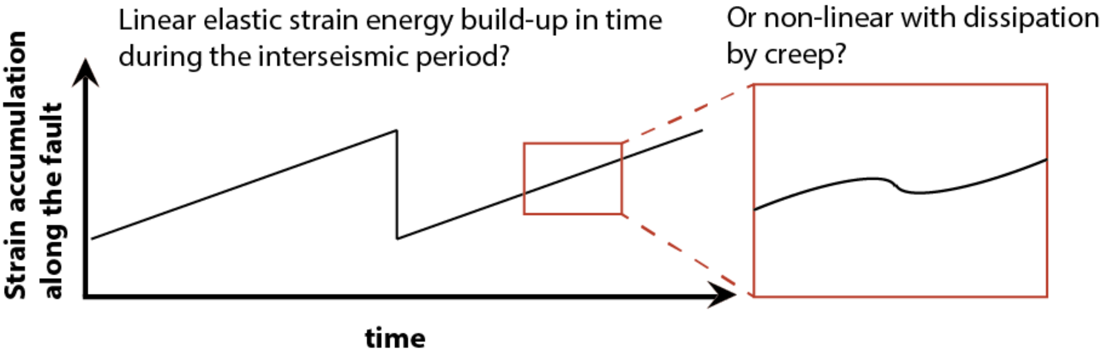

Figure.1.3 During the interseismic period a fault may either be fully elastically loaded by tectonic forces or some of this strain energy may be dissipated by creep. In the present project, we aim at studying the mechanism of creep from a geological approach along the North Anatolian Fault, Turkey. Figure courtesy of Baptiste Rousset.

1.3 The implication of fault analysis from geodetic data to shear zone analysis on the mechanism of creep

There are possibly three key mechanisms known for creep mechanisms: (1) Friction along interfaces (e.g. grains, fractures), is described by the phenomenological rate-and-state friction laws (Dieterich, 1972; Ruina, 1983), and experiment on rocks and fault gouge (Marone, 1998) have shown an effect of velocity weakening (Scholz, 1998) which is known to be affected by mineral composition (Carpenter et al., 2016). (2) Pressure solution creep at microscopic scale is studied from both field data and slow experiments (Gratier et al., 2015, 2011), or numerical micro-models (Bos, 2002). (3) Brittle creep is strongly dependent on preexisting microstructures and the degree of anisotropy (Rostom et al., 2013; Røyne et al., 2011). Despite the large amount knowledge on those topics, the effect of those mechanisms as well as the significance of them as physical processes related to active faults remain unsolved. An important aim of my research is to shed light on the complexity of the mechanism related to aseismic creep along the NAF based on natural data from rocks.

In **Chapter 2**, a major goal is to acquire a better description of the microstructures that are associated with aseismic creep, and to outline the effects of rock mineralogy transformations along the NAF, which support the concept of creep formed by velocity wakening (Scholz, 1998). Research performed on others faults like the San Andreas Fault (Zoback et al., 2010) allowed to study permanently creeping weak clay gouge (Lockner et al., 2011), and microstructures that formed by pressure solution creep (Gratier et al., 2011). The same approach was followed on other creeping faults as well (e.g. Thomas et al., 2014). In the present study, I have acquired a better description of the deformation along the NAF in places where I can compare the composition of the fault rocks in relation with their seismic or aseismic behavior. I have shown the crucial effect of the lithology on the development of creep processes and I have reconstructed the evolution of a creep zone from the beginning of an active shear zone to the present day localized fault zone.

Then in order to better understand the partition between seismic and aseismic deformation and its evolution with time in the upper crust **(Chapter 3)** I have made strain measurements and I have evaluated mass transfer within the fault zone. I have also established the relationship between the creep strain rate measured near the surface by geodesy with the creep rate deduced from geological observations. On one hand, geological field data allows investigating creep deformation at small spatial scale that would not be reached from geodesy. On the other hand, geodetic data provide time series on short time scales. In the present study I demonstrate that it is possible to combine geodetic strain rate (recent strain) and strain measured from microstructures (representing a snapshot of the geological strain) collected from the fault. The results achieved allow quantifying the part of aseismic deformation relative to the total displacement that depends on the lithology and its evolution with time since the beginning of the fault displacement.

References

Allmendinger, R.W., Reilinger, R., Loveless, J., 2007. Strain and rotation rate from GPS in Tibet, Anatolia, and the Altiplano. Tectonics 26, 1–18. doi:10.1029/2006TC002030

Beroza, G.C., Ide, S., 2011. Slow Earthquakes and Nonvolcanic Tremor. Annu. Rev. Earth Planet. Sci. 39, 271–296. doi:10.1146/annurev-earth-040809-152531

Bos, B., 2002. Frictional-viscous flow of phyllosilicate-bearing fault rock: Microphysical model and implications for crustal strength profiles. J. Geophys. Res. 107. doi:10.1029/2001JB000301

Carpenter, B.M., Ikari, M.J., Marone, C., 2016. Laboratory observations of time-dependent frictional strengthening and stress relaxation in natural and synthetic fault gouges. J. Geophys. Res. Solid Earth 121, 1183-1201. doi:10.1002/2015JB012136

Cetin, E., Cakir, Z., Meghraoui, M., Ergintav, S., Akoglu, A.M., 2014. Extent and distribution of aseismic slip on the Ismetpa?a segment of the North Anatolian Fault (Turkey) from Persistent Scatterer InSAR. Geochemistry, Geophys. Geosystems 15, 2883–2894. doi:10.1002/2014GC005307

Chen, K.H., Bürgmann, R., 2017. Creeping faults: Good news, bad news? Rev. Geophys. 1–5. doi:10.1002/2017RG000565

Dieterich, J.H., 1972. Time-dependent friction in rocks. J. Geophys. Res. 77, 3690–3697. doi:10.1029/JB077i020p03690

Gratier, J.-P., Noiriel, C., Renard, F., 2015. Experimental evidence for rock layering development by pressure solution. Geology 43, 871–874. doi:10.1130/G36713.1

Gratier, J.P., Richard, J., Renard, F., Mittempergher, S., Doan, M.L., Di Toro, G., Hadizadeh, J., Boullier, A. M., 2011. Aseismic sliding of active faults by pressure solution creep: Evidence from the San Andreas Fault Observatory at Depth. Geology 39, 1131–1134. doi:10.1130/G32073.1

Holzer, T.L., Barka, A.A., Carver, D., Celebi, M., Toprak, S., 1999. Implications for Earthquake Risk Reduction in the United States from the Kocaeli, Turkey, Earthquake. U.S. Geol. Surv. Circ. 1193, 1–65.

Hussain, E., Hooper, A., Wright, T.J., Walters, R.J., Bekaert, D.P.S., 2016a. Interseismic strain accumulation across the central North Anatolian Fault from iteratively unwrapped InSAR measurements. J. Geophys. Res. Solid Earth 121, 9000–9019. doi:10.1002/2016JB013108

Hussain, E., Wright, T.J., Walters, R.J., Bekaert, D., Hooper, A., Houseman, G.A., 2016b. Geodetic observations of postseismic creep in the decade after the 1999 Izmit earthquake, Turkey: Implications for a shallow slip deficit. J. Geophys. Res. Solid Earth 121, 2980–3001. doi:10.1002/2015JB012737

Ikari, M.J., Marone, C., Saffer, D.M., Kopf, A.J., 2013. Slip weakening as a mechanism for slow earthquakes. Nat. Geosci. 6, 468–472. doi:10.1038/ngeo1818

Kaneko, Y., Fialko, Y., Sandwell, D.T., Tong, X., Furuya, M., 2013. Interseismic deformation and creep along the central section of the North Anatolian Fault (Turkey): InSAR observations and implications for rate-and-state friction properties. J. Geophys. Res. Solid Earth 118, 316–331. doi:10.1029/2012JB009661

Lockner, D. A, Morrow, C., Moore, D., Hickman, S., 2011. Low strength of deep San Andreas fault gouge from SAFOD core. Nature 472, 82–85. doi:10.1038/nature09927

Marone, C., 1998. The effect of loading rate on static friction and the rate of fault healing during the earthquake cycle. Nature 69–72.

Meghraoui, M., Aksoy, M.E., Akyüz, H.S., Ferry, M., Dikbaş, A., Altunel, E., 2012. Paleoseismology of the North Anatolian Fault at Güzelköy (Ganos segment, Turkey): Size and recurrence time of earthquake ruptures west of the Sea of Marmara. Geochemistry, Geophys. Geosystems, 13, Q04005. doi:10.1029/2011GC003960

Reilinger, R., McClusky, S., Paradissis, D., Ergintav, S., Vernant, P., 2010. Geodetic constraints on the tectonic evolution of the Aegean region and strain accumulation along the Hellenic subduction zone. Tectonophysics 488, 22–30. doi:10.1016/j.tecto.2009.05.027

Reilinger, R.E., McClusky, S.C., Oral, M.B., King, R.W., Toksoz, M.N., Barka, A.A., Kinik, I., Lenk, O., Sanli, I., 1997. Global Positioning System measurements of present-day crustal movements in the Arabia-Africa-Eurasia plate collision zone. J. Geophys. Res. Solid Earth 102, 9983–9999. doi:10.1029/96JB03736

Reid, H. F. (1910). The mechanics of the earthquake (Vol. 2, pp. 1-192). Carnegie institution of Washington.

Rogers, G., Dragert, H., 2003. Episodic Tremor and Slip on the Cascadia Subduction Zone : The Chatter of Silent Slip 300, 1942–1943. doi:10.1126/science.1084783

Rostom, F., Røyne, A., Dysthe, D.K., Renard, F., 2013. Effect of fluid salinity on subcritical crack propagation in calcite. Tectonophysics 583, 68–75. doi:10.1016/j.tecto.2012.10.023

Røyne, A., Bisschop, J., Dysthe, D.K., 2011. Experimental investigation of surface energy and subcritical crack growth in calcite. J. Geophys. Res. 116, B04204. doi:10.1029/2010JB008033

Ruina, A., 1983. Slip instability and state variable friction laws. J. Geophys. Res. Solid Earth 88, 10359–10370. doi:10.1029/JB088iB12p10359

Savage, J.C., 1975. Comment on "An analysis of strain accumulation on a strike slip fault" by D. L. Turcotte and D. A. Spence 80, 4111–4114. doi:10.1029/JB080i029p04111

Scholz, C.H., 2002. The Mechanics of Earthquake Faulting. doi:10.1017/CBO9780511818516

Scholz, C.H., 1998. Earthquakes and friction laws. Nature 391, 37–42. doi:10.1038/34097

Stein, R.S., Barka, A. a, Dieterich, J.H., 1997. Progressive failure on the North Anatolian fault since 1939 by earthquake stress triggering. Geophys. J. Int. 128, 594–604. doi:10.1111/j.1365-246X.1997.tb05321.x

Thatcher, W., 1993. The earthquake cycle and its role in the long-term deformation of the continental lithosphere, Annali di Geofisica, 26(2), 13-24.

Thomas, M.Y., Avouac, J.-P., Gratier, J.-P., Lee, J.-C., 2014. Lithological control on the deformation mechanism and the mode of fault slip on the Longitudinal Valley Fault, Taiwan. Tectonophysics 632, 48–63. doi:10.1016/j.tecto.2014.05.038

Zoback, M., Hickman, S., Ellsworth, W., 2010. Scientific Drilling Into the San Andreas Fault Zone. Eos, Trans. Am. Geophys. Union 91, 197. doi:10.1029/2010EO220001.

Chapter 2

2. The implications of fault zone transformation on aseismic creep: example of the North Anatolian Fault, Turkey

AGU PUBLICATIONS
JGR
Journal of Geophysical Research: Solid Earth

RESEARCH ARTICLE
10.1002/2016JB013803

The implications of fault zone transformation on aseismic creep: Example of the North Anatolian Fault, Turkey

Maor Kaduri[1], **Jean-Pierre Gratier**[1], **François Renard**[1,2], **Ziyadin Çakir**[3], **and Cécile Lasserre**[1]

[1]ISTerre, University Grenoble Alpes and CNRS, Grenoble, France, [2]Department of Geosciences, Physics of Geological Processes, University of Oslo, Oslo, Norway, [3]Department of Geology, Istanbul Technical University, Istanbul, Turkey

Abstract Aseismic creep is observed at surface along several segments of the North Anatolian right-lateral active fault in Turkey, a major plate boundary between Eurasia and Anatolia. Identifying the mechanisms that control creep and their temporal and spatial change represents a major challenge for predicting the mechanical evolution of active faults, the interplay between creep and earthquakes, and the link between short-term observations from geodesy and the long-term fault zone evolution. We combine geological observations, laboratory analyses, and imaging techniques, shedding new light on the mechanism of fault creep along the North Anatolian Fault (NAF) and its time-dependent change. A clear correlation is shown between shallow creep and near-surface fault gouge composition: locked segments of the NAF are mostly composed of massive limestones without clay gouges, whereas creeping segments comprise clay gouges that contain low-friction minerals. Such fault gouges appear to result from a progressive change of initial volcanic host rocks during their deformation. Anastomosing cleavage develops during the first stage of displacement, leading to layering, oblique at first and then subparallel to the fault, which accommodates part of the aseismic creep by pressure solution. Soluble minerals are dissolved, leading to passive concentration of phyllosilicates in the gouges where alteration transformations by fluid flow produce low friction minerals. At the same time damage zones are fractured and fractures are sealed by carbonates. As a result, these mineralogical and structural transformations weaken the gouge and strengthen the damage zone leading to the change from diffuse to localized seismic-aseismic zones.

Key Points:

- Massive limestones deform seismically; aseismic creep is observed only in volcanic rocks with clay gouges
- Clay gouges result from transformations of rocks during seismic and aseismic deformation
- Aseismic creep mechanism is a combination of pressure solution viscous creep and grain frictional sliding

Supporting Information:

- Supporting Information S1

Correspondence to:
F. Renard,
francois.renard@geo.uio.no

Citation:
Kaduri, M., J.-P. Gratier, F. Renard, Z. Çakir, and C. Lasserre (2017), The implications of fault zone transformation on aseismic creep: Example of the North Anatolian Fault, Turkey, *J. Geophys. Res. Solid Earth*, *122*, doi:10.1002/2016JB013803.

Received 29 NOV 2016
Accepted 8 MAY 2017
Accepted article online 10 MAY 2017

1. Introduction

Active shallow aseismic displacement, also called creep, has been measured on several major continental faults such as the San Andreas Fault in California [*Titus et al*., 2006; *de Michele et al*., 2011], the Haiyuan Fault in China [*Jolivet et al*., 2012, 2013, 2015], the El-Pilar Fault in Venezuela [*Jouanne et al*., 2011; *Pousse Beltram et al*., 2016], the Longitudinal Valley Fault in Taiwan [*Thomas et al*., 2014b], the Chaman Fault in Pakistan [*Fattahi and Amelung*, 2016], and the North Anatolian Fault in Turkey along the Ismetpasa segment [*Ambraseys*, 1970*; Barka*, 1992*; Çakir et al*., 2005*; Kaneko et al*., 2013*; Cetin et al*., 2014]. Creep behavior can be permanent, or it can appear after a major earthquake and be called afterslip or postseismic creep, as measured, for example, from slow surface displacements over a period of several years following the 1999 Izmit earthquake in Turkey [*Çakir et al*., 2003; *Hearn et al*., 2009, *Hussain et al*., 2016a].

Creep, in addition to silent slow slip events, tremors, and repeating earthquakes, sheds new light on the dynamics of the Earth's continental crust at a global scale and on the seismic cycle [*Peng and Gomberg*, 2010*; Beroza and Ide*, 2011*; Barbot et al*., 2012]. The existence of physical and geological links between all these phenomena is strongly suggested by observations of foreshocks and repeating earthquakes prior to some large earthquakes [*Bouchon et al*., 2011, 2013]. These observations are interpreted as resulting from the nucleation phase, involving creep on or around the future rupture area. Because small or slow earthquakes and creep processes transfer stress between different portions of the fault, relaxing or loading them [*Stein et al*., 1997], they could trigger the nucleation of large earthquakes.

The North Anatolian Fault (NAF) is a continental right-lateral fault that separates the Anatolian Plate to the south and the Eurasian Plate to the north (Figure 1). Its main active trace has a sharp morphological expression. Large-scale structural right-lateral offsets have been estimated, as that of the Pontide suture [*Şengör et al*., 1985; *Hubert-Ferrari*, 2002] or around the Sea of Marmara [*Barka*, 1992*; Le Pichon*, 2003*; Armijo et al*., 2005*; Şengör et al*., 2005; *Akbayram et al*., 2016] and in the western part of the central bend [*Hubert-Ferrari*, 2002]. In western Turkey, slip between Anatolia and Eurasia is partitioned on several fault branches

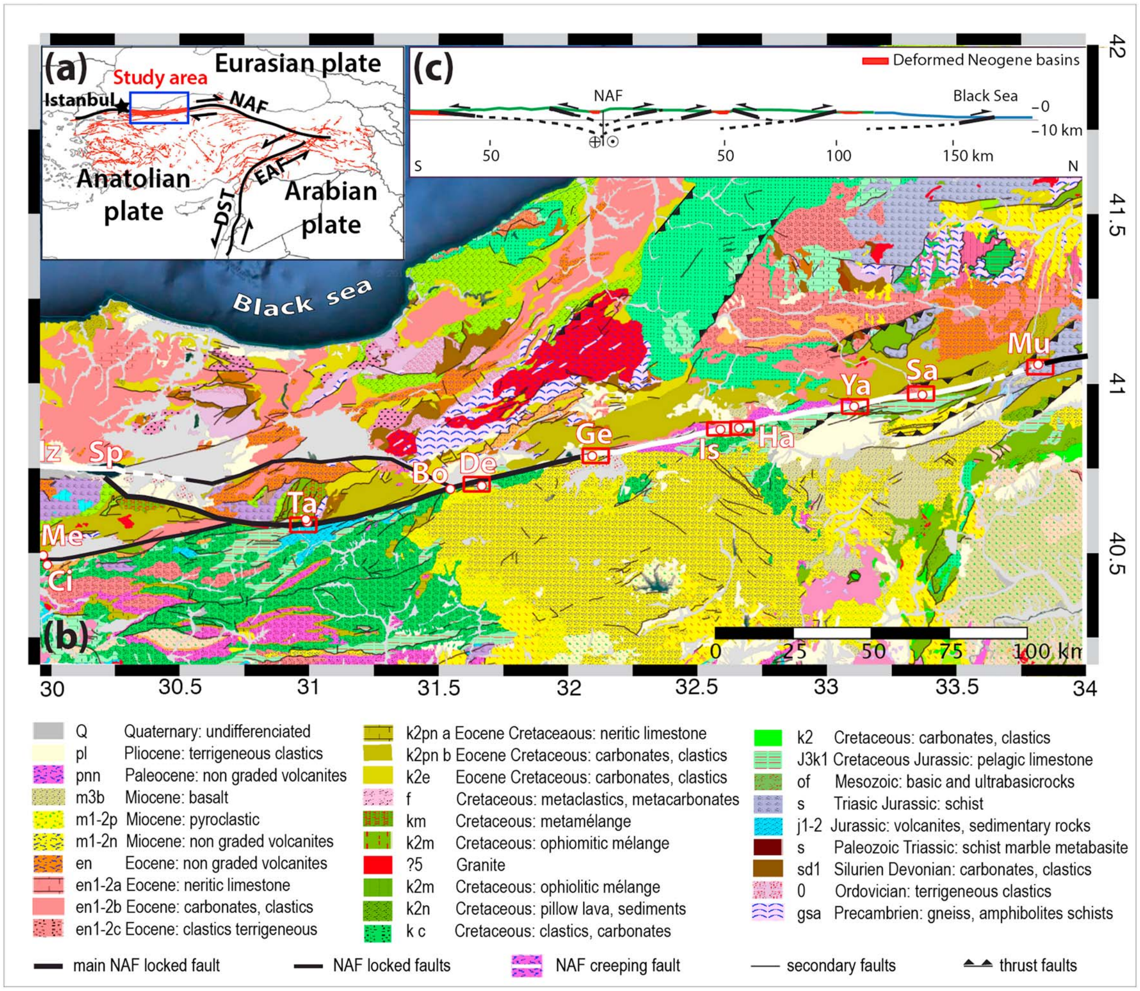

Figure 1. Structural and geological map of the study area along the North Anatolian Fault: (a) Location map of Turkey. The study area, east of Istanbul, is marked by a blue rectangle with the studied fault segment in red [*Emre et al*., 2013]. NAF: North Anatolian Fault, EAF: East Anatolian Fault, and DST: Dead-Sea Transform fault segment. (b) Geological map of the study area with names and outcrop locations indicated as white circles: Me = Mekece, Ci = Ciciler, Iz = Izmit, Sp = Sapanca lake, Ta = Taskesti, Bo = Bolu, De = Demirciler, Ge = Gerede, Is = Ismetpasa, Ha = Hamamli, Ya = Yazioren, Sa = Sarialan, and Mu = Mülayim. The creeping segments of Izmit (west) and Ismetpasa (east) are marked in white [*Çakir et al*., 2005; *Cetin et al*., 2014]. The locked segments are black. Small red rectangles contour local geological maps shown in the following figures to describe outcrops with referenced names. The GPS coordinates of these outcrops are given in the supporting information. The regional geological map is extracted from an interactive map of the Turkish geological survey [*Akbaş et al*., 2016] available on http://yerbilimleri.mta.gov.tr/anasayfa.aspx. The legend gives the lithology of the formations that are cut by the studied NAF segment. (c) Schematic N-S cross section along the eastern boundary of the map, adapted from [*Yildirim et al*., 2011].

[*Ambraseys*, 1970; *Hubert-Ferrari*, 2002*; Flerit et al*., 2003]. Together, they amount to about 80 km total displacement [*Armijo et al*., 1999, 2000]. This cumulative displacement along the North Anatolian Fault is in agreement with the analysis of major river deflections [*Barka*, 1992*; Hubert-Ferrari*, 2002*; Şengör et al*., 2005]. Furthermore, measuring and dating stream channel and alluvial terraces offsets lead to Quaternary slip rate estimates of 18 mm/yr to 20.5 mm/yr [*Hubert-Ferrari*, 2002; *Kozaci et al*., 2007, 2009*; Gasperini et al*., 2011*; Meghraoui et al*., 2012; *Grall et al*., 2013], which can be compared to the present-day slip rate estimated from rigid block modeling of GPS measurements of about 17 to 27 mm/yr [*Barka and Reilinger*, 1997*; Straub et al*., 1997; *McClusky et al*., 2000; *Meade et al*., 2002; *Reilinger et al*., 2006, 2010]. Whether the variability in the fault slip rate estimates may be explained by slip partitioning between the different fault branches is still debated. With a mean slip rate of 20 mm/yr the displacement could have taken about 4 Ma to accumulate 80 km of displacement.

A striking feature of the North Anatolian Fault is the existence of different segments that show differing slip behaviors indicative of differing mechanical behaviors. Some segments remain locked and are prone to major earthquakes [*Ambraseys*, 1970*; Stein et al*., 1997], while others display active aseismic or postseismic creep measured using radar interferometry in particular [*Kaneko et al.*, 2013; *Cetin et al.*, 2014; *Hussain et al.*, 2016a; *Rousset et al.*, 2016]. According to *Kondo et al.* [2010], the Bolu-Gerede locked segment shows a recurrence time of earthquakes of about 330 years. Two inland segments of the North Anatolian Fault show aseismic creep [*Ambraseys*, 1970; *Çakir et al.*, 2005, 2012; *Kaneko et al.*, 2013; *Cetin et al.*, 2014; *Hussain et al.*, 2016b] (Figure 1). The 50 km long Izmit segment has been creeping since the 1999 earthquake [*Çakir et al.*, 2012]. The fault segment near Ismetpasa has been creeping since at least the 1950s, possibly since the 1944 (M_w 7.2) and/or 1951 (M_w 6.9) earthquakes [*Çakir et al.*, 2005] **(**Figure 1). Interferometric synthetic aperture radar (InSAR) studies determined the length of the Ismetpasa creeping segment as ~100 km, with a creep depth of ~7 km and an ~8 mm/yr creep rate [*Çakir et al.*, 2005; *Kaneko et al.*, 2013; *Cetin et al.*, 2014; *Hussain et al.*, 2016b]. This rate has been decreasing since the initial observations (1957–1969), in favor of a postseismic creep interpretation. The surface creep rate today is in overall less than half of the annual average rate of relative plate velocity, indicating that significant stress is still being accumulated on the fault [*Hussain et al.*, 2016b]. Recent creepmeter and time-lapse InSAR studies also showed that creep occurs as bursts, with a depth up to 6 ± 3 km [*Rousset et al.*, 2016; *Bilham et al.*, 2016].

InSAR studies show that there is little differential vertical motion along the NAF in the Ismetpasa region [*Hussain et al.*, 2016b]. However, thrust faults subparallel to the NAF that deform Neogene deposits are seen on the geological map and the cross section attesting of regional uplift (Figure 1). Geomorphological field observations of uplifted marine deposits also show that the NAF surface and fault rocks are uplifted versus the abyssal plain of the Black Sea with associated erosional processes. This late Neogene and active orogenic uplift is associated with the NAF displacement [*Yildirim et al.*, 2011]. This means that outcropping rocks in the fault zone may gather samples deformed at various depths, from the surface to several kilometers deep.

From these field observations, the detailed mechanisms of creep at the scale of the fault zone remain to be understood. At least three deformation processes have been identified to explain a creep rheology of the rocks at low temperature and moderate stress in the upper crust: (1) pressure solution stress-driven viscous creep [*Elliott*, 1973; *Rutter*, 1976; *Gratier et al.*, 2011, 2013b], (2) brittle creep [*Atkinson*, 1984; *Perfettini and Avouac*, 2004; *Brantut et al.*, 2013], and (3) velocity-strengthening grain frictional sliding [*Marone*, 1998] where weak minerals are involved [*Moore and Rymer*, 2007; *Carpenter et al.*, 2011a; *Lockner et al.*, 2011]. Mixed friction and viscous creep behavior has also been proposed [*Bos and Spiers*, 2002]. These mechanisms depend to a variable degree on thermodynamic parameters (pressure and temperature), rock microstructure (size and shape of the grains), and mineral composition. Which of these three mechanisms is dominant in creeping fault zones is an open question.

The aims of this study are to characterize fault zone outcrops along creeping versus locked segments along the North Anatolian Fault and to identify the deformation mechanisms at the origin of creep. For this purpose, a detailed microstructural and mineralogical study of fault outcrops along the North Anatolian Fault is performed in order to answer the following questions: (1) Do the creeping segments correspond to specific geological and structural features along the fault? (2) What are the mechanisms of creep (friction versus stress-driven mass transfer), and how are the nature of rocks and fluids and the conditions of the deformation linked to these mechanisms? And (3) more generally, are the fault zone petrophysical properties different along the creeping zones versus the locked ones, and do these properties change with time?

2. Approach and Methodology

2.1. Fault Zone Outcrops

The present work studies the fault rock development and character of the North Anatolian Fault between Ciciler and Sapanca in the west to Mülayim in the east (Figure 1). This portion of the fault covers several segments, including the creeping segment of Ismetpasa [*Çakir et al.*, 2005], from Gerede to Mülayim, and the locked segments from Sapanca and Ciciler to Gerede (Figure 1). To analyze the anatomy of the fault zones at the outcrop scale along these segments, field studies were performed that systematically followed the fault zone over a distance of 270 km. All outcrops that were located on the fault within 1 km of any tarred or accessible dirt road were explored. For this purpose, satellite images and the map of the faults provided by the Turkish geological survey [*Herece and Akay*, 2003] were used and dirt roads identified using Google Earth. More than 30 sites along both locked and creeping segments of the fault were visited where geomorphological evidence of the active fault can be identified (fresh outcrops, push-ups, offsets of streams, offsets of lines of trees or walls, and sets of aligned springs or ponds). Seventeen well-preserved outcrops have been selected from these sites based on two criteria: (1) the fault zone is not fully covered by Quaternary sediments and (2) an outcropping cross section of the fault zone can be identified, with visible damage zone and core of the fault and in several cases the initial host rock as well. A dozen of the most representative outcrops are presented here (Figure 1b). Their GPS coordinates are given in the supporting information. From these outcrops, 90 oriented hand samples were collected and analyzed in the laboratory and 130 thin sections of rock samples were prepared for mineralogical, geochemical, and microstructural analyses. Several samples were collected from initial rock, damaged rock, and fault gouge: each type of rock was sampled in several places in order to determine the spatial variation of the mineralogy within the fault zone.

2.2. Sampling Procedure

In places where the samples were sufficiently cohesive, they were first oriented on the outcrop, localized with respect to their distance from the fault core, and then sampled with a hammer. In other places along the creeping segment, the rocks in the fault zone were very fragile due to both high damaging and high content of weak minerals. As a result, these rocks had a very low cohesion and sampling was challenging. We decided to sample them directly in the field using hollow metal tubes (5 cm internal diameter) that could be hammered directly into the gouge. The 20 cm long core samples were extracted. These samples were then immediately placed in a plastic bag that was sealed to avoid water evaporation. In this way, the internal structure of the gouge can be preserved. All tubes were oriented on the outcrop and labeled accordingly. Samples of damage zones and initial rocks, located up to a hundred meters from the fault core, were also collected. In order to prepare oriented thin sections, the samples should be cut without compromising the microstructures. The less cohesive samples were consolidated using PRESI epoxy resin diluted with 10% methanol in vacuum. These samples in their epoxy bath were placed in a vacuum glass chamber for 1 day. Using this procedure, the epoxy can access large and small pores and consolidate the sample sufficiently for thin section preparation without compromising chemical and structural analyses.

2.3. Chemical, Mineralogical, and Microstructural Analyses of Fault Samples

The mineralogy, chemistry, and microstructures were characterized and quantified using a series of complementary analytical methods. The chemical compositions were obtained at various scales leading to maps of oxide contents at various sizes: X-ray fluorescence imaging (XRF) at sizes of several millimeters to centimeters, scanning electron microscopy (SEM-EDS) at sizes of several millimeters, and electron microprobe (EPMA) at sizes of several hundreds of microns with single points of local analysis (microns sizes). The mineralogical composition can be calculated if the minerals present in the sample are known. Such information was obtained from powder X-ray diffraction analyses that have been done at hand sample sizes (millimeters to centimeters and minerals were quantified using Rietvel refinement procedure [*Doebelin and Kleeberg*, 2015]). Mineral composition was then obtained either from internal programs (EPMA) or by the use of the XmapTool software [*Lanari et al.*, 2014] for the other analyses. The microstructures were obtained from optical and SEM imaging. Details on analytical techniques are given in the supporting information.

When comparing composition contents between initial and deformed rocks, a distinction was made between soluble and insoluble minerals by reference to the abundant bibliography (see a review in *Gratier et al.* [2013a]). The most soluble minerals such as quartz, feldspars, calcite, and dolomite are considered to be mobile and are transported in solution during the deformation processes either by diffusion or by advection. Some of these minerals (quartz and carbonates) fill fractures. The most insoluble minerals such as phyllosilicates, Ti and Fe oxides, are considered to be nonmobile and are passively concentrated into the deformed rock. In order to best visualize the mass transfer processes, heterogeneously deformed zones are divided into homogeneous areas that are then sorted according to their soluble and insoluble mineral contents, respectively *Gratier et al.* [2013a]. This can be done at all scales from the outcrop to the grain size.

3. Results

3.1. Characteristics of the Locked Segments

Along the presently locked studied segments, all the fault outcrops we found in small or big quarries, from Sapanca Lake to Gerede, crosscut limestone lithology (Figure 1b). The total right-lateral fault offset of reference geological formations, along the Bolu-to-Mülayim NAF fault segment, is about 80 km. East of Bolu the

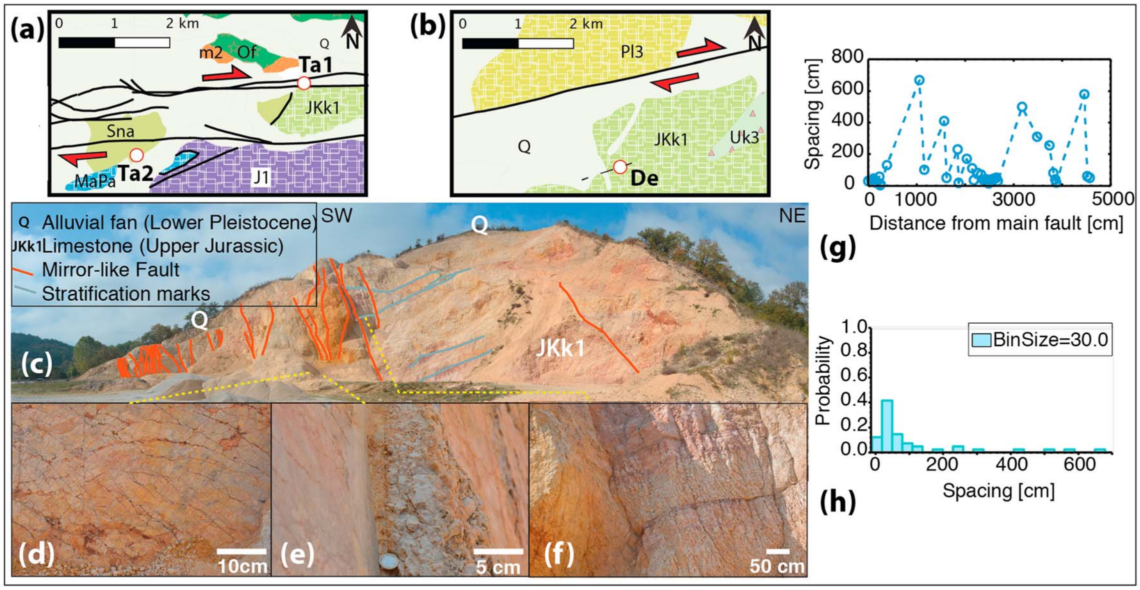

Figure 2. Taskesti and Dermirciler outcrops location and Taşkesti-1 fault structure; (a and b) Taskesti and Demirciler geological maps respectively; see lithology in Figure 7e. (c) The Taskesti-1 fault zone is located in an abandoned quarry, and numerous localized slip surfaces can be seen. (d) Mirror-like slip surface. (e) Limestone gouge. (f) Damage zone (mainly by fracturing). (g) Spacing between the slip surfaces as a function of the distance from the main fault. (h) Probability density function of the distances between slip surfaces with the most frequent distance close to 45 cm (see the supporting information for detailed method).

NAF splits into several branches with various offsets: 50 km along the Taskesti-Sapanca main segment and 30 km along the Taskesti-Ciciler and North-Taskesti segments [*Akbayram et al*., 2016]. The Sapanca-to-Gerede fault segment puts in contact mostly carbonates-clastics and limestone massifs. Its northern compartment comprises carbonates-clastics and limestone massif, more than 5 km thick [*Göncüoglu*, 2010], that are seen along about 90% of the total 200 km long fault segment only locally interrupted by NE-SW trending stripes of Paleozoic schist and marble as well as Eocene volcanic rocks extending over distance of about 10% of the total along-the-fault length. The southern compartment of this Sapanca-to-Gerede fault segment comprises a huge massif of Eocene to Jurassic carbonates-clastics and limestones, also several kilometers thick, extending along about 90% of the 200 km long fault segment only locally interrupted by some NE-SW trending stripes of volcanic rocks extending over distance of about 10% of the along-the-fault length. The same 90% carbonates-clastics and limestones versus 10% volcanic rocks ratio is seen along the Taskesti-Ciciler branch (comprising the Mekece and Ciciler outcrops) Figure 1. In terms of deformation style the locked fault segment shows localized deformation structures such as cataclastic bands, mirror-like slip surfaces, gouges of various width, horizontal striaes, tectonic stylolites, and anastomosing slip surfaces.

3.1.1. Taşkesti Outcrop

The main outcrop (Ta1, Figure 2a) is located east of the Taşkesti settlement (Figure 1) in an abandoned quarry in massive limestone (JKk1). The fault zone is oriented parallel to the main trend of the North Anatolian Fault. It is made up of a succession of several subparallel main slip surfaces, with near-horizontal striaes, embedded in damage zones (Figure 2c). The outcrop is located along the 1967 earthquake rupture, and some of the slip surfaces may be related to this event. Of the ~200 m wide damage zone, only an ~50 m wide section is freshly outcropping, with arrays of subparallel near-vertical fault surfaces and 4–6 m wide near-vertical cataclastic deformation zones crosscutting the limestone (Figure 2c). Figure 2d shows examples of mirror fault surfaces with fracture networks. Most of the faults are associated with gouges made of fine-grained calcite powder with widths measured in millimeters to centimeters (Figure 2e). Their clay contents are always very low (less than 5%) and not very different from the host rocks (less than 2%). In thin sections, mirror faults show much higher contents in Fe oxides than in the host rocks. The spacing of the slip surfaces plotted as a function of distance from the main fault shows two zones with a high density of slip surfaces (Figure 2g). The probability density function of the discretized fracture spacing (bin size = 30 cm) shows lognormal distribution, and the most frequent spacing distance is 45 cm (Figure 2h). Two main types of deformation microstructures are

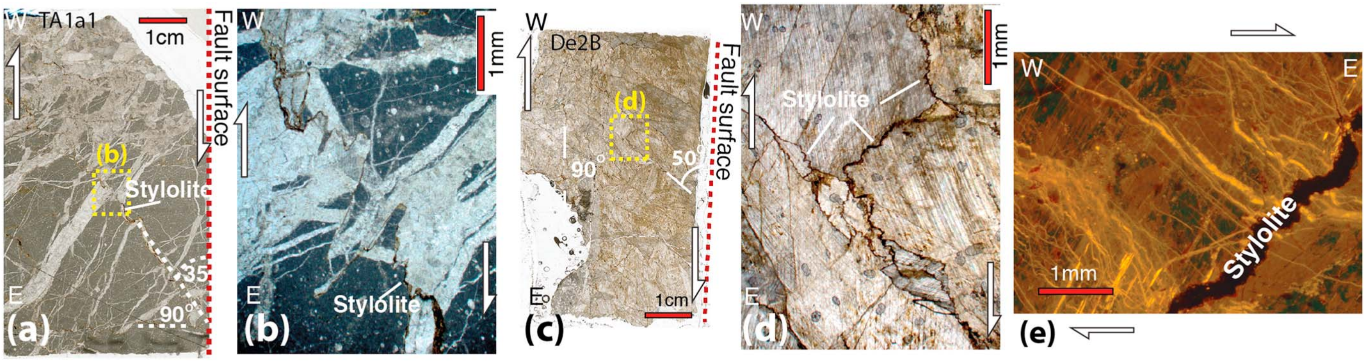

Figure 3. Microstructures of the deformed zones. Taşkesti-1 outcrop: (a) Horizontal thin section in limestone (arrows are parallel to the strike-slip fault) with networks of vertical tectonic stylolites and veins. Stylolite surfaces are seen here crosscutting at 35° and 90° with respect to the fault plane although these surfaces may be inclined at any angle to the fault plane. The stylolite peaks indicate an orientation of the main horizontal compressive stress that varies from near parallel to near perpendicular to the fault. (b) Magnified view of the yellow rectangle in Figure 3a where a stylolite crosscuts a preexisting vein, underlying the shortening direction due to pressure solution. Demirciler outcrop: (c) Horizontal thin section showing vertical tectonic stylolites crosscutting in all directions with respect to the strike slip fault. (d) Magnified view of the yellow rectangle in Figure 3c showing calcite twinning in the microlithons. (e) In horizontal thin section, cathodoluminescence image of a vertical stylolite with perpendicular vertical tension gashes calcite veins probably indicating a closed system where the calcite dissolved in stylolites and sealed the nearby fractures.

observed in the limestone: cataclastic zones and tectonic stylolites. The cataclastic zones are composed mainly of angular fragments of limestone and calcite veins (Figure 2f). Within the vertical fault zones, vertical tectonic stylolites surfaces appear at any angle between 0 and 90° with respect to the fault plane (Figure 3a). The stylolite peaks indicate a horizontal main compressive stress ranging from near parallel to near perpendicular to the fault. The damage zones show near-vertical veins at any angle between 0 and 90° with respect to the fault plane. In places, those veins are crosscut and dissolved by stylolites that indicate the shortening axis (Figure 3b). Another outcrop nearby (Ta2, Figures 1 and 2a), located in massive Cretaceous limestone, shows the same type of structures.

3.1.2. Demirciler Outcrop

This outcrop (De, Figure 1) is an active quarry that exposes an ~100 m wide shear zone hosted in Jurassic limestone (JKk1, Figure 2b). The damage zone contains a dozen main slip surfaces with associated cataclastic zones, similar to the Taşkesti outcrops. Here the fault also contains networks of near-vertical tectonic stylolites oriented in the same directions versus the near-vertical faults as in Taskesti. They are also associated with vertical tension gashes veins (Figure 3e). Microlithons show calcite twinning (Figures 3c and 3d).

3.1.3. Common Characteristics

In summary, three main observations can be made regarding the Taskesti and Dermirciler outcrop sites (Ta and De, Figures 2 and 3) that are common to other ones (Ciciler, Mekece, and Bolu) along locked fault segments **(**Ci, Me, and Bo, Figure 1).

1. Displacement along the fault is associated with two different types of structures: (i) mirror-like fault surfaces with relatively high Fe oxides concentration together with very narrow cataclastic gouges and nearby vein fracture arrays with damage followed by healing and (ii) shear zones of centimeter to decimeter thickness and oriented parallel to the mirror faults contain numerous tectonic stylolites that are indicative of pressure solution creep processes [*Janssen et al*., 1997].
2. Comparative chemical analyses of the damage zones and the shear zones versus the initial rocks show almost no change in the overall chemical composition. Local chemical differentiation may be seen in the stylolites that passively concentrate the insoluble species and in veins that are filled with pure calcite. Because vertical stylolites surfaces and tension gashes veins are clearly associated with right-lateral movement, this postseismic aseismic deformation must occur with a mean mass transfer distance from dissolution to reprecipitation zones of about 1 to 10 cm.
3. In several places, near-vertical vein arrays and tectonic stylolite surfaces occur at various angles with respect to the near-vertical fault surfaces: stylolite peaks (parallel to the local maximum compressive stress) and veins (perpendicular to the local minimum compressive stress) range from parallel to perpendicular to the strike-slip faults, indicating a rotation of the stress components with time (Figures 2 and 3).

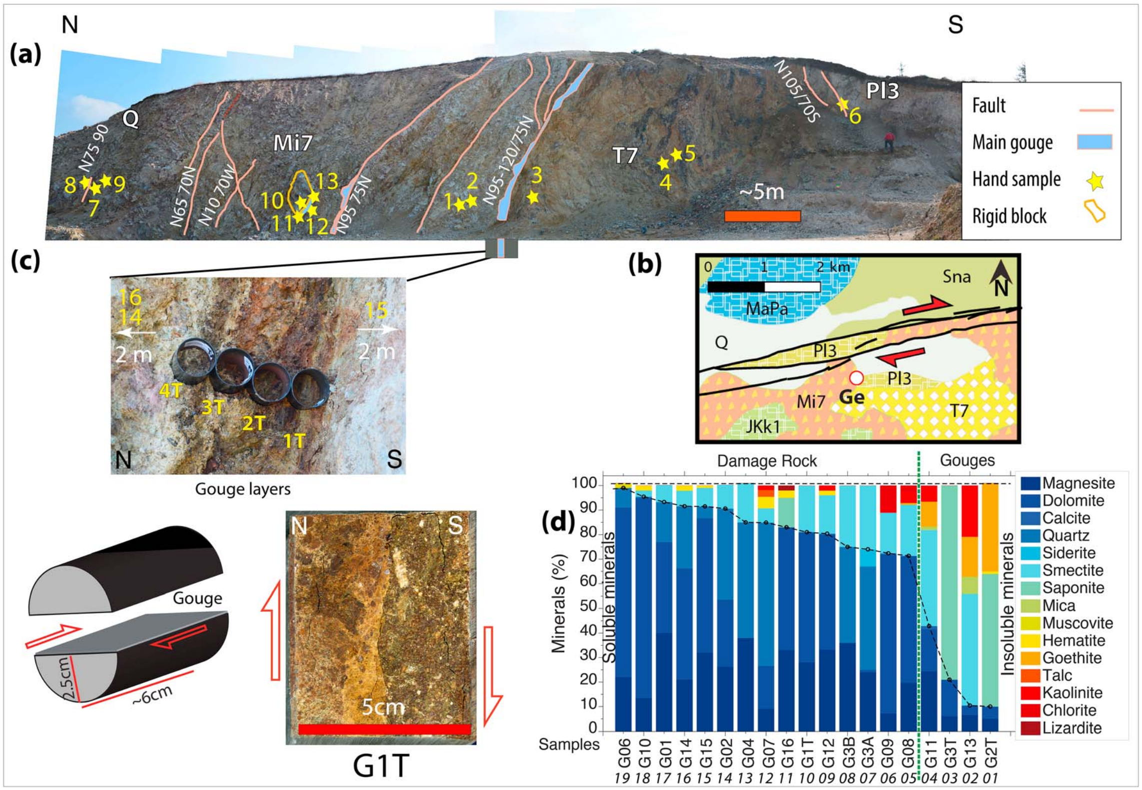

Figure 4. Gerede outcrop: general observation; see lithology in Figure 7e. (a) Photograph of the fault zone with the main structures and location of the sampling sites (yellow stars with G numbers). (b) Geological map. (c) Fault with gouge layers (with various white, red, or green colors). Each layer having different mineral contents was sampled using metal tubes labeled 1T to 4T. The sketch shows how the gouge was sampled, consolidated, and then cut to prepare thin sections with an example of horizontal slice of gouge sample after consolidation. Red arrows indicate the direction of horizontal slip on the main surface. (d) XRD analyses of mineral contents. The sample numbers are those shown on the outcrops of Figure 4c; see supporting information for detailed content. The samples have been sorted according to their content in soluble and insoluble minerals. The green dashed line separates damaged rock samples from those of the gouge that contain much more insoluble minerals than the damage zones. The G1T sample of gouge is rich in parallel-to-the-gouge altered carbonate veins. Sample G10 is a piece of a rigid block that is mainly composed of carbonate veins in contact with a clay gouge (samples G11–G13).

3.2. Characteristics of the Ismetpasa Creeping Segment

Unlike the locked segments, the Ismetpasa creeping segment exhibits several rock lithologies, with wide variations in mineral composition, microstructure, and fault structure but without any outcrops of limestone. At regional scale, there is a major geological transition between the locked segment (from Sapanca to Gerede) and the creeping segment (from Gerede to Mülayim). The creeping segment crosses the northern part of the huge Miocene to Paleocene Volcanic Galatia massif that extends about 200 km east-west and 200 km north-south, Figure 1b [*Akbaş et al.*, 2016]. In more details, the creeping fault segment lies for 90% of its length within the volcanic units and cuts narrow stripes of limestone and clastic rocks on less than 10% of its length. The total fault offset, of about 80 km, puts face to face the volcanic units either with other volcanic units or with sandstones, serpentines, or a near-continuous stripe of limestone (from Ismetpasa to Sarialan, Figure 1b). Near its eastern ending (Mülayim) the creeping segment crosses an ophiolite mélange that is included within a Trias-Jurassic schist unit.

All the outcrops along the Ismetpasa creeping segment have a common features: near E-W trending vertical faults and shear zones, with evidence of horizontal sliding (striaes) that are associated with thick gouge materials containing clay minerals and showing tectonic layering. The gouge generally has a mineral composition and inner microstructure different from that of the initial rock and the damage zone. In order to best describe these fault rock structures continuously from regional to microstructural scales, we describe in the following the fault zones (damage zone versus gouge) at three different sizes: macro (10–1000 m), meso (1–100 cm), micro (10–1000 μm).

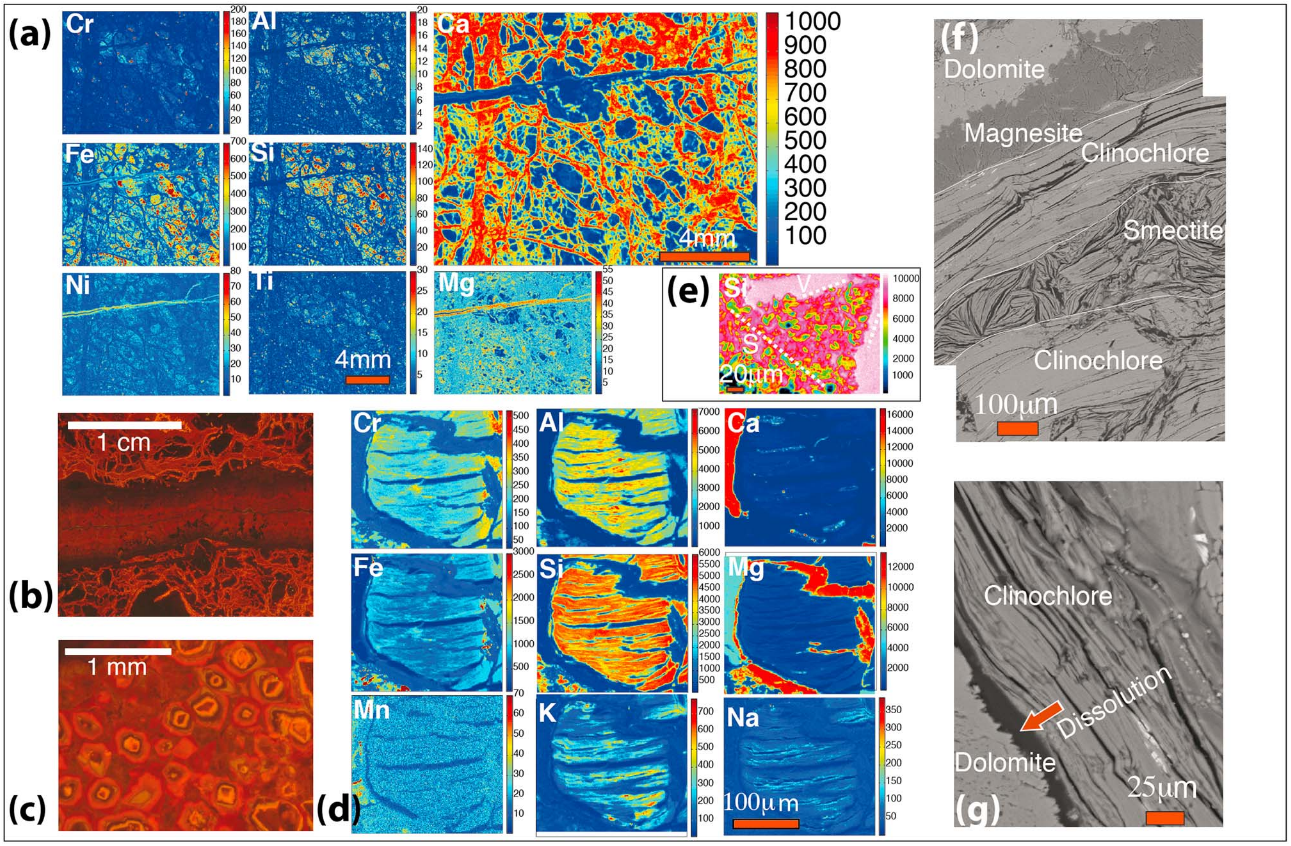

Figure 5. Gerede outcrop: microstructure of the damaged rock (sample G14 in Figure 4c), with initial volcanic rocks intensively sheared and fractured. (a) Chemical map of elements using XRF with typical network of calcite dolomite and magnesite veins parallel and perpendicular to the foliation. (b and c) Cathodoluminescence image of a carbonate veins: (b) magnesite vein crosscutting dolomite veins, indicating several cracking-sealing episodes and (c) calcite crystals with euhedral shape indicating growth in open cavities with fluid flow from depth through seismic faults. (d) Zoom using EPMA chemical mapping showing a cavity filled with chlorite and clay minerals. (e) Quartz veins (V) more or less perpendicular to cleavage (S) in the damage zone (G07 in Figure 4a). (f) SEM image of a vein (G09 in Figure 4a) composed of dolomite and magnesite (top) bounded by layers of clinochlore and smectite (bottom). (g) Stylolite peaks along dolomite vein indicative of stress-driven dissolution, with an orientation in agreement with the main compressive direction along the North Anatolian Fault.

3.2.1. Gerede Outcrop

A fault outcrop near Gerede (Figure 4) is located at the western end of the Ismetpasa creeping segment (Ge, Figure 1b) where the present-day creep rate tends to zero [*Cetin et al*., 2014]. The fault crosses volcanic units of the Galatia massif, (Mi7 and T7, Figures 4a and 4b) [*Adiyaman et al*., 2001]. The different units are indistinguishable and contain a mélange of dacite, andesite, and trachy basalts [*Wilson et al*., 1997]. The outcrop is located in an abandoned quarry on the roadside west of Gerede south of the main faults (Figures 4a and 4b). The initial volcanic rock is highly damaged with fractured blocks and near-vertical veins in all directions. In places, 5 to 50 cm thick clay-rich fault gouges contain very weak material (noncohesive) that can be dug up by hand (Figure 4c).

3.2.1.1. Damaged Rock and Gouge Macrostructure

Thanks to the good exposure of the outcrop, the architecture of the fault zones could be mapped, as well as the spatial distribution of the mineral composition in the fault gouges compared to the damaged rock (sample locations marked by yellow stars in Figure 4a). The main fault contains gouge layers, which have been sampled using metal tubes (Figure 4c). Figure 4d displays the mineralogical composition from XRD analyses of all samples sorted by soluble (and insoluble) mineral contents and their distance to the fault core. A clear spatial variation in the mineralogical composition can be seen, with an abrupt change when passing from the damage zones to the gouges (indicated by the green dashed line in Figure 4d). Most of the damaged rocks contain a large amount (70% to 95%) of carbonate minerals, such as magnesite and dolomite, in veins. The gouge samples contain 60% to 90% of smectite (montmorillonite and saponite) and other insoluble minerals (phyllosilicates and iron oxides).

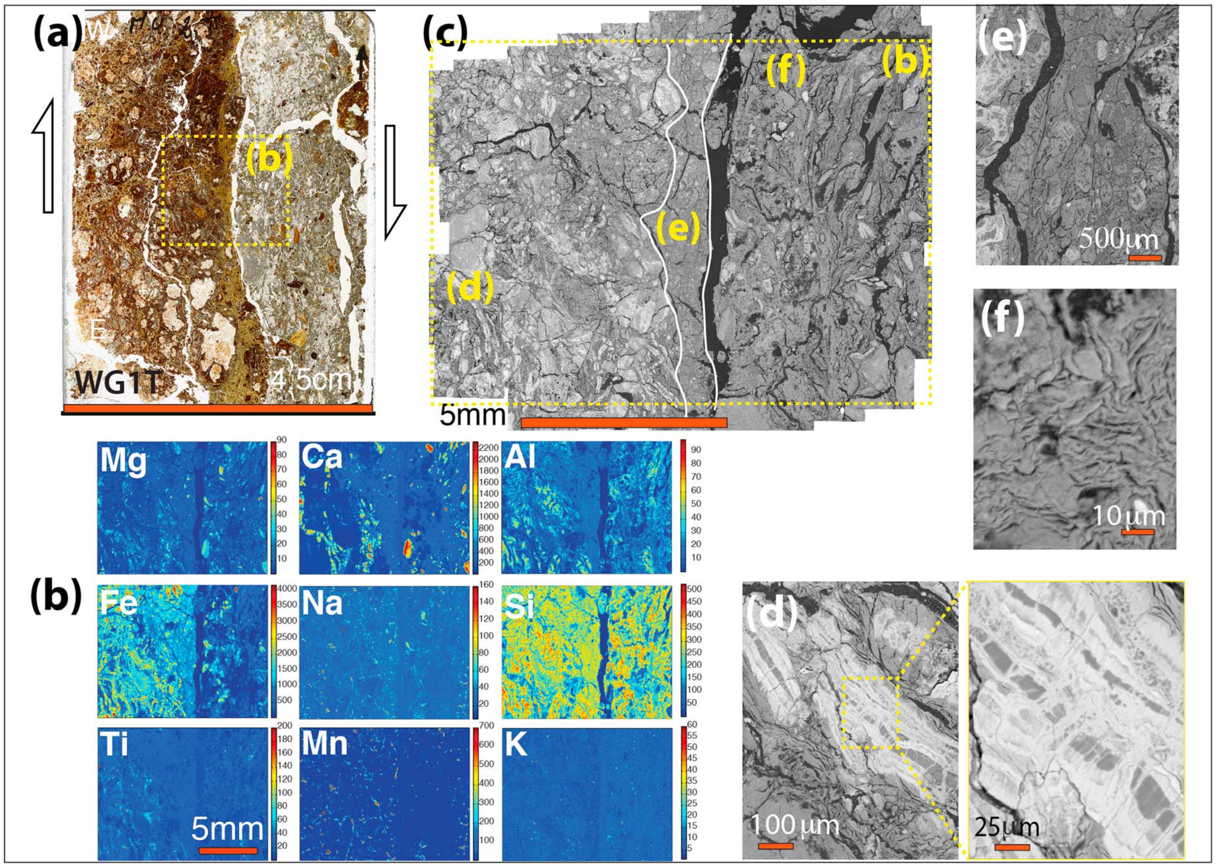

Figure 6. Gerede outcrop: microstructure of the gouge. (a) Horizontal thin section of part of gouge sample G1T (see Figure 4c for sample location) showing a contact between two layers: a brownish-red layer and a gray layer. Arrows are parallel to the strike-slip fault. (b) Map of elements at the contact between the two layers using XRF, showing that the main difference of color between the two gouge layers is due to variations in iron content. (c) Mosaic of SEM-BSE images at the same location with the diffuse boundary (contact layer) attached to the brownish-red layer. (d) BSE image showing Fe-rich carbonate veins parallel to the layering that form a boudinage with Fe-rich carbonate sealing (see details in the enlarged part). (e) BSE image of the boundary zone and (f) typical smectite minerals in the gray layer.

3.2.1.2. Damaged Rock Mesostructure

Centimeter-scale maps of elements measured using XRF show that the typical damaged rock is highly carbonated, as indicated by zones rich in Ca and Mg (Figure 5a). These are veins of dolomite (Ca + Mg) in all directions, crosscut by magnesite veins (Mg) in one direction oblique to the fault. Consequently, there is almost no significant trace of the initial rock containing elements like Si, Al, and Fe. A cathodoluminescence image was focused on a magnesite vein crossing dolomite veins, both vein arrays showing several crack-seal episodes (Figure 5b), as well as cavities filled with euhedral calcite (Figure 5c).

3.2.1.3. Damaged Rock Microstructure

Zooming on damage zones using element EPMA maps shows that between the network of dolomite and magnesite veins, some foliated chlorite minerals remain (Figure 5d). Preserved quartz veins can also be seen (V) more or less perpendicular to the solution cleavage (S) (G07) (Figure 5e). SEM images in Figure 5f show dolomites and magnesite veins locally parallel to alternating layers rich in clinochlore and smectite (G09). The clinochlore layers have a foliated structure, whereas the smectite layers show no clear preferred orientation (Figure 5f). In places, the carbonate veins show rough walls, indicating partial dissolution (Figure 5g).

3.2.1.4. Gouge Mesostructure

Thin sections were prepared from samples taken from the gouge layers in order to study their chemistry and structure. As pointed out previously, here the gouges are formed by layers oriented subparallel to the fault surface (Figure 4c). The thin section made from part of the G1T sample with high smectite content is presented in Figure 6a. This sample is composed of two types of gouge layers that are associated with different structures and minerals: a brownish-red layer, a diffuse boundary (contact zone), which seems attached to the brownish-red layer, and a gray layer. The chemical difference is revealed on the XRF element map (Figure 6b):

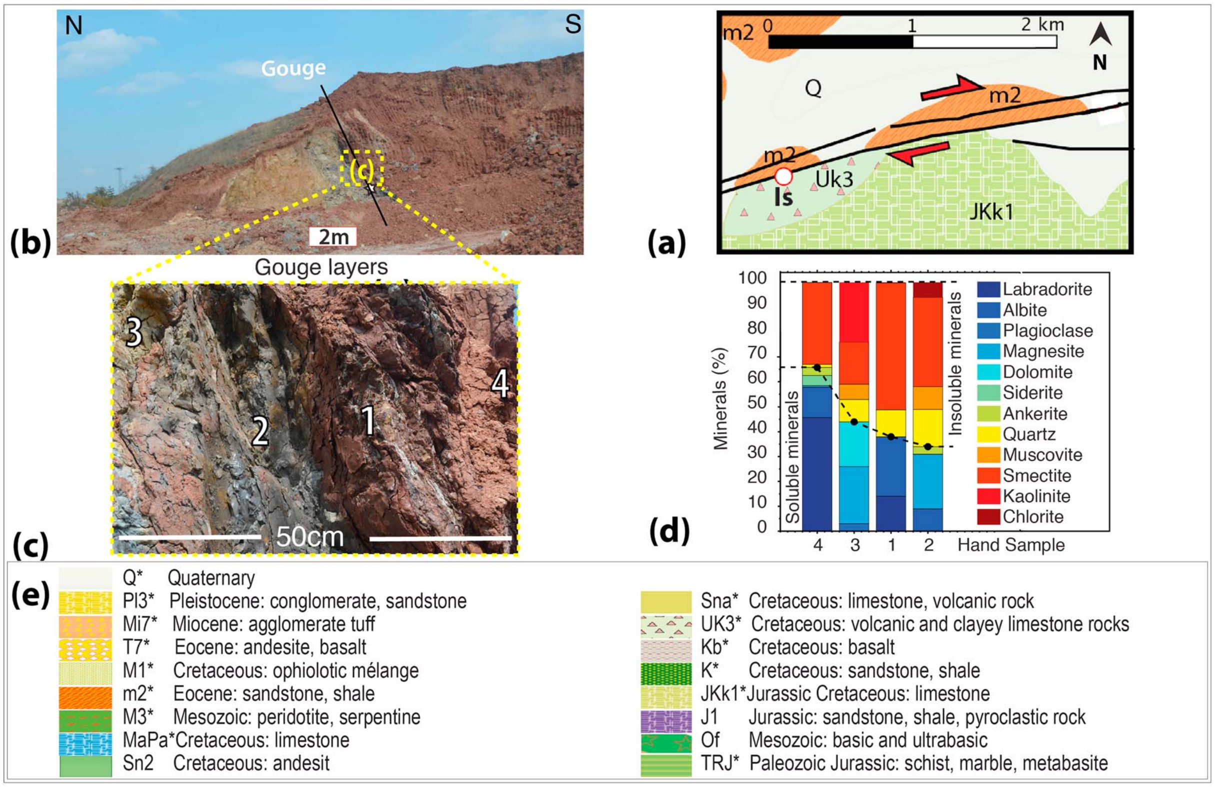

Figure 7. Ismetpasa outcrop: fault gouge with clasts of the initial rock. (a) Geological map (see lithology in Figure 7e). (b) Photograph of the outcrop with the volcanic host rocks and the fault zone containing clay gouge layers. (c) Zoom on the gouge layers (samples 1–3 in Figure 7d) and the damaged rock (sample 4 in Figure 7d). (d) XRD analyses of gouge mineralogy compared to the damage zone; see the supporting information for detailed content. (e) Geological units of the 1/100,000 geological maps [*Herece and Akay*, 2003] of Figures 2, 4, 7, 9, and 12–14. The asterisks refer to units that have been sampled.

the matrix of brownish-red layers is richer in Fe in comparison with the gray layers and is crosscut by Mg-Ca carbonate veins, some also being rich in Fe. A mosaic of BSE images shows the structural characteristics of these zones (Figure 6c). In the brownish-red layer, dolomite clasts (Mg + Ca) appear as boudins that are aligned along curvy layers, while in the gray layer the dolomite clasts are smaller and show a more random arrangement in the smectite matrix.

3.2.1.5. Gouge Microstructure

The brownish-red layers contain carbonate fragments embedded in a clay matrix with a network of Fe-rich carbonate veins parallel and perpendicular to the foliation (Figure 6d). The contact zone is characterized by very small, rounded, granular carbonate fragments embedded in a smectite matrix (Figure 6e). The gray zone comprises fragments of carbonate veins that form small angular fragments spread randomly within the smectite matrix. The smectite matrix may have been disturbed during the thin section preparation process; however, the clay foliation is organized in domains without preferred orientation (Figure 6f).

3.2.2. Ismetpasa Outcrop

This outcrop is located 2.6 km west of the Ismetpasa settlement (Is, Figure 1b), where an active creep rate of 6–10 mm/yr has been measured [*Cetin et al.*, 2014] and where there is clear evidence of creep offset (40 cm) along the concrete wall of a gas station. Recently, a fresh outcrop was excavated (Figures 7a and 7b) for the construction of a water canal and this gives access to the entire fault zone, including the initial rock. An Eocene sandstone-shale unit (m2) on the north side of the fault is in contact with a volcanic rock (Uk3) on the south side. The fault zone in this volcanic rock contains several thin gouge layers, with anastomosing geometry and presence of cleavage. Trails of CO_2 bubbles in a small pond are indicative of active CO_2 circulation along the fault.

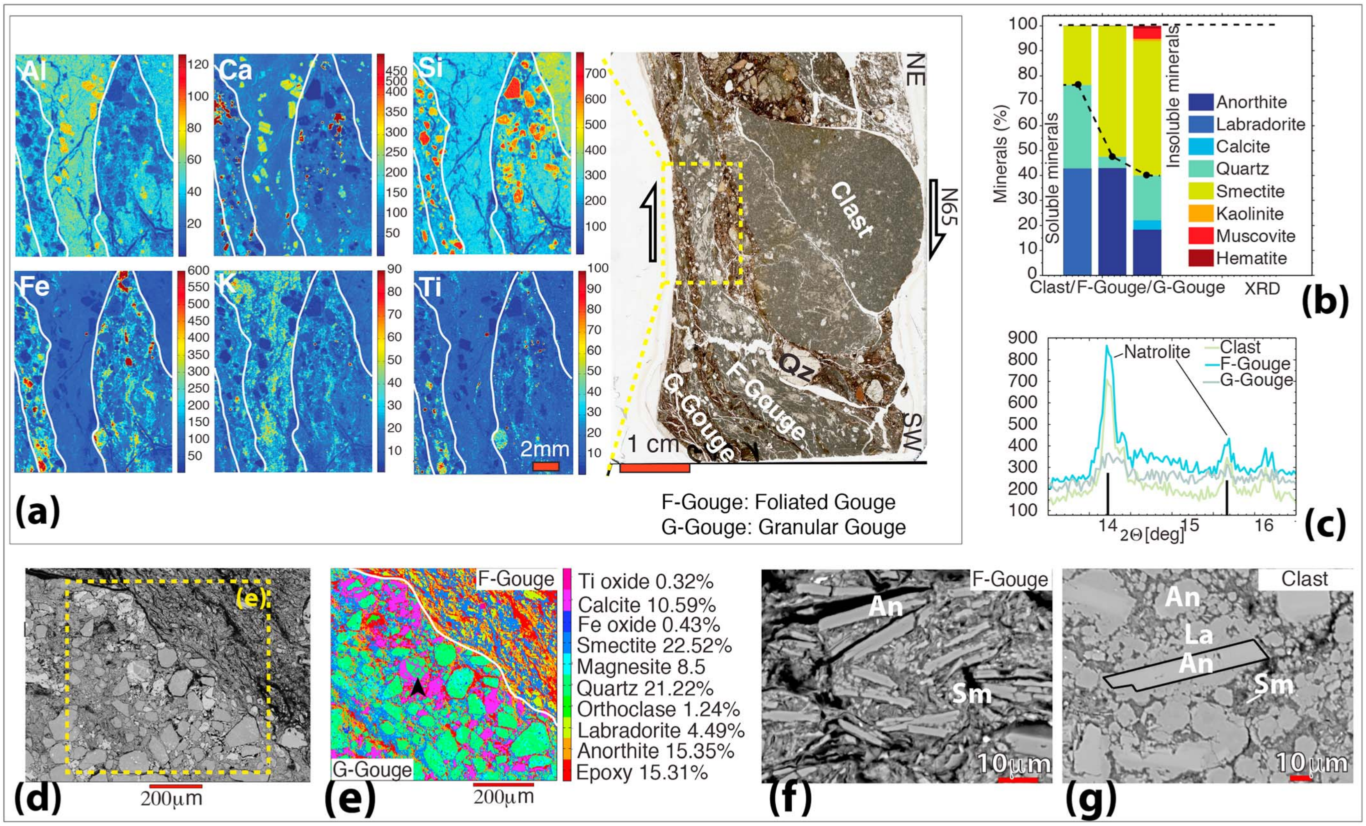

Figure 8. Ismetpasa outcrop: (a) Horizontal thin section (sample 1 in Figure 7c) oriented perpendicular to the strike-slip fault with foliated gouge layers (F-gouge), granular gouge (G-gouge) and a volcanic clast marker of the initial state (right), and XRF maps of the F- and G-gouges (left). (b) XRD quantification of mineral concentrations of those samples reveal that the smectite content is more than double in the gouges compared to the clast. (c) XRD pattern of the clast, F-gouge, and G-gouge with natrolite peak (>1%). (d) SEM image showing the boundary between the foliated gouge and the granular gouge. (e) Mineralogical map from EPMA analysis showing the difference between the granular (bottom) and the foliated (top) gouges; some grains contain crack-seal calcite veins in all directions (arrow) (f and g) alteration of plagioclases: in the foliated gouge, anorthite grains are surrounded by large amount of smectite (Figure 8f) and in the clast anorthite grains are surrounded by labradorite with few smectite around in the clast (Figure 8g).

3.2.2.1. Damaged Rock and Gouge Mesostructure

The site exposes a main fault plane with gouge zones (~25 cm thick) with continuous layering of centimeter to millimeter thickness (Figures 7a–7c). The XRD data of samples taken in and near the gouge (Figure 7d) indicate that the phyllosilicate content (smectite, kaolinite, muscovite, etc.) ranges from ~30% to 50% with variable quartz content. In this case, the soluble (mobile) minerals are plagioclase feldspars.

3.2.2.2. Damaged Rock and Gouge Microstructure

On a thin section oriented perpendicular to the fault plane (Figure 8a), shear zones are deflected around a clast, which is clearly an undeformed piece of volcanic rock and which can be considered as representative of the initial volcanic rock (see Figure 8g) assuming that it was rather homogeneous. The shear zone consists of an alternation of two types of gouges: a granular gouge and a foliated gouge. They can be distinguished by both structure and chemical composition. When comparing the initial rock composition with the composition of these two types of gouge (Figure 8b), the phyllosilicate content (smectite) varies from ~20% to 60%. There is less quartz in the foliated zone than in the granular zone and more feldspars. These samples also reveal a small amount (~1%) of zeolite group mineral (natrolite) (Figure 8g). From XRF and EPMA maps (Figures 8a–8e), the granular gouge is characterized by angular and rounded grains of plagioclases and quartz embedded locally in a carbonate matrix with some thin layers of smectite. Some of the grains show indentation between plagioclase, quartz, and calcite, and some grains contain crack-seal calcite veins in all directions (Figure 8d). The foliated zone comprises much smaller grains of quartz and feldspar embedded in a smectite matrix. SEM observations in this foliated clay gouge (Figure 8f) show the elongated tabular

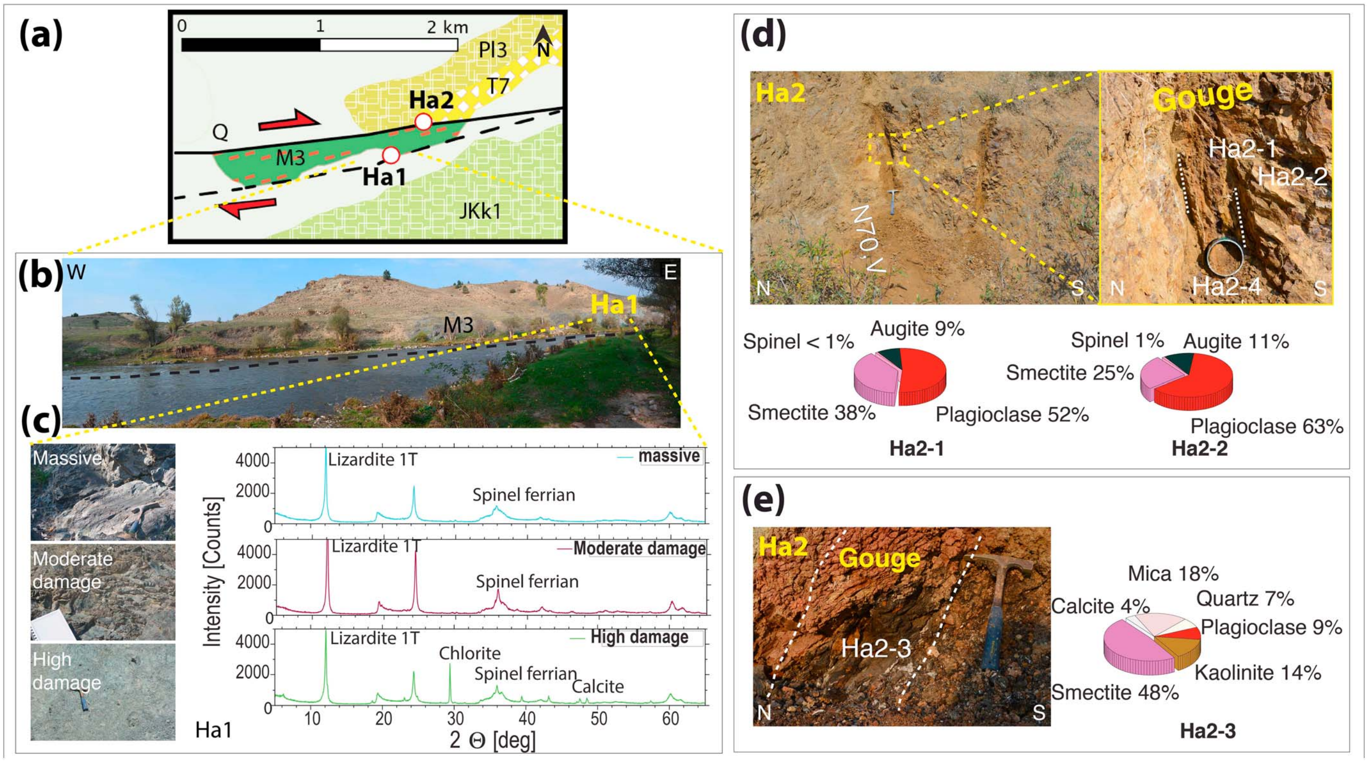

Figure 9. Hamamli outcrops: on minor fault in serpentines, (Ha1 in Figures 9a–9c) and in major fault gouge in volcanic rocks at the contact with serpentines (Ha2 in Figures 9d and 9e). (a) Geological map with sample locations (see lithology in Figure 7e). The main active fault is indicated by a thick black line and is currently monitored by leveling methods that show active creep. A secondary (nonactive) fault is highlighted by a dashed line. (b) Serpentine outcrop along the secondary fault (dashed black line). (c) Zoom on the three types of damaged materials in the serpentine unit and corresponding XRD spectra showing mineral compositions. (d) Gouge and volcanic host rock outcrop; see location in Figure 9a, with layering and mineral composition calculated from XRD data. (e) Gouge, same location as Figures 9d, with anastomosing cleavage and mineral composition calculated from XRD data.

crystals of calcic-plagioclase (with average dimensions ~2 × 10 μm) that are subparallel to the undulated cleavage surface. An interesting change in the plagioclases may be seen when comparing the plagioclases from the clast (anorthite core surrounded by labradorite, Figure 8g) with the plagioclases within the clay gouge (no more labradorite around the core and development of smectite, Figure 8f).

3.2.3. Hamamli Outcrops

These outcrops are located 0.4 km east of the Hamamli settlement (Ha, Figure 1b) where an active creep rate of 5 mm/yr is measured [*Cetin et al*., 2014]. This area is characterized by the presence of an elongated body of serpentinized peridotites of Mesozoic age (M3, Figure 9a) and has been studied by *Dor et al*. [2008] and *Ozakin et al*. [2012].

This serpentine body along the North Anatolian Fault is in contact with a volcanic unit to the north (T7) and a Jurassic limestone unit to the south (JKk1) lying under quaternary cover. On this site, the focus was placed on two outcrops along two faults: the first (Ha1) on a minor fault in the serpentine and the second (Ha2) on the major fault gouge in the volcanic rock at the contact with serpentine units (Figure 9a). This was a good opportunity to compare the behavior of serpentine with volcanic gouge.

The first outcrop, Ha1, along the minor fault (Figure 9b) exposes serpentine rocks with anastomosing polished surfaces and evidences of shear deformation. At the outcrop scale the variations in damage intensity are spatially heterogeneous: the serpentine shows three kinds of damage, from slight and pervasive to moderate and intense (Figure 9c). The main compositional difference is that the highest deformed serpentines contain more chlorite and calcite than the least deformed ones (Figure 9c).

The second outcrop, Ha2, along the major fault, shows a gouge in volcanic rocks (T7) near the contact with the serpentine body M3 (Figure 9a).

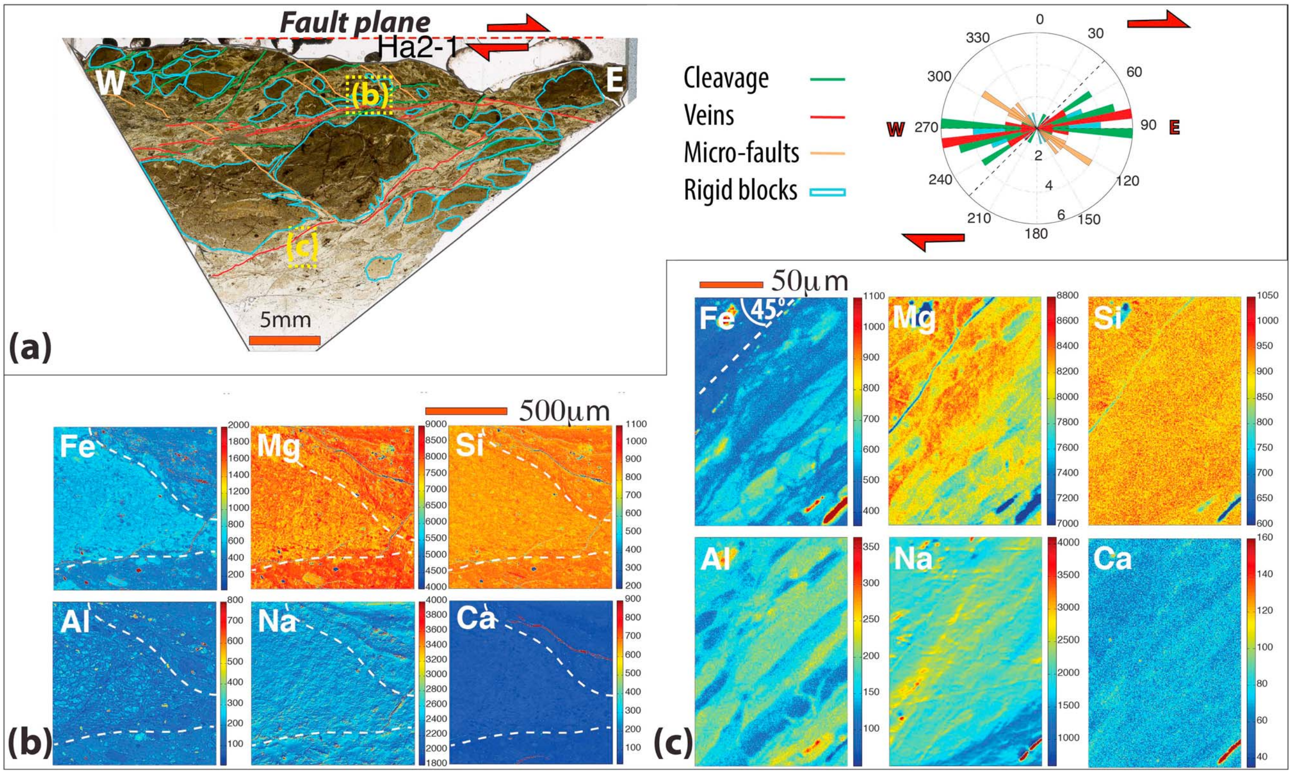

Figure 10. Hamamli outrops: damage zone near the fault gouge (Ha2). (a) Horizontal thin section of damage zone near the gouge (Ha2-1), perpendicular to the strike-slip fault shown in Figure 9d, with segmentation of veins, cleavage, microfault, and rigid blocks whose relative orientations are indicated in the rose diagram. (b) XRF map, located on the thin section, showing rigid block with a mesh texture and parallel-to-layering siderite vein. (c) EPMA chemical maps, located on the thin section, showing tectonic layering oblique to the fault.

3.2.3.1. Gouge Mesostructure

The XRD measurements (Figures 9d and 9e) show the variation in composition from damaged rock to gouge, with smectite content increasing from 25% in the damaged rock (Ha2-2) to 38% in a transition zone (Ha2-1) and up to 48% in the gouge (Ha2-3), with feldspar content decreasing accordingly.

3.2.3.2. Damaged Rock Microstructures

A thin section (Ha2-1) located at the transition between damaged rocks and gouge (Figure 9d) shows a cleavage angle ranging from 0 to 45° with respect to the fault direction with sets of microfaults at about 30° from the fault, as in C-S shear structure (Figure 10a). Shear deformation can be distinguished by alignments of iron oxides that reflect tectonic layering corresponding to the cleavage with rigid blocks surrounded by more deformed zones. The contrast in mineral composition of these zones can be seen on XRF map (Figure 10b), with veins of siderite parallel to the cleavage. EPMA maps of elements across the shear zone (Figure 10c) also show the compositional tectonic layering oblique to the fault at smaller scale.

3.2.3.3. Gouge Microstructures

A thin section of gouge (Ha2-4, Figure 9d) reveals two rich-in-clay shear zones, 100–200 μm wide, with a high degree of deformation oriented obliquely to the fault (Figure 11a), where the grain size is smaller than 30 μm. Given the very small grain size, it is difficult to quantify the change in element distribution along the deformation zones from XRF maps. However, the high deformation zones are depleted in Ca and enriched in Fe and K. The network of fractures both parallel and perpendicular to the high deformation zones contains carbonate minerals rich in Mn (Figure 11b). Of the two high deformation zones, one contains localized cataclastic damage with distinct boundaries (Figure 11d), while the other is more diffuse. Two types of elongated calcite bodies can be observed in places that are subparallel to this second high deformation zone. The first type corresponds to compact veins that show dissolved edges adjacent to microstylolites (Figure 11e); the second type takes the form of clusters of grains and is associated with iron oxides (Figures 11f and 11g).

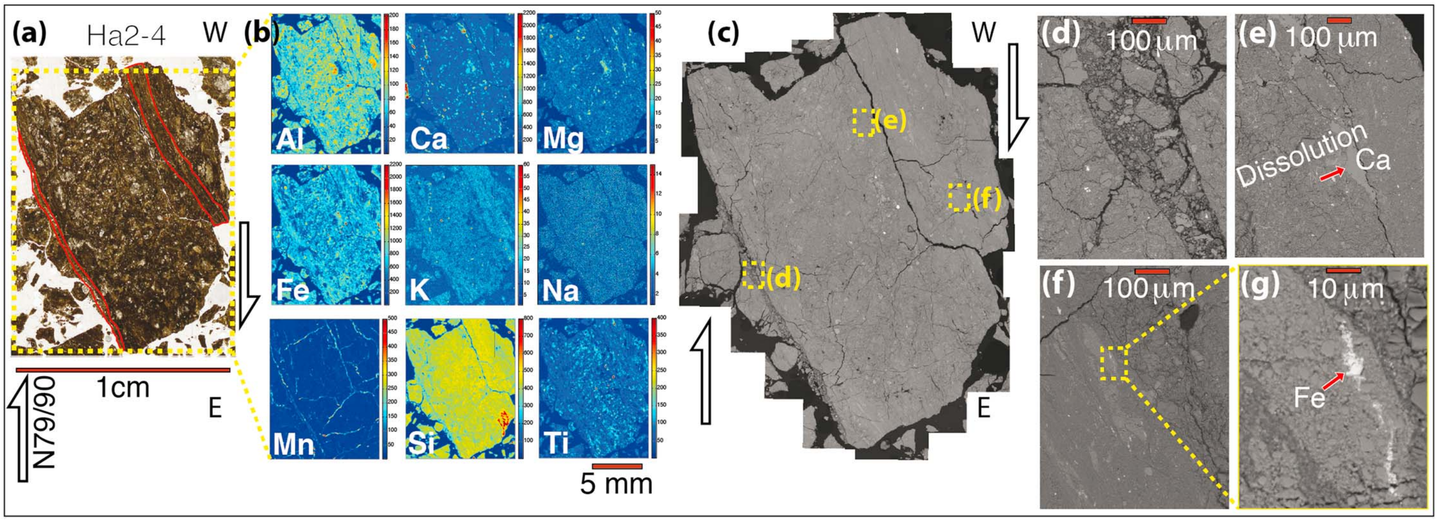

Figure 11. Hamamli outcrops: along the main fault gouge (Ha2). (a) Horizontal thin section of a gouge core Ha2-4 (see location Figure 9d; arrows are parallel to the strike-slip fault), with two shear zones (in red) oblique to the fault. (b) XRF map of elements showing the layering. (c) SEM-BSE panorama with three selected zones: (d) cataclastic band, (e) tectonic microstylolite oblique to the fault, dissolving calcite vein, and (f) calcite aggregates forming elongated clasts along horizons subparallel to the cataclastic bands. (g) Located in Figure 9f; in places some of the calcite clasts are associated with iron oxides.

3.2.4. Yazioren Outcrop

Near Yazioren the present-day creep rate is 6 mm/yr in average [*Cetin et al.*, 2014]. In this zone, the fault is more diffuse and forms a large shear zone [*Ellero et al.*, 2015]. The outcrop (Ya, Figure 1b) is located on the roadside about 1 km southwest of Yazioren village in volcanic and clayey limestone rocks (Uk3, Figure 12a). It shows an ~20 m shear zone with metric to decimetric width localized anastomosing cleavage (Figure 12b). Unfortunately, in view of the limited exposure, it was not possible to compare the composition of the shear zone with that of the initial rock. Unlike the other outcrops, it is not easy to distinguish between damaged rock and gouge. However, zones with anastomosing cleavage were investigated. The mean mineralogical composition of the rock indicates a mélange of carbonate and volcanic minerals, with 36% of mica.

3.2.4.1. Gouge Mesostructure

In the thin section Ya2 (Figure 12c) there is a clear structural and mineralogical separation between two types of layers. The first type of layer is made of carbonate-rich material mainly composed of calcite, dolomite, gypsum, and quartz grains (so-called calcitic-silicate layer). The layer elements are disrupted and form a boudinage with pinch-and-swell structure where the open voids developed between the boudins are sealed by calcite. The second type of layer is rich in muscovite, chlorite, albite, and anatase (so-called aluminosilicate layer). XRF maps of elements (Figure 11d) show the oblique-to-the-fault foliation (40–60°) that has been locally rotated near a small shear zone parallel to the fault. They also highlight the contrasting composition of calcitic-silicate layers and foliated aluminosilicate layers with calcite sealing of the interboudin veins.

3.2.4.2. Gouge Microstructure

The mosaic of SEM images shows the microstructures of the two types of layers. Figures 12e and 12f focus on a zone with an aluminosilicate layer that is confined between two calcitic-silicate layers. Here the upper calcitic-silicate layer is more disrupted and fractured compared to the aluminosilicate layer. Calcitic-silicate layers deform by extension due to boudinage with carbonate sealing and contraction due to stylolitization of the boundary (Figure 12f). They are composed of large closely entangled grains of quartz in a calcite vein network with dissolution at grain boundaries (Figure 12g). In contrast, the aluminosilicate foliated layer (Figure 12h) contains smaller grains of different minerals (quartz, calcite, plagioclase, mica, chlorite, Ti and Fe oxides, etc.) that have been deformed by the dissolution of the smaller grains of quartz and feldspars. This is attested by the passive concentration of the more insoluble phyllosilicates and oxide minerals in the solution cleavage planes. Another thin section Ya3 (Figure 12i) shows an example of a layer that has been completely disrupted, as a result of rotations that have formed rolling clasts between a boudinage of layers. The contrast of deformation behaviors between polymineralic and monomineralic materials is clearly apparent here and on other thin sections. Polymineralic layers corresponding to foliated layers show dissolution of

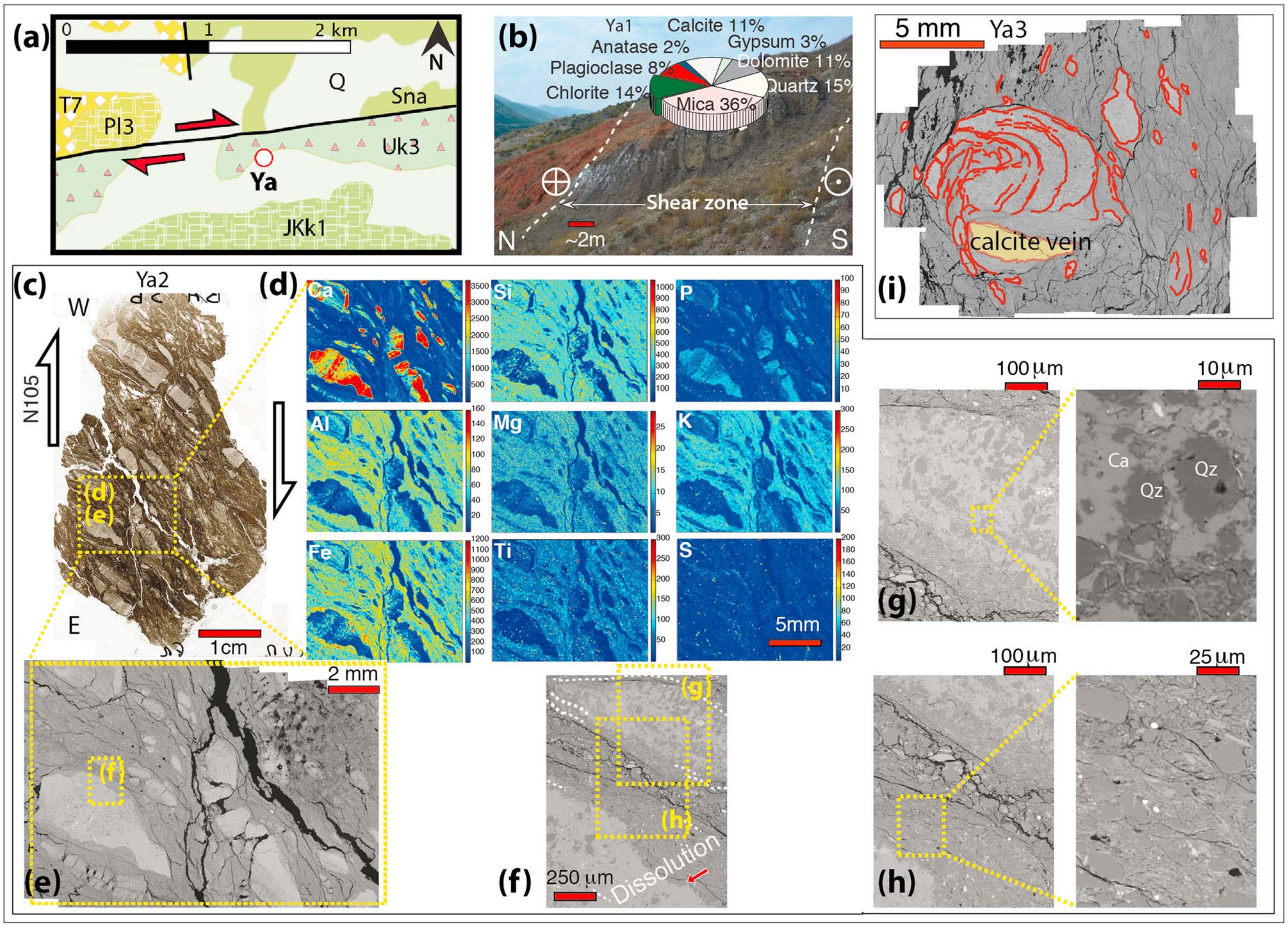

Figure 12. Yazioren outcrop: shear zone. (a) Geological map with outcrop location; see lithology in Figure 7e. (b) Shear zone, ~20 m wide, with composition in a deformed zone shown in the pie diagram. (c) Horizontal thin section (Ya2) showing a boudinage of carbonate layers with stylolitic boundaries. Arrows are parallel to the strike-slip fault. (d) XRF maps of elements showing the foliation layering. (e) Mosaic of SEM images. (f) Zoom in between the layers with microstylolites at the boundary of the clast. (g) Detail of calcitic-silicate layers and zoom on grain indentations between quartz and calcite. (h) Detail of aluminosilicate foliated layer and zoom showing that some stronger minerals (plagioclase and quartz) are embedded in the clay. (i) Horizontal thin section (Ya3): tightly folded layers overprinted by a rigid calcite vein.

quartz and feldspar at grain scale (Figures 8b–8e) and are folded (Figure 12i), whereas the massive monomineralic calcitic veins, which cut the boudins or the rolling layers of clasts, are, in general, undeformed (Figures 12d and 12i). The only deformation that is seen for such monomineralic veins and for the others dispersed in the matrix is the dissolution at their boundaries (Figures 12f, 12g, and 12i).

3.2.5. Sarialan Outcrop

This outcrop (Sa, Figure 1b) is located in an area where an average creep rate of 8 mm/yr is measured [*Cetin et al.*, 2014] in volcanic rock (Uk3), in contact with a sandstone-shale unit (K) north of the fault Figure 13a. The fault contains a foliated gouge composed mainly of aluminosilicates, with 41% of mica and 24% of kaolinite (Figure 13b).

3.2.5.1. Gouge Mesostructure

The thin section Sa1 (Figure 13c) shows two types of layers: one with a dense array of quartz grains and the other one with isolated small quartz grains embedded in a foliated aluminosilicate matrix. XRF maps of elements focused on the contact zone between these two layers (Figure 13d) show that the quartz-rich layers are fractured, with some veins sealed by calcite. The foliated zone shows thin layering underlined by the variations in Al and K contents.

3.2.5.2. Gouge Microstructure

A SEM-BSE panorama shows the differentiation between quartz-rich and aluminosilicate-rich layers (Figure 13e). Zooming on the aluminosilicate-rich layers, which contain illite, kaolinite, small amounts of

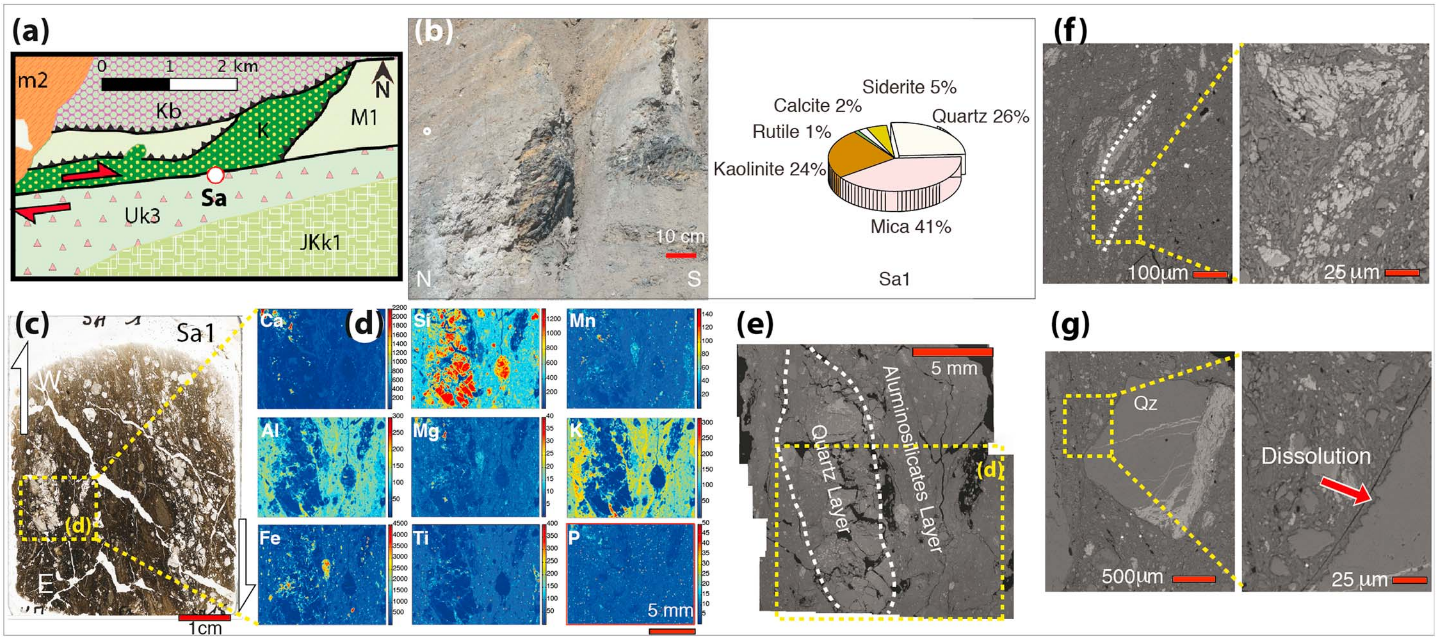

Figure 13. Sarialan outcrop: fault gouge. (a) Geological map (see lithology in Figure 7e). (b) Outcrop with mineral content. (c) Horizontal thin section Sa1 in the vertical E-W gouge: arrows are parallel to the strike-slip movement. (d) XRF maps of elements showing the foliation layering: arrows are parallel to the strike-slip fault. (e) SEM_BSE panorama. (f) Detail of folded layers: the zoom shows the rotation of elongated plagioclase minerals. (g) Quartz grain with dissolved edges and carbonate veins.

quartz, and some rare albite, shows that these layers are folded, with the long axis of the mineral grains parallel to the folded layers (Figure 13f). In the quartz-rich layer the quartz fragments have rough dissolution boundaries (microstylolites), and the fractures are filled with iron-rich carbonate minerals (Figure 13g).

3.2.6. Mülayim Outcrop

This outcrop (Mu, Figure 1b) is located in an area where the measured creep rate is close to 6 mm/yr [*Cetin et al*., 2014]. It is located on a riverbank where the fault crosscuts a block of ophiolitic mélange (M1) within schists, marbles, and metabasite units (TRJ). Here as in other examples, tectonic layering can be observed both in the gouge and in the nearby damaged rock (Figure 14b).

3.2.6.1. Gouge Mesostructure

XRD analysis shows the composition of the gouge from its core to its boundary (Figure 14c). The thin section Mu1 shows layers subparallel to the fault (Figure 14d). The XRF maps indicate layering at various scales cross-cut by carbonate veins in all directions (Figure 14e). Three types of carbonate veins appear on the Ca map: (i) veins oblique or perpendicular to the layers, (ii) tightly folded veins with millimeter wavelength, and (iii) veins parallel to the layers.

3.2.6.2. Gouge Microstructure

SEM-BSE images (Figure 14f) also show tightly folded thin carbonate veins and the growth of mineral sealing in veins parallel and oblique to the foliation (Figures 14i and 14j). Alternations of weak and strong layers are seen with a mix of clay and phyllosilicate with small grains of plagioclases, mica, chlorite, and quartz in the weak zones (Figure 14g) and large grains of plagioclase and quartz sealed with dolomite in places mixed with carbonate veins with dispersed phyllosilicates in the strong zones (Figure 14h).

3.2.7. Common Characteristics

In summary, five main observations can be made regarding these outcrops along the Ismetpasa right-lateral creeping segments (Figures 4–14).

1. The displacement along the fault is associated with the progressive development of wide shear zones (of hectometric width) that comprise gouge zones (of centimeter to meter width) embedded into wide damage zones (hectometric in width). The gouges are characterized by the development of

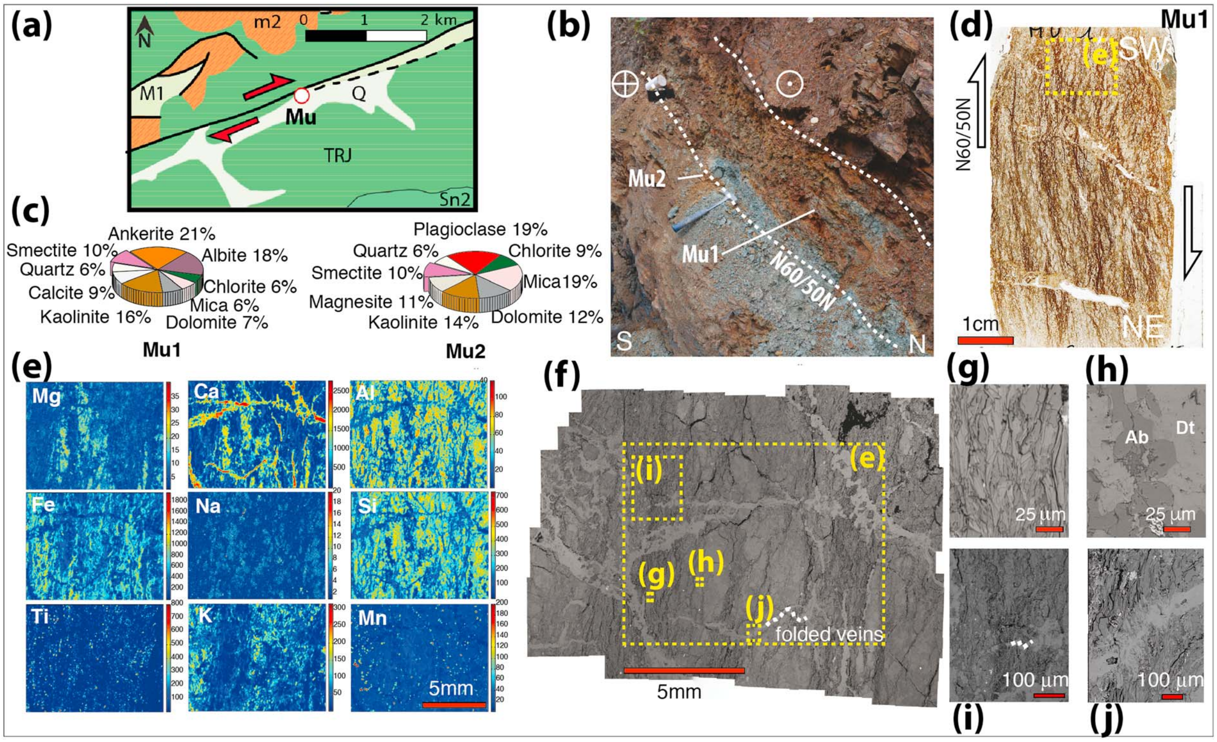

Figure 14. Mülayim outcrop: fault gouge. (a) Geological map (see lithology in Figure 7e). (b) Outcrop with gouge and sample locations. (c) Mineral content. (d) Horizontal thin section Mu1 with tectonic layering and carbonate veins, arrows parallel to the strike-slip fault. (e) XRF maps showing mineral differentiation between the layers crosscut by calcite veins. (f) SEM-BSE panorama showing the layered structure associated with thin folded veins. (g) Weak layer with small grains of plagioclase, quartz in a phyllosilicate matrix. (h) Strong layer composed of albite (Ab) and dolomite (Dt). (i) Detail of thin folded calcite veins. (j) Detail of the growth of the mineral sealing in veins parallel and oblique to the foliation.

pressure solution cleavage and foliation, whereas the damage zones show numerous fractures sealed by carbonates.

2. Comparative chemical analysis of the damage zones and the gouges versus the initial rocks show a drastic evolution with time. The gouges are depleted of the soluble minerals such as quartz and feldspars and passively enriched in the less soluble minerals such as phyllosilicates and Fe and Ti oxides. By contrast, the damage zones are enriched in carbonate up to such content (90%) that it is often difficult to recognize the initial rocks.
3. Various markers of ductile deformation associated with cleavage development such as rolling clasts, asymmetrical folds, and cleavage planes at various angles to the main slipping zone that evolve to fine-grained layers attest of an early ductile behavior of the damage zones before their strengthening by fracture sealing and the concomitant development of localized soft gouges.
4. Cataclastic gouges and intense networks of carbonates veins with euhedral mineral growth that reflect fast void openings attest of seismic events that must have affected the damage zones at an early stage of the fault initiation and opened paths for large carbonated fluid flows coming from outside the fault.
5. Finally, at grain scale, two specific processes can be observed: (i) the metamorphic transformations of phyllosilicates and some feldspars that evolve into clay minerals and (ii) the contrasted behavior of monomineralic rocks that are very difficult to dissolve except at their boundaries by comparison with polymineralic rocks that are much more easily transformed by stress-driven mass transfer processes.

4. Discussion

All observations and measurements presented above allow discussing the characteristics of gouge formation, evolution, and mineral alteration as well as their implications for the creep behavior of the Ismetpasa creeping segment of the North Anatolian Fault. We address in particular the following points: (1) the spatial correlation between the observed present-day creep behavior and the mineral composition of the gouge;

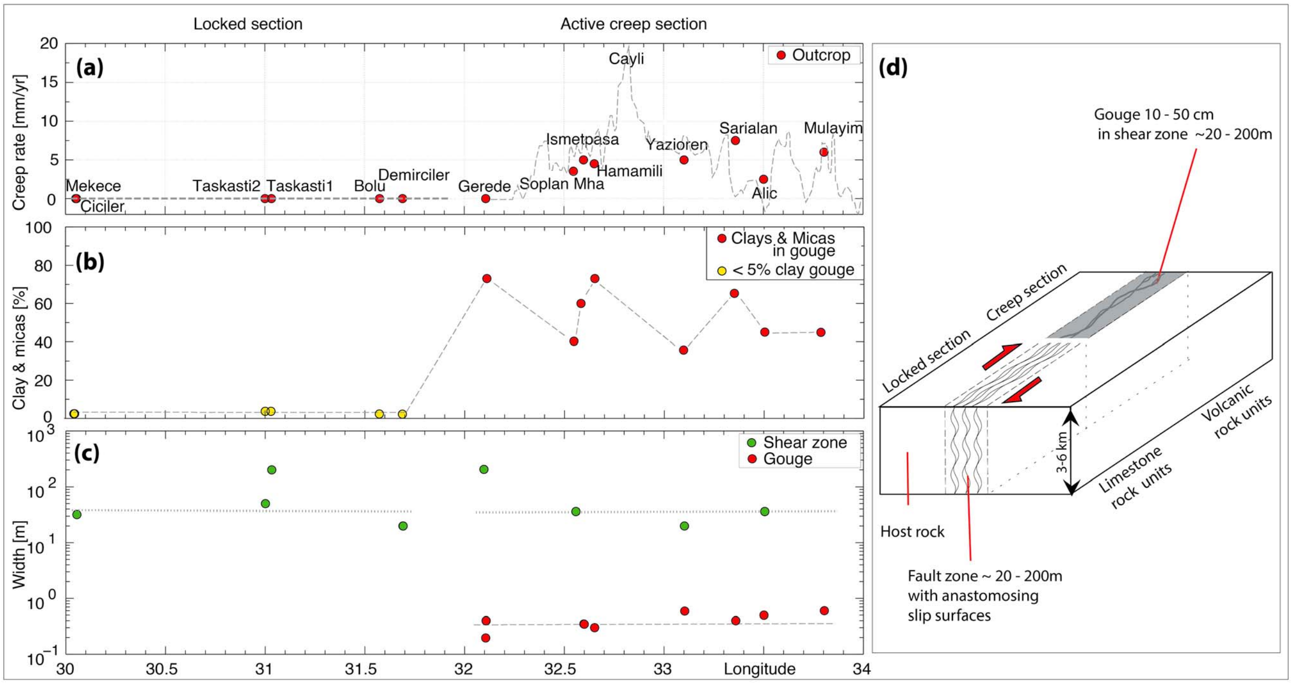

Figure 15. Comparison of locked and creeping zones: (a) Creep rate versus longitude along the North Anatolian Fault from *Cetin et al.* [2014]. The red points indicate the available outcrops where the fault zone is clearly visible in the field and where samples were collected (see Figure 1 and supporting information for locations). (b) Amount of clay and mica minerals in the gouge versus the longitude along the fault. Note the abrupt change in clay and mica content between the locked (limestone units) and the creeping (volcanic units) segments. (c) Width of shear zone or gouge versus the longitude showing the drastic change between limestone and volcanic rocks. (d) Sketch representing the locked segment with a wide shear zone and anastomosing slip surfaces hosted in the limestone rock unit, while the creeping segment has a limited number of branches of localized gouge in a similarly wide shear zone hosted in volcanic units.

(2) the mechanisms of mass transfer, segregation and layering at various scales, and the time-dependent change in fault zone mineralogical and structural properties; (3) the mechanisms of metamorphic mineral transformations that contribute to the creeping processes; and (4) the mechanisms of the aseismic creeping processes.

4.1. Spatial Correlation Between Creep and Gouge Mineral Composition

In the past decade, a considerable amount of data has been collected from experiments, drilling projects, and field studies, showing that the frictional properties of rocks are dependent on the type of minerals, mineral content of the gouge, and water content [*Carpenter et al.*, 2011; *Lockner et al.*, 2011; *Carpenter et al.*, 2016]. Furthermore, experiments on a synthetic clay gouge show that an almost negative linear trend exists between the amount of clay content and the coefficient of friction [*Samuelson and Spiers*, 2012]. Experimental data show that the presence of saponite has a weakening effect, due to low friction $\mu \approx 0.1$ [*Lockner et al.*, 2011; *Mittempergher et al.*, 2011; *Carpenter et al.*, 2011]. The pure muscovite gouge exhibits a higher friction coefficient $\mu \approx 0.3$. This coefficient becomes much higher, up to 0.8, if the sample contains pure quartz or calcite [*den Hartog et al.*, 2013] or differing amount of strong minerals [*Bullock et al.*, 2015, and references therein]. Hence, it is important to understand the nature of the interplay between creep and mineral composition of the gouge.

Figure 15a shows the creep rate along the North Anatolian Fault measured by *Cetin et al.* [2014]. The maximum creep rate value has been measured in the vicinity of the Cayli settlement (although this maximum value has been revised to a lower rate by *Hussain et al.* [2016b]) and is close to the present-day relative motion of 22 ± 5 mm/yr between the Anatolian and European Plates [*Reilinger et al.*, 2006]. In order to compare the gouge composition with the creeping rate along the fault, the amount of clay and mica minerals in the gouges was plotted with respect to longitude (Figure 15b). The locked segments appear as a deformation zone with width in the range 20–200 m (Figure 15c) that contain numerous fractures and cataclastic zones and very thin mirror-like slip surfaces (Figure 2) that are considered as indicative of fast (seismic) sliding

[*Fondriest et al.*, 2013]. It has been suggested that such features may also develop at lower sliding [*Verbene et al.*, 2014]. However, the observed high Fe oxide content along these mirror-like faults, which could result from decarbonation process that passively concentrated Fe oxides due to carbonate dissociation [*Rowe et al.*, 2012, *Collettini et al.*, 2013], is also in favor of seismic behavior. In overall, the gouges have almost the same composition as the limestone rocks containing less than 5% of clay minerals. Finally, it must be noted that when canceling the 80 km offset of the fault, the locked segment shows on both sides units of limestone and carbonate clastics since the initiation of the fault (see section 3.1 and Figure 1b).

Conversely, the Ismetpasa creeping segment appears as composed of gouge branches with width in the range 10–50 cm in sheared and fractured damage zones of 20–200 m width (Figure 15c). Along this creeping segment a dramatic change in gouge composition is seen with respect to the locked segment with high clay contents (smectite and kaolinite, as well as other phyllosilicates such as micas, ranging from 40 to 80%, Figure 15b). The gouges are within volcanic units. They result from transformations under stress in actively deforming zones (Figures 6–8 and 10), and such changes are discussed in more details in the section 4.2 below. Note that although there is a clear correlation between the existence of creep and the clay content, the correlation between the creep rate and the clay content is not perfect. For example, the Gerede zone, with a maximum clay and mica content, is located near the west end of the creeping segment where creep rate is small. However, it is not completely certain that we sampled the most present-day active creeping zone. Several parallel creeping zones were often observed in the field (Figure 4a). Moreover, the creeping zone may shift after earthquakes, as observed in the San Andreas Fault (SAF) where the SAFOD drilling project revealed two localized actively creeping zones, 50–200 cm thick, 100 m apart, containing saponite [*Lockner et al.*, 2011; *Hadizadeh et al.*, 2012], one sliding much faster than the other. Another major limitation of our study along the NAF is that based on geological outcrops alone, it is not possible to properly characterize the geology and mineralogical composition of the gouge of the fault at depth. This is important because gouge composition can change with depth by mineralogical transformation and alteration [*Chester et al.*, 2004; *Scholz*, 2006]. Such changes can be crucial for creep behavior [*Richard et al.*, 2014]. At the present time, there are no deep drilling data available on the Ismetpasa creeping segment of the North Anatolian Fault. So one can only conclude that there is an overall correlation between the gouge composition observed near the surface and creep, as locked segments do not contain a significant amount of clay and mica minerals and no saponite and montmorillonite, whereas the gouge along the investigated creeping segment contains large amounts of these minerals. However, due to the regional uplift in the area [*Yildirim et al.*, 2011], we can reasonably assume that the sampled rocks in the gouge gather samples deformed at various depths, from the surface to several kilometers deep. Finally, one must note that at the present day, the offset of the NAF has put volcanic units and limestone units face to face in some place along the Ismetpasa segment (see section 3.2). However, if the 80 km total offset is canceled, the whole volcanic unit of the Galatia massif in the southern compartment of the fault becomes face to face with its northern volcanic part. This indicates that at the beginning of the transformation of the creeping fault segment the volcanic units where face to face and the creeping process initiated and developed in a volcanic unit.

To summarize, at shallow depth (upper 0–6 km), the locked segments are characterized by an absence of present-day creep and a wide seismic deformed zone with anastomosing slip surfaces hosted in limestone rocks without clay gouges. Conversely, the Ismetpasa creeping segment is characterized by creep rates up to 20 mm/yr and localized clay gouge bands in shear zones hosted in volcanic units (Figure 15d). Due to the uplift and associated erosion processes of the NAF fault rocks [*Yildirim et al.*, 2011], the mechanisms observed on the outcropping samples are representative of most of the creeping zone at depth.

4.2. Mechanisms of Mass Transfer, Segregation and Layering at Various Scales, and Time-Dependent Change in Fault Properties

Major faults such as the NAF are likely to act as major fluid channel pathways and zone of fluid rocks reactions. We have described in section 3 several circumstantial evidences of this presence and effect of fluids that are further discussed below. From a general point of view, in natural deformation, mass transfer occurs by two types of mechanism: diffusion through a fluid phase driven by chemical potential differences and advection by fluid flow driven by hydraulic gradients. According to the experiments of *Ildefonse and Gabis* [1976], the maximum distance of diffusive mass transfer over geological times is limited at best to a few meters in the case of mass transfer through a free fluid phase (fluid in open fractures, for example).

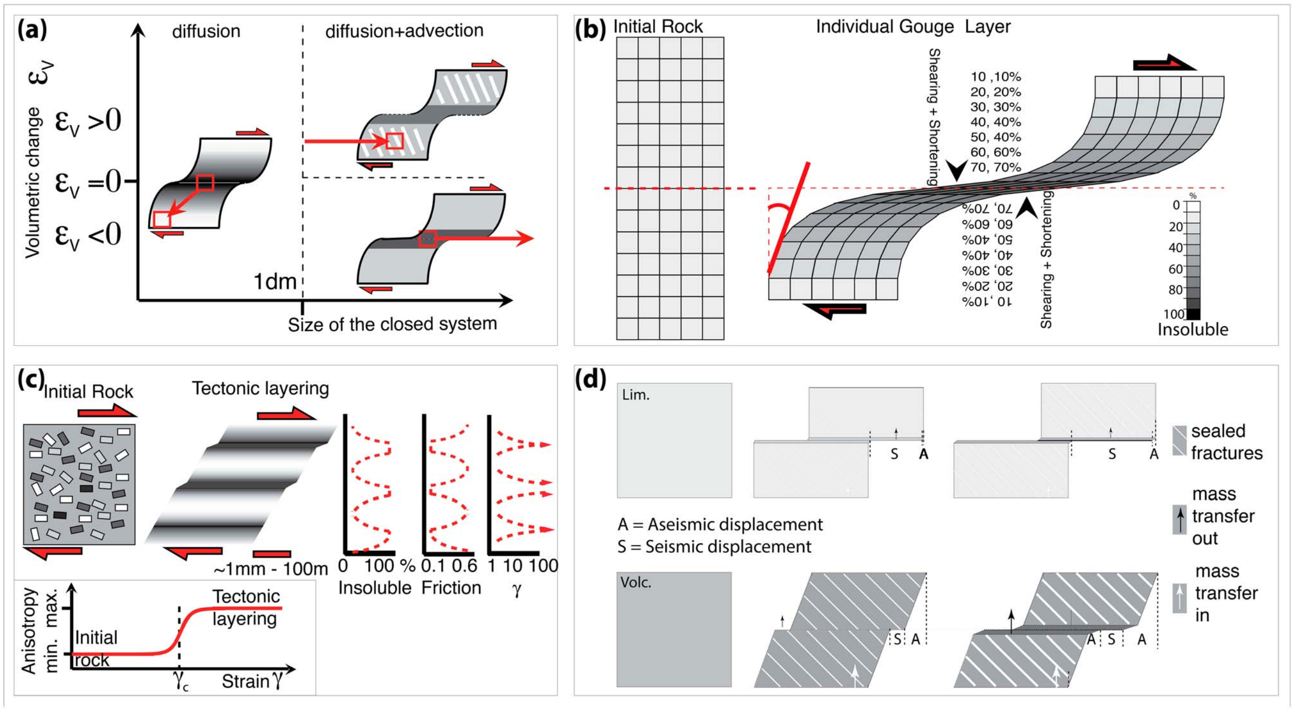

Figure 16. General concepts of tectonic layering and rock transformations. (a) Three types of mass transfer in a diagram showing volume change versus mass transfer distance: mass transfer by diffusion in a closed system over a distance of less than a decimeter (left) and coupled diffusion-advection over greater distances (right) with either a volume gain (veins in damage zone, top) or volume loss (dissolution in the gouge, bottom). (b) Model of passive concentration of insoluble minerals (black) in shear zone with volume loss. (c) Model of tectonic layering development at all scales after critical shear strain, leading to anisotropic rocks with alternations of strong and weak material, with high/low friction coefficient and low/high accommodation of shear strain, respectively. (d) Contrast in limestone and volcanic rocks deformation: limestone deforms by seismic displacement (S) with only very minor postseismic aseismic displacement (A) (top) and volcanic rock deforms by both seismic (S) and aseismic (A) displacement associated with a chemical change in the rocks with mass transfer in and out of the fault zone, leading through time (from left to right) to gouge softening and damage zone strengthening (bottom).

However, most of the time in deformed zones diffusive mass transfer occurs along reactive fluid phases that are trapped under stress at grain boundaries, or in stylolites, or in cleavage planes [*Wheeler*, 2014]. In such cases, the diffusion paths are very thin (see below) and the maximum distance of diffusive mass transfer is reduced to values ranging from a few decimeters to a few centimeters or even less. Mass transfer may occur in closed or open systems. The system is closed if the amount of dissolution is equal to the amount of redeposition and the total solid mass is conserved. Otherwise, the system is considered to be open and the initial rock can lose or gain volume as a result of transport of mobile elements.

4.2.1. Mass Transfer at the Grain Scale

At the grain size scale (μm-mm), various models are used for fluid phases trapped along grain boundaries, from very thin continuous phases to clouds of fluid inclusions. However, the diffusive path width is sufficiently small to be the controlling factor of pressure solution or metamorphic reactions in nature [*Rutter*, 1976*; van Noort et al.*, 2008*; Gratier et al.*, 2013a*; Wheeler*, 2014]. This explains the observed main difference between monomineralic rocks and polymineralic rocks. Monomineralic rocks do not deform at grain scale in the locked segment (Figure 3) and are hardly deformed at grain scale in some parts of the creeping zone except by dissolution along microstylolites at veins (Figures 11e, 11f, and 12d–12i) or quartz clasts boundaries (Figure 13g). Conversely, polymineralic rocks in the creeping segment show very efficient dissolution at grain scale leading to the dissolution of a large part of the more soluble grains (Figures 8a, 8b, 8e, 9d, and 9e). The reason for this is that diffusion at the contact between two identical minerals, whose boundaries are most often healed, is much slower than diffusion at the contact between minerals of different nature where the fluid phase boundary is more continuous [*Zubtsov et al.*, 2004]. The difference is even greater if one of the minerals is a phyllosilicate, which prevents healing [*Bos and Spiers*, 2000] or activates dissolution [*Renard et al.*, 2001].

4.2.2. Mass Transfer at the Mesoscale, Tectonic Layering, and Size of the Closed System

At the mesoscale, various types of structures are observed, such as tectonic stylolites, cleavages, and foliations more or less associated with veins of various sizes in the closed system. In the locked segments, tectonic stylolites are associated with tension gashes veins (Figure 3e) that have the same composition as the dissolved minerals. Even though it is not easy to evaluate exactly the size of the closed system, a mean distance of diffusive mass transfer can be evaluated, ranging from 1 to 10 cm. A schematic representation of this behavior based on diffusion-driven mass transfer is shown on the diagram of volumetric strain plotted against the size of the closed system (Figure 16a). The size of a near closed system is smaller than 1 dmr with conservation of volume ($\varepsilon_v \approx 0$).

In the volcanic rocks of the creeping segment, tectonic layering has developed at various scales from centimeter to micrometer width (Figures 6–8 and 10) leading to a foliation structure. Various markers such as rolling clasts (Figure 12i), asymmetrical folds (Figures 13f and 14f–14i), and cleavage planes at various angles to the main slipping zone (Figures 10a–10c and 12d) show that such layering developed during a shearing process more or less parallel to the present-day active right-lateral fault zones. Such layering is visible both in the present-day gouges and in the damage zones, although in the latter case successive veins have partially obliterated the initial tectonic layering (Figures 5a–15d and 14e). This layering process was thus a relatively early process. It began before the massive episodes of intense fracturing and sealing of the damage zone, but it was also reinforced by the first carbonate vein sealing episodes that prevented the dissolution of the more calcitic-silicate layers (Figures 12g and 14h). Such layering is frequently observed in deformed rocks. It can develop by a purely mechanical effect as shown experimentally by *Barnhoorn et al.* [2005], but in such a case this effect only starts to appear for very large shear strain values of more than 10. Conversely, it has been shown, also by experiment, that layering can develop at much lower strain values as a result of stress-driven chemical effects by dissolution of soluble elements and the passive concentration of insoluble elements [*Gratier et al.*, 2015]. The foliation layering that develops here is clearly associated with this latter process with dissolution of quartz and feldspars and passive concentration of more insoluble minerals such as phyllosilicates and Fe and Ti oxides (Figures 8a, 8b, 8e, 9d, and 9e). It is a self-organized process: stress-driven dissolution of the soluble minerals is initiated in the areas initially richer in insoluble species as diffusive mass transfer along the interface between soluble/insoluble minerals is much faster than along the healed boundaries of the soluble minerals (see above). The passive concentration of the insoluble minerals amplifies the dissolution along layers oriented perpendicular to the maximum compressive stress. Conversely, in areas with an initial low content of insoluble minerals and clustered soluble minerals, dissolution is slower. Consequently, these areas are less deformed. They may show redeposition of the dissolved species (Figure 5e) or not (Figures 8a and 13d). They may also host the deposition of soluble carbonate minerals (Figures 12g and 14h) coming from outside (see section 4.2.3 below). In any case, they act as rigid objects that concentrate the dissolution near their boundaries, thus amplifying the differentiation and development of layered microstructures.

It is possible to estimate the mass transfer that occurred at the layering scale when comparing the mineralogical composition of the more deformed (exposed) zones relative to the zones that have been more protected from deformation. The relative mass change is: $\Delta M/M = (I_p/I_e) - 1$, $\Delta M/M$ being the relative mass change and I_p and I_e the concentrations of the whole insoluble minerals in the protected and exposed zones, respectively. As the porosity of the rock does not change to any significant degree, this mass change may be assimilated to a volume change. This relation may be used on various examples in order to evaluate the mass transfer. In Figure 8b when comparing a clast of initial rock that has been protected from deformation with zones that have been subject to greater deformation, a relative decrease in volume of -60% ($I_p = 23\%$ and $I_e = 60\%$) was found. In Figures 9d and 9e a relative decrease in volume of -40% ($I_p = 48\%$ and $I_e = 80\%$) was found. In both cases, the mobile minerals are mainly feldspars and quartz. In Figure 7d, quartz appears to behave as an insoluble mineral, which may happen if the deformation temperature is very low, with a volume change due to feldspar dissolution of about -50% ($I_p = 33\%$ and $I_e = 67\%$). An example of such behavior is modeled in Figure 16b: during shearing, the differentiation occurs with progressively increasing strain toward the center of the layer. Far away from the median axis, the rock composition does not change. As one gets closer to the median axis, each cube in the grid deforms by superposition of 10% simple shear and 10% shortening with 10% volume loss. These measurements are made at centimeter to decimeter scale, but the same layering process occurs from decimeter to micrometer scale.

When considering the wide foliated shear zone that includes both the present-day gouges and the damage zone in the early times (Figure 4), the question is to know where the soluble matter was transported. At small scale, part of this material may have reprecipitated in quartz veins (Figure 5e) but this is rarely seen. Part of the feldspars was transformed into clay minerals by metamorphic reactions (Figures 8f and 8g; see section 4.3 below). However, the major part of the soluble minerals probably left the shear zone, which was an open system (Figure 16a). Due to the size of the system, advection mass transfer associated with fluid circulation must have controlled the evacuation of mobile elements. However, the kinetics of the overall transfer was probably limited by the diffusion rate along the trapped fluid phase as discussed above.

4.2.3. Mass Transfer at Fault Scale, Fault Zone Segregation, and Size of the Closed System

As mentioned above, the layering process developed in a large shear zone that progressively evolved into the present-day gouges and damage zones. Two parallel processes controlled this evolution. The first one is fracturing and sealing of the damage zones (Figure 16a), tending to strengthen this zone because large veins of monomineralic carbonates are very difficult to deform by dissolution even if a certain amount of dissolution can be seen at their boundaries (Figures 5f, 5g, 11e, and 11f). Evidence of large veins that stop deformation is found everywhere (Figures 12d–12i). The second process is pressure solution creep that remains active in the gouge, facilitated by the concentration of insoluble minerals in a self-organized system, as described above (see section 4.2.2). The layering inherited from the development of large shear zones is amplified in the gouge. Note that the first calcite veins that probably developed at the same time in the proto-gouges and damage zones are sometimes folded in the gouge (Figures 14f–14i), probably because they were thinner than the latter veins. The thinner are the veins, the shorter are the paths of diffusive mass transfer from the intrados to the extrados of the folds and consequently the faster are the folding processes. However, this reflects a continuous change, as indicated by the folding of the foliation (Figure 13f). It must be noted that such an opposite volume change between (i) fault gouge with volume loss by mechanical wear and dissolution and (ii) damage zone with volume increase with carbonates and zeolites veins is also described in other faults such as the Nojima Fault [*Tanaka et al.*, 2001].

The huge amount of carbonates that sealed the fractures in the damaged rocks, sometimes up to 90% in very large areas (Figure 4d), cannot originate from the volcanic rocks but must come from nearby limestone massifs. Consequently, an enormous mass transfer was required to accommodate this segregation process between gouge and damage zone, with a two-way fluid flux in order to (i) evacuate the dissolved species from the fault zone and (ii) bring into the fault zone the carbonates that filled the veins and some fluids that contribute to the metamorphism of the gouge (see section 4.3 below). It is likely that the flux inversions were linked to earthquakes [*Sibson*, 1990], the shear zones having been probably associated with earthquakes with postseismic inflow and interseismic outflow. Evidence of such seismic behavior can be found in historical records and the recent period [*Kondo et al.*, 2005]. Earthquakes have occurred repeatedly over geological timescales, as attested by the cataclastic gouges (Figure 11d) and intense networks of carbonates veins (Figures 5a, 6d, and 14e) with euhedral mineral sealing (Figure 5c) that reflect the fast void openings commonly associated with seismic events [*Gratier et al.*, 2013a]. The high Mg content (dolomite and magnesite) or Fe content (siderite) of these veins probably reflects the relatively high temperature of the fluids coming from depth after each earthquake [*Montes-Hernandez et al.*, 2016]. Evidence of CO_2-rich springs seeping along the fault, as trails of CO_2 bubbles that are seen in a pond at the Ismetpasa outcrop and travertine carbonate deposition [*Temiz et al.*, 2013], bears witness to the present-day regional fluid flux. Moreover, permeability in the gouges and damage zones varies over an enormous range during the seismic cycle, depending on rock type and fracture connectivity. In this context, the intriguing veins parallel to the cleavage (Figures 5a, 10a, 10b, and 14j) may be explained either by stress rotation or by hydraulic fracturing due to local overpressure [*Mittempergher et al.*, 2011] or by chemically activated subcritical cracking processes [*Brantut et al.*, 2013]. Hydraulic fracturing may develop parallel to the cleavage if the sum of the stress normal to the cleavage and the cleavage tensile strength is lower than the stress parallel to the cleavage and the rock tensile strength [*Gratier et al.*, 2013a]. This happens mainly at depth in the context of lithological fluid pressure [*Jefferies et al.*, 2006b]. However, for a crack-sealing process (Figure 5b) it is impossible to rule out other possibilities of sealing driving forces, such as the crystallization force associated with CO_2 degassing of oversaturated fluid [*Noiriel et al.*, 2010], which is more likely in a near-surface context [*Gratier et al.*, 2012].

It should be noted that several parallel gouges could develop, simultaneously or successively (Figure 4). Conceptually, it is the same self-organized system that the foliation development described above [*Gratier* *et al*., 2015], but at regional scale (Figure 4a). This phenomenon is represented as a sketch in Figure 16c, where mineral differentiation coupled with fracture sealing controls the formation of layers with high and low friction and low and high strain localization, respectively. The transition from strong to weak behavior could possibly result from a phase transition of the rock structure from isotropic to anisotropic [*Collettini et al*., 2009]. When the shear strain is greater than a critical shear strain $\gamma > \gamma_c$, weak zones start to separate from strong zones and form alternating strong and weak zones with high and low friction values, respectively. Most of the creep deformation occurs in the weak zones (Figures 6f and 12h), whereas strong zones deform by fracturing (Figures 3a–3e and 12g).

4.3. Gouge Metamorphism and Phase Transformation

Along the North Anatolian Fault, evidence of the transformations of mica, chlorites, or feldspars to weak clay minerals is observed. Temperature and pressure vary with depth in the first few kilometers of strike slip faults as a result of tectonic forces, geothermal gradients, and fluid circulation. With typical geothermal (25°C km^{-1}) and lithostatic gradients, the temperature at 6 km depth is up to 150°C, and the lithostatic pressure is up to 150–170 MPa. Under these conditions, volcanic rocks alter and produce weak minerals, including saponite [*Andrews*, 1980*; Gíslason et al*., 1996*; Wilson*, 2004]. Such alteration is also found in other places where volcanic rocks weather, such as Iceland [*Gíslason et al*., 1996]. Plagioclases and phyllosilicates such as mica and chlorite transform into kaolinite and then to smectite (montmorillonite and saponite) as a result of hydrothermal fluid circulation along the fault [*Deer et al*., 2013]. Goethite and smectite can form as products of volcanic rock alteration, with goethite forming first, followed by smectite and a small amount of zeolites. Our XRD analyses of creeping gouges reveal the presence of these clay minerals and even ~1% of natrolite (zeolite group) (Figure 8c). This supports the idea of volcanic rock alteration into weak clay minerals. At the grain scale, the mineralogical changes occurring between protected and deformed zones can be seen in the gouge in the outcrop west of Ismetpasa (Figures 8f and 8g). For instance, in the initial (protected) state (in the undeformed volcanic clast), the plagioclase-rich clasts are composed of anorthite cores coated with labradorite and without any preferred orientation of the grains. Conversely, in the foliated gouge, all grains have lost their labradorite coating. Moreover, in addition to losing their coating, some grains lose at least 75% of their original size, with all their long axes aligned subparallel to the shear direction.

Along minor faults in serpentines, only minor changes in the chemical composition of the rock are measured, and there is no evidence of a well-developed gouge, nor is any smectite detected in the XRD data (Figure 8c). In the absence of significant tectonic or metamorphic transformations, the serpentines do not appear to be weak rocks.

It is worth noting that only part of the phyllosilicate and feldspar minerals is transformed into soft clay. Theoretically, the transformation of labradorite into smectite is driven by fast kinetics, with typical timescales of the order of one to several years [*Aharonov et al*., 1998*; Tenthorey et al*., 1998]. However, plagioclase dissolution rates are strongly dependent on composition and pH [*Gudbrandsson et al*., 2014]. Moreover, evidence of fast kinetics is most often found in the laboratory for free-face metamorphic reactions in experiments where minerals are under fluid pressure. In active deformed zones, the reactions must occur in fluid phases that are trapped under stress and, in this case, the kinetics of the reaction is controlled by the diffusive mass transfer flux along these fluid phases (see discussion in section 4.2) and the process is very slow [*Wheeler*, 2014].

The timing of these metamorphic transformations may affect creep deformation in two ways: (i) either insoluble minerals (micas, chlorites, etc.) are first passively concentrated in the gouge and then transformed into weak minerals such as smectite or kaolinite or (ii) metamorphic transformations occur first and then the weak minerals are passively concentrated in the gouge.

If metamorphic transformations occur first at a local scale with diffusion-controlled mass transfer, the transformed volume will remain small covering a maximum distance of just a few meters according to the experiments of *Ildefonse and Gabis* [1976]. The effect on the creep process will then be minimal. If such metamorphic transformations occur first but along fractures before gouge development, the gouges will also be diffuse and disconnected, again with a minimal effect on the creep process. Conversely, if metamorphic transformations occur after the passive concentration of phyllosilicates by pressure solution, and on some large feldspars that had not been dissolved previously, they will be more efficient for facilitating creep as they occur in gouges that are already regionally connected. Transformations that occur along planar interconnected layers of the gouge greatly facilitate the amplification of the creep process [*Holdsworth et al.*, 2011]. Moreover, we see plenty of evidence of early brittle and even comminution processes associated with early seismic events and associated interseismic pressure solution processes (Figures 7, 8, 11, and 12). Reducing the grain size increases the reaction rates (see below section 4.4, point 3) facilitating the localization of the pressure solution and metamorphic processes (see above section 4.2.2). This testifies of a partitioning of the deformation alternating fast brittle and slow creep processes. Such coupled brittle and ductile deformation have been described on other faults as in the Outer Hebrides Fault Zone and the Great Glen Fault in Scotland and in the Median Tectonic Line in Japan [*Stewart et al.*, 2000; *Imber et al.*, 2001; *Jefferies et al.*, 2006a]. The formation of smectite has also been related to the infiltration of hydrothermal fluid, as reported for the Wenchuan Earthquake fault [*Chen et al.*, 2013b] and the Chelungpu thrust fault [*Isaacs et al.*, 2007]. In the case of the North Anatolian Fault, these transformations could have occurred relatively early in proto-gouges that were later included in vein networks of the damage zones (Figures 5f and 5g). This is consistent with the observations of high fluid fluxes associated with the postseismic processes described above. Such large fluid transfers along the gouge have two effects: the transformation of relatively rigid minerals into weak minerals that soften the gouge and the extensive deposition of soluble carbonate minerals in the damage zone, which strengthen this zone.

4.4. Aseismic Creep Mechanisms

First, it should be noted that both creeping segments and currently locked fault segments actually show considerable geological evidence of creep (Figures 3–14). Creep is still active along the Izmit and Ismetpasa segments, since the 1999 Izmit and 1944 Dücze earthquakes, while some of it is fossil and was associated with afterslip and postseismic creep following older major past earthquakes. This section discusses the four types of mechanism of creep in present-day and past creeping and locked segments.

Numerous occurrences of stylolites and cleavage, associated with veins to a varying extent, and dissolution features at grain scale (Figures 3–14) bear witness to an efficient process of pressure solution ductile deformation. The pressure solution viscous creep law, derived from experiments [*Rutter*, 1976*; Bos and Spiers*, 2000; *Gratier et al.*, 2011], states that the strain rate is inversely proportional to the cube of the diffusive mass transfer distance along the fluid phase that is trapped under stress. Consequently, it is possible to evaluate the relation between the mass transfer distance inferred from our observations and the displacement rate and width of the deforming zone.

1. In the currently locked zones, pressure solution is associated with mass transfer distances of 1 to 10 cm. However, the highly stylolitic zones with 1 cm transfer are rather narrow (1 m width at most), and those with 10 cm transfer distance are found only over a small width of the total damage zone (10 m at most). At 5 km depth, for calcite [*Gratier et al.*, 2011], a 1 cm mass transfer distance in a 1 m shear zone could potentially lead to a strain rate of 2.6×10^{-15} s^{-1}, which corresponds to a displacement rate of 0.15 μm/yr, and for a 10 cm mass transfer distance in a 10 m wide shear zone the displacement rate would be 0.0015 μm/yr. Clearly, it is not possible to measure and record such very low displacement rates with classical surface geodetic measurements. So even if creep is active, the zone still appears locked.
2. In the wide shear zones preceding gouge development, pressure solution cleavage was associated with foliation development. In this case, if the diffusive mass transfer distance for feldspar and quartz dissolution was of the order of the foliation width (1 mm), a shear zone of 10 to 50 m width could potentially have accommodated a displacement rate of 10 mm/yr [*Gratier et al.*, 2011].
3. An increase in shear leads to the distortion of cleavage surfaces from 45° at the initial step to near 0° after a large shear displacement [*Ramsay*, 1967], as observed in our data (Figure 10a). When cleavages are distorted down to low angles with respect to the gouge, the creep mechanism changes to a grain boundary sliding process accommodated by a pressure solution diffusion mechanism. However, this mechanism of grain boundary sliding can only develop if the gouge contains a significant amount of soluble species as in some foliated gouges of the creeping segment (Figures 8e, 12h, and 14g). This mechanism is geometrically analogous to the superplasticity process described by *Ashby and Verrall* [1973]. It can accommodate almost infinite shear strain values, and the strain rate is inversely proportional to the cube of the grain size. It was suggested that superplasticity occurs at high temperatures in dry rocks either in the bulk grain mineral or at their boundaries [*Boullier and Gueguen*, 1975]. It was even suggested that thin films of

nanogranular fault rock could allow superplasticity to accommodate unstable seismic fault slip [*Verbene et al*., 2014]. Here at 5 km depth in wet rocks, assuming a mean value of 10 mm/yr and a gouge width of 50 cm, and due to the inverse relation between strain rate and cube of the grain size, the maximum grain size for feldspars and quartz would range from 200 to 400 μm, respectively [*Gratier et al*., 2011]. If the gouge were thinner (10 cm), the required grain sizes would be smaller, ranging from 100 to 250 μm. When considering the thin sections, it is clear that the easily deformed part (weak foliation layers, Figures 8e, 12h, and 14g) was made up of a material with a much smaller grain size than required, so active pressure solution creep is a possible mechanism. In the part that does not deform easily (strong granular or calcitic-silicate layers that break or are disrupted), the grain size is close to or greater than these maximum values required to develop grain boundary sliding (Figures 8e and 13d). This shows that pressure solution is a major mechanism governing aseismic sliding in wet rocks at low temperature in the presence of small-size soluble minerals. Diffusion occurs along a fluid water phase trapped at the boundary of the minerals and is activated by the presence of insoluble species such as phyllosilicate minerals.

4. Finally, in some of the gouge with low soluble species content where most of the soluble species (quartz and feldspars) have been dissolved or can no longer be dissolved because they are too dispersed, the gouge contains localized layers of phyllosilicate and clays minerals. The phyllosilicates are most often well reoriented, whereas the clays (smectite) show no preferred mineral orientation (Figures 5f and 6f). In this case, the friction of the gouge depends on the friction of individual minerals and on the geometry of their assemblage [*Moore et al*., 1997*; Carpenter et al*., 2011*; Lockner et al*., 2011*; Sone et al*., 2012*; Carpenter et al*., 2016] or on a combined frictional and viscous flow behavior [*Bos and Spiers*, 2002]. In the North Anatolian Fault example, the friction becomes very low because of the passive concentration of phyllosilicates that progressively transform into smectites, which appear in layering at various spatial scales in the range 10^{-5} m to 10^{-2} m.

From a general point of view, and to summarize the discussion, the contrast in change in limestone and volcanic rock deformation is shown in Figure 16d: (i) limestone units deform mainly by seismic displacement with only very minor postseismic aseismic displacement, and this behavior is stable with time, and (ii) volcanic rock units deform by both seismic and aseismic displacements associated with a chemical change in the rocks during geological times involving mass transfer in and out of the fault zone. This leads to gouge softening and damage zone strengthening and a change from diffuse to localized seismic-aseismic zones. Such mineral transformation can lead to permanent or transient aseismic sliding, as observed in other creeping faults that contain similar material such as the San Andreas Fault in California [*Lockner et al*., 2011; *Richard et al*., 2014] and the Long Valley Fault [*Thomas et al*., 2014a, 2014b]. It might be worth to note that the clay-rich fault gouges generally have lower permeabilities than clay-free gouges, which may also affect the runaway process of an earthquake, e.g., by thermal or thermochemical pressurization [*Wibberley and Shimamoto*, 2003; *Chen et al*., 2013a].

5. Conclusions

Based on the observations of fault zone outcrops along the North Anatolian Fault, the main findings of the present study can be summarized as follows:

1. There is a clear correlation between shallow creep and near-surface fault gouge composition. The locked fault segments consisting of massive limestone without any clay gouge are deformed mainly seismically. The creeping segments are located in volcanic units that show decimeter-thick clay gouges with high phyllosilicate and clay minerals content; they accommodate displacement along fault both by seismic and aseismic slip.
2. The clay gouges in the creeping segments result from a progressive change of the initial volcanic rocks during their deformation. A large damage zone is initially formed by shearing during the first stage of displacement, leading to layering development obliquely then subparallel to the fault that accommodates part of the aseismic displacement by pressure solution creep. Soluble minerals, mainly quartz and feldspars, are dissolved and evacuated for the most part by fluid advection out of the deforming zone during interseismic periods, leading to passive concentration of phyllosilicates in the gouges.
3. The damage zones, in parallel, are fractured by seismic events, and numerous fracture networks are sealed by carbonate minerals coming from outside during postseismic inflow. This fluid inflow also induces

metamorphic transformations of the passively concentrated phyllosilicates, and of some large feldspars not previously dissolved, producing low-friction clay minerals such as kaolinite and smectite. As a result, these mineralogical and structural transformations weaken the gouges and strengthen the damage zones, leading to a change from diffuse to localized seismic-aseismic zones.

4. The mechanisms of aseismic creep are a combination of pressure solution creep and friction sliding. These mechanisms evolve with time. Pressure solution creep is the driving force in early shear zones with the development of cleavage and layering. It is subsequently superseded by grain boundary sliding in the gouges, which still contain soluble minerals. In places where the soluble species have been completely dissolved or can no longer be dissolved because of their dispersion, then low-friction minerals control aseismic sliding.

Acknowledgments
This project was funded by the European Union's, Seventh Framework Programme for research technological development and demonstration under grant agreement 316889 (ITN FlowTrans) and by the CNRS-INSU (programs Syster and ALEAS). This work has been supported by a grant from Labex OSUG@2020 (Investissements d'avenir - ANR10 LABX56) and by the Frinatek grant 250661 (HADES) from the Norwegian Research Council. The authors would like to thank N. Findling, V. Magnin, and V. Batanova for technical support with measurement equipment at ISTerre, A.-M. Boullier for her help in microstructural analyses, and B. Rousset and F. Aben for their help on the field. The microstructural and mineralogical data in the present study can be requested from the corresponding author. We thank R.E. Holdsworth and three anonymous reviewers for their comments that significantly improved the manuscript.

References

Akbayram, K., C. C. Sorlien, and A. L. Okay (2016), Evidence for a minimum 52 ± km of total offset along the northern branch of the North Anatolian Fault in northwest Turkey, *Tectonophysics*, *668–669*, 35–41, doi:10.13140/RG.2.1.4160.8729.

Adiyaman, Ö., J. Chorowicz, O. N. Arnaud, M. N. Gündogdu, and A. Gourgaud (2001), Late Cenozoic tectonics and volcanism along the North Anatolian Fault: New structural and geochemical data, *Tectonophysics*, *338*(2), 135–165, doi:10.1016/S0040-1951(01)00131-7.

Aharonov, E., E. Tenthorey, and C. H. Scholz (1998), Precipitation sealing and diagenesis: 2. Theoretical analysis, *J. Geophys. Res.*, *103*(B10), 23,969–23,981, doi:10.1029/98JB02230.

Akbaş, B., et al. (2016), Turkey geology map general directorate of mineral research and exploration publications, Ankara Turkey.

Ambraseys, N. N. (1970), Some characteristic features of the Anatolian fault zone, *Tectonophysics*, *9*(2–3), 143–165, doi:10.1016/0040-1951(70)90014-4.

Andrews, A. J. (1980), Saponite and celadonite in layer 2 basalts, DSDP Leg 37, *Contrib. to Mineral. Petrol.*, *73*(4), 323–340, doi:10.1007/BF00376627.

Armijo, R., B. Meyer, A. Hubert, and A. Barka (1999), Westward propagation of the North Anatolian fault into the northern Aegean: Timing and kinematics, *Geology*, *27*(3), 267, doi:10.1130/0091-7613(1999)027<0267:WPOTNA>2.3.CO;2.

Armijo, R., B. Meyer, A. Hubert, and A. Barka (2000), Westward propagation of North Anatolian fault into the northern Aegean: Timing and kinematics—Comment and reply, *Geology*, *28*(2), 188, doi:10.1130/0091-7613(2000)28<188:WPONAF>2.0.CO;2.

Armijo, R., et al. (2005), Submarine fault scarps in the Sea of Marmara pull-apart (North Anatolian Fault): Implications for seismic hazard in Istanbul, *Geochem. Geophys. Geosyst.*, *6*, Q06009, doi:10.1029/2004GC000896.

Ashby, M., and R. Verrall (1973), Diffusion-accommodated flow and superplasticity, *Acta Metall.*, *11*(2), 149–163.

Atkinson, B. K. (1984), Subcritical crack growth in geological materials, *J. Geophys. Res.*, *89*(B6), 4077–4114, doi:10.1029/JB089iB06p04077.

Barbot, S., N. Lapusta, and J.-P. Avouac (2012), Under the hood of the earthquake machine: Toward predictive modeling of the seismic cycle, *Science*, *336*(6082), 707–710, doi:10.1126/science.1218796.

Barka, A. (1992), The North Anatolian fault zone, Ann, *Tectonicae*, *6*(Suppl), 164–195.

Barka, A., and R. Reilinger (1997), Active tectonics of the Eastern Mediterranean region: Deduced from GPS, neotectonic and seismic data, *Ann. di Geofis.*, *40*, 587–6190, doi:10.1111/j.1365-2486.2011.02460.x.

Barnhoorn, A., M. Bystricky, K. Kunze, L. Burlini, and J.-P. Burg (2005), Strain localisation in bimineralic rocks: Experimental deformation of synthetic calcite-anhydrite aggregates, *Earth Planet. Sci. Lett.*, *240*(3–4), 748–763, doi:10.1016/j.epsl.2005.09.014.

Bilham, R., et al. (2016), Surface creep on the North Anatolian Fault at Ismetpasa, Turkey, 1944–2016, *J. Geophys. Res. Solid Earth*, *121*, 7409–7431, doi:10.1002/2016JB013394.

Bullock, R. J., N. de Paola, and R. E. Holdsworth (2015), An experiemntal investigation into the role of phyllosilicates content on earthquake propagation during seismic slip in carbonate faults, *J. Geophys. Res. Solid Earth*, *120*, 3187–3207, doi:10.1002/2015JB011914.

Beroza, G. C., and S. Ide (2011), Slow earthquakes and nonvolcanic tremor, *Annu. Rev. Earth Planet. Sci.*, *39*(1), 271–296, doi:10.1146/annurev-earth-040809-152531.

Bos, B., and C. J. Spiers (2000), Effect of phyllosilicates on fluid-assisted healing of gouge-bearing faults, *Earth Planet. Sci. Lett.*, *184*(1), 199–210, doi:10.1016/S0012-821X(00)00304-6.

Bos, B. and C. J. Spiers (2002), Frictional-viscous flow of phyllosilicate-bearing fault rock: Microphysical model and implications for crustal strength profiles, *J. Geophys. Res.*, *107*(B2), 2028, doi:10.1029/2001JB000301.

Bouchon, M., H. Karabulut, M. Aktar, S. Ozalaybey, J. Schmittbuhl, and M.-P. Bouin (2011), Extended nucleation of the 1999 M_w 7.6 Izmit earthquake, *Science*, *331*(6019), 877–880, doi:10.1126/science.1197341.

Bouchon, M., V. Durand, D. Marsan, H. Karabulut, and J. Schmittbuhl (2013), The long precursory phase of most large interplate earthquakes, *Nat. Geosci.*, *6*(4), 299–302, doi:10.1038/ngeo1770.

Boullier, A.-M., and Y. Gueguen (1975), SP-Mylonites: Origin of some mylonites by superplastic flow, *Contrib. to Mineral. Petrol.*, *50*(2), 93–104, doi:10.1007/BF00373329.

Brantut, N., M. Heap, P. Meredith, and P. Baud (2013), Time-dependent cracking and brittle creep in crustal rocks: A review, *J. Struct. Geol.*, *52*, 17–43, doi:10.1016/j.jsg.2013.03.007.

Çakir, Z., J.-B. de Chabalier, R. Armijo, B. Meyer, A. Barka, and G. Peltzer (2003), Coseismic and early post-seismic slip associated with the 1999 Izmit earthquake (Turkey), from SAR interferometry and tectonic field observations, *Geophys. J. Int.*, *155*(1), 93–110, doi:10.1046/j.1365-246X.2003.02001.x.

Çakir, Z., A. M. Akoglu, S. Belabbes, S. Ergintav, and M. Meghraoui (2005), Creeping along the Ismetpasa section of the North Anatolian fault (Western Turkey): Rate and extent from InSAR, *Earth Planet. Sci. Lett.*, *238*(1–2), 225–234, doi:10.1016/j.epsl.2005.06.044.

Çakir, Z., S. Ergintav, H. Ozener, U. Dogan, A. M. Akoglu, M. Meghraoui, and R. Reilinger (2012), Onset of aseismic creep on major strike-slip faults, *Geology*, *40*(12), 1115–1118, doi:10.1130/G33522.1.

Carpenter, B. M., C. Marone, and D. M. Saffer (2011), Weakness of the San Andreas Fault revealed by samples from the active fault zone, *Nat. Geosci.*, *4*(4), 251–254, doi:10.1038/ngeo1089.

Carpenter, B. M., M. J. Ikari, and C. Marone (2016), Laboratory observations of time-dependent frictional strengthening and stress relaxation in natural and synthetic fault gouges, *J. Geophys. Res. Solid Earth*, *121*, 1183–1201, doi:10.1002/2015JB012136.

Cetin, E., Z. Çakir, M. Meghraoui, S. Ergintav, and A. M. Akoglu (2014), Extent and distribution of aseismic slip on the Ismetpasa segment of the North Anatolian Fault (Turkey) from Persistent Scatterer InSAR, *Geochem. Geophys. Geosyst.*, *15*, 2883–2894, doi:10.1002/2014GC005307.

Chen, J., X. Yang, Q. Duan, T. Shimamoto, and C. J. Spiers (2013a), Importance of thermochemical pressurization in the dynamic weakening of the Longmenshan Fault during the 2008 Wenchuan earthquake: Inferences from experiments and modeling, *J. Geophys. Res. Solid Earth*, *118*, 4145–4169, doi:10.1002/jgrb.50260.

Chen, J., X. Yang, S. Ma, and C. J. Spiers (2013b), Mass removal and clay mineral dehydration/rehydration in carbonate-rich surface exposures of the 2008 Wenchuan Earthquake fault: Geochemical evidence and implications for fault zone evolution and coseismic slip, *J. Geophys. Res. Solid Earth*, *118*, 474–496, doi:10.1002/jgrb.50089.

Chester, F., J. Chester, D. Kirschner, S. Schulz, and J. Evans (2004), Structure of large-displacement, strike-slip fault zones in the brittle continental crust, *Rheol. Deform. Lithosph. Cont. Margins*, *1*, 223–260.

Collettini, C., A. Niemeijer, C. Viti, and C. Marone (2009), Fault zone fabric and fault weakness, *Nature*, *462*(7275), 907–910, doi:10.1038/nature08585.

Collettini, C., C. Viti, T. Tesei, and S. Mollo (2013), Thermal decomposition along natural carbonate faults during earthquakes, *Geology*, *41*, 927–930.

Deer, W. A., R. A. Howie, and J. Zussman (2013), *An Introduction to the Rock-Forming Minerals*, 488 pp., Mineralogical Society of Great Britain & Ireland ed, Twickenham, U. K.

de Michele, M., D. Raucoules, F. Rolandone, P. Briole, J. Salichon, A. Lemoine, and H. Aochi (2011), Spatiotemporal evolution of surface creep in the Parkfield region of the San Andreas Fault (1993–2004) from synthetic aperture radar, *Earth Planet. Sci. Lett.*, *308*(1–2), 141–150, doi:10.1016/j.epsl.2011.05.049.

den Hartog, S. A. M., A. R. Niemeijer, and C. J. Spiers (2013), Friction on subduction megathrust faults: Beyond the illite–muscovite transition, *Earth Planet. Scie. Lett.*, *373*, 8–19, doi:10.1016/j.epsl.2013.04.036.

Doebelin, N., and R. Kleeberg (2015), Profex: A graphical user interface for the Rietveld refinement program BGMN, *J. Appl. Crystallogr.*, *48*(5), 1573–1580, doi:10.1107/S1600576715014685.

Dor, O., C. Yildirim, T. K. Rockwell, Y. Ben-Zion, O. Emre, M. Sisk, and T. Y. Duman (2008), Geological and geomorphologic asymmetry across the rupture zones of the 1943 and 1944 earthquakes on the North Anatolian Fault: Possible signals for preferred earthquake propagation direction, *Geophys. J. Int.*, *173*(2), 483–504, doi:10.1111/j.1365-246X.2008.03709.x.

Ellero, A., G. Ottria, M. Marroni, L. Pandolfi, and M. C. Göncüoğlu (2015), Analysis of the North Anatolian Shear Zone in Central Pontides (northern Turkey): Insight for geometries and kinematics of deformation structures in a transpressional zone, *J. Struct. Geol.*, *72*, 124–141, doi:10.1016/j.jsg.2014.12.003.

Elliott, D. (1973), Diffusion flow laws in metamorphic rocks, *Geol. Soc. Am. Bull.*, *84*(8), 2645, doi:10.1130/0016-7606.

Emre, Ö., T. Y. Duman, S. Özalp, H. Elmacı, Ş. Olgun, and F. Şaroğlu (2013), Active fault map of Turkey with an explanatory text. 1:1,250,000 scale, General Directorate of Mineral Research and Exploration (MTA), Ankara-Turkey.

Fattahi, H., and F. Amelung (2016), InSAR observations of strain accumulation and fault creep along the Chaman Fault system, Pakistan and Afghanistan, *Geophys. Res. Lett.*, *43*, 8399–8406, doi:10.1002/2016GL07121.

Flerit, F., R. Armijo, G. C. P. King, B. Meyer, and A. Barka (2003), Slip partitioning in the Sea of Marmara pull-apart determined from GPS velocity vectors, *Geophys. J. Int.*, *154*(1), 1–7, doi:10.1046/j.1365-246X.2003.01899.x.

Fondriest, M., S. A. Smith, T. Candela, S. B. Nielsen, K. Mair, and G. Di Toro (2013), Mirror-like faults and power dissipation during earthquakes, *Geology*, *41*(11), 1175–1178.

Gasperini, L., A. Polonia, M. N. Çağatay, G. Bortoluzzi, and V. Ferrante (2011), Geological slip rates along the North Anatolian Fault in the Marmara region, *Tectonics*, *30*, TC6001, doi:10.1029/2011TC002906.

Gíslason, S. R., S. Arnórsson, and H. Ármannsson (1996), Chemical weathering of basalt in Southwest Iceland: Effects of runoff, age of rocks and vegetative/glacial cover, *Am. J. Sci.*, *296*(8), 837–907, doi:10.2475/ajs.296.8.837.

Göncüoglu, M. C. (2010), *Introduction to the Geology of Turkey: Geodynamic Evolution of the pre-Alpine and Alpine Terranes*, *Monogr. Ser.*, 66 pp., MTA, Ankara.

Grall, C., P. Henry, Y. Thomas, G. K. Westbrook, M. N. Çağatay, B. Marsset, H. Saritas, G. Çifçi, and L. Géli (2013), Slip rate estimation along the western segment of the Main Marmara Fault over the last 405–490 ka by correlating mass transport deposits, *Tectonics*, *32*, 1587–1601, doi:10.1002/2012TC003255.

Gratier, J.-P., J. Richard, F. Renard, S. Mittempergher, M.-L. Doan, G. Di Toro, J. Hadizadeh, and A.-M. Boullier (2011), Aseismic sliding of active faults by pressure solution creep: Evidence from the San Andreas Fault Observatory at Depth, *Geology*, *39*(12), 1131–1134, doi:10.1130/G32073.1.

Gratier, J.-P., E. Frery, P. Deschamps, A. Royne, F. Renard, D. K. Dysthe, N. Ellouz-Zimmerman, and B. Hamelin (2012), How travertine veins grow from top to bottom and lift the rocks above them: The effect of crystallization force, *Geology*, *40*(11), 1015–1018, doi:10.1130/G33286.1.

Gratier, J.-P., D. K. Dysthe, and F. Renard (2013a), The role of pressure solution creep in the ductility of the Earth's upper crust, *Advance in Geophysics*, *54*, 47–171.

Gratier, J.-P., F. Thouvenot, L. Jenatton, A. Tourette, M.-L. Doan, and F. Renard (2013b), Geological control of the partitioning between seismic and aseismic sliding behaviours in active faults: Evidence from the Western Alps, France, *Tectonophysics*, *600*, 226–242, doi:10.1016/j.tecto.2013.02.013.

Gratier, J.-P., C. Noiriel, and F. Renard (2015), Experimental evidence for rock layering development by pressure solution, *Geology*, *43*(10), 871–874, doi:10.1130/G36713.1.

Gudbrandsson, S., D. Wolff-Boenisch, S. R. Gislason, and E. H. Oelkers (2014), Experimental determination of plagioclase dissolution rates as a function of its composition and pH at 22°C, *Geochim. Cosmochim. Acta*, *139*, 154–172, doi:10.1016/j.gca.2014.04.028.

Hadizadeh, J., S. Mittempergher, J.-P. Gratier, F. Renard, G. Di Toro, J. Richard, and H. A. Babaie (2012), A microstructural study of fault rocks from the SAFOD: Implications for the deformation mechanisms and strength of the creeping segment of the San Andreas Fault, *J. Struct. Geol.*, *42*, 246–260, doi:10.1016/j.jsg.2012.04.011.

Hearn, E. H., S. McClusky, S. Ergintav, and R. E. Reilinger (2009), Izmit earthquake postseismic deformation and dynamics of the North Anatolian Fault Zone, *J. Geophys. Res.*, *114*, B08405, doi:10.1029/2008JB006026.

Herece, E. I., and E. Akay (2003), *Atlas of North Anatolian Fault*, General Directorate of Mineral Research and Exploration (MTA), 14 pp., Ankara-Turkey.

Holdsworth, R. E., E. W. E. van Diggelen, C. J. Spiers, J. H. P. de Bresser, R. J. Walker, and L. Bowen (2011), Fault rocks from the SAFOD core samples: Implications for weakening at shallow depths along the San Andreas Fault, California, *J. Struct. Geol.*, *33*(2), 132–144, doi:10.1016/j.jsg.2010.11.010.

Hubert-Ferrari, A. (2002), Morphology, displacement, and slip rates along the North Anatolian Fault, Turkey, *J. Geophys. Res.*, *107*(B10), 2235, doi:10.1029/2001JB000393.

Hussain, E., T. J. Wright, R. J. Walters, D. Bekaert, A. Hooper, and G. A. Houseman (2016a), Geodetic observations of postseismic creep in the decade after the 1999 Izmit earthquake, Turkey: Implications for a shallow slip deficit, *J. Geophys. Res. Solid Earth*, *121*, 2980–3001, doi:10.1002/2015JB012737.

Hussain, E., A. Hooper, T. J. Wright, R. J. Walters, and D. P. S. Bekaert (2016b), Interseismic strain accumulation across the central North Anatolian Fault from iteratively unwrapped InSAR measurements, *J. Geophys. Res. Solid Earth*, *121*, 9000–9019, doi:10.1002/2016JB013108.

Ildefonse, J., and V. Gabis (1976), Experimental study of silica diffusion during metasomatic reactions in the presence of water at 550 C and 1000 bars, *Geochim. Cosmochim. Acta*, *40*(3), 292–303, doi:10.1016/0016-7037(76)90206-4.

Imber, J., R. E. Holdsworth, C. A. Butler, and R. A. Strachan (2001), A reppraisal of the Sibson-Scholz fault model: The nature of the frictional to viscous (brittle-ductile) transition along a long-lived crustal-scale fault, Outer Hebrides, Scotland, *Tectonics*, *20*, 601–624, doi:10.1029/2000TC001250.

Isaacs, A. J., J. P. Evans, S.-R. Song, and P. T. Kolesar (2007), Structural, mineralogical, and geochemical characterization of the Chelungpu thrust fault, Taiwan, *Terr. Atmos. Ocean. Sci.*, *18*(2), 183–221.

Janssen, C., G. W. Michel, M. Bau, V. Lüders, and K. Mühle (1997), The North Anatolian Fault Zone and the role of fluids in seismogenic deformation, *J. Geol.*, *105*(3), 387–404, doi:10.1086/515934.

Jefferies, S. P., R. E. Holdsworth, C. A. J. Wibberley, T. Shimamoto, C. J. Spiers, A. R. Niemeijer, and G. E. Lloyd (2006a), The nature and importance of phyllonite development in crustal-scale fault cores: An example from the Median Tectonic Line, Japan, *Journal of Structural Geology*, *28*, 220–235.

Jefferies, S. P., R. E. Holdsworth, T. Shimamoto, H. Takagi, G. E. Lloyd, and C. J. Spiers (2006b), Origin and mechanical significance of foliated cataclastic rocks in the cores of crustal-scale faults: Examples from the Median Tectonic Line, Japan, *J. Geophys. Res.*, *111*, B12303, doi:10.1029/2005JB004205.

Jolivet, R., C. Lasserre, M.-P. Doin, S. Guillaso, G. Peltzer, R. Dailu, J. Sun, Z.-K. Shen, and X. Xu (2012), Shallow creep on the Haiyuan fault (Gansu, China) revealed by SAR interferometry, *J. Geophys. Res.*, *117*, B06401, doi:10.1029/2011JB008732.

Jolivet, R., C. Lasserre, M.-P. Doin, G. Peltzer, J.-P. Avouac, J. Sun, and R. Dailu (2013), Spatio-temporal evolution of aseismic slip along the Haiyuan fault, China: Implications for fault frictional properties, *Earth Planet. Sci. Lett.*, *377-378*, 23–33, doi:10.1016/j.epsl.2013.07.020.

Jolivet, R., T. Candela, C. Lasserre, F. Renard, Y. Klinger, and M.-P. Doin (2015), The burst-like behavior of aseismic slip on a rough fault: The creeping section of the Haiyuan Fault, China, *Bull. Seismol. Soc. Am.*, *105*(1), 480–488, doi:10.1785/0120140237.

Jouanne, F., F. A. Audemard, C. Beck, A. Van Welden, R. Ollarves, and C. Reinoza (2011), Present-day deformation along the El Pilar Fault in eastern Venezuela: Evidence of creep along a major transform boundary, *J. Geodyn.*, *51*(5), 398–410, doi:10.1016/j.jog.2010.11.003.

Kaneko, Y., Y. Fialko, D. T. Sandwell, X. Tong, and M. Furuya (2013), Interseismic deformation and creep along the central section of the North Anatolian Fault (Turkey): InSAR observations and implications for rate-and-state friction properties, *J. Geophys. Res. Solid Earth*, *118*, 316–331, doi:10.1029/2012JB009661.

Kondo, H., Y. Awata, O. Emre, A. Dogan, S. Ozalp, F. Tokay, C. Ildirim, T. Yoshioka, and K. Okuumura (2005), Slip distribution, fault geometry and fault segmentation of the 1944 Bolu-Gerede earthquake rupture, North Anatolian Fault, Turkey, *Bull. Seism. Soc. Am.*, *95*(4), 1234–1249.

Kondo, H., V. Özaksoy, and C. Yıldirim (2010), Slip history of the 1944 Bolu-Gerede earthquake rupture along the North Anatolian fault system: Implications for recurrence behavior of multisegment earthquakes, *J. Geophys. Res.*, *115*, B04316, doi:10.1029/2009JB006413.

Kozaci, Ö., J. F. Dolan, R. Finkel, and R. Hartleb (2007), Late Holocene slip rate for the North Anatolian fault, Turkey, from cosmogenic 36Cl geochronology: Implications for the constancy of fault loading and strain release rates, *Geology*, *35*(10), 867, doi:10.1130/G23187A.1.

Kozacı, Ö., J. F. Dolan, and R. C. Finkel (2009), A late Holocene slip rate for the central North Anatolian fault, at Tahtaköprü, Turkey, from cosmogenic ^{10}Be geochronology: Implications for fault loading and strain release rates, *J. Geophys. Res.*, *114*, B01405, doi:10.1029/2008JB005760.

Lanari, P., O. Vidal, V. De Andrade, B. Dubacq, E. Lewin, E. G. Grosch, and S. Schwartz (2014), Computers & Geosciences XMapTools: A MATLAB©-based program for electron microprobe X-ray image processing and geothermobarometry, *Comput. Geosci.*, *62*, 227–240, doi:10.1016/j.cageo.2013.08.010.

Le Pichon, X. (2003), The North Anatolian Fault in the Sea of Marmara, *J. Geophys. Res.*, *108*(B4), 2179, doi:10.1029/2002JB001862.

Lockner, D. A., C. Morrow, D. Moore, and S. Hickman (2011), Low strength of deep San Andreas fault gouge from SAFOD core, *Nature*, *472*(7341), 82–85, doi:10.1038/nature09927.

Marone, C. (1998), Laboratory-derived friction laws and their application to seismic faulting, *Annu. Rev. Earth Planet. Sci.*, *26*(1), 643–696, doi:10.1146/annurev.earth.26.1.643.

McClusky, S., et al. (2000), Global Positioning System constraints on plate kinematics and dynamics in the eastern Mediterranean and Caucasus, *J. Geophys. Res.*, *105*(B3), 5695–5719, doi:10.1029/1999JB900351.

Meade, B. J., B. H. Hager, S. C. McClusky, R. E. Reilinger, S. Ergintav, O. Lenk, A. Barka, and H. Özener (2002), Estimates of seismic potential in the Marmara Sea region from block models of secular deformation constrained by Global Positioning System measurements, *Bull. Seismol. Soc. Am.*, *92*(1), 208–215, doi:10.1785/0120000837.

Meghraoui, M., M. E. Aksoy, H. S. Akyüz, M. Ferry, A. Dikbaş, and E. Altunel (2012), Paleoseismology of the North Anatolian Fault at Güzelköy (Ganos segment, Turkey): Size and recurrence time of earthquake ruptures west of the Sea of Marmara, *Geochem., Geophys. Geosyst.*, *13*, Q04005, doi:10.1029/2011GC003960.

Mittempergher, S., G. Di Toro, J.-P. Gratier, J. Hadizadeh, S. A. F. Smith, and R. Spiess (2011), Evidence of transient increases of fluid pressure in SAFOD phase III cores, *Geophys. Res. Lett.*, *38*, L03301, doi:10.1029/2010GL046129.

Montes-Hernandez, G., N. Findling, and F. Renard (2016), Dissolution-precipitation reactions controlling fast formation of dolomite under hydrothermal conditions, *Appl. Geochem.*, *73*, 169–177, doi:10.1016/j.apgeochem.2016.08.011.

Moore, D. E., and M. J. Rymer (2007), Talc-bearing serpentinite and the creeping section of the San Andreas fault, *Nature*, *448*(7155), 795–797, doi:10.1038/nature06064.

Moore, D. E., D. A. Lockner, S. Ma, R. Summers, and J. D. Byerlee (1997), Strengths of serpentinite gouges at elevated temperatures, *J. Geophys. Res.*, *102*(B7), 14,787–14,801, doi:10.1029/97JB00995.

Noiriel, C., F. Renard, M.-L. Doan, and J.-P. Gratier (2010), Intense fracturing and fracture sealing induced by mineral growth in porous rocks, *Chem. Geol.*, *269*(3–4), 197–209, doi:10.1016/j.chemgeo.2009.09.018.

Ozakin, Y., Y. BenZion, M. Aktar, H. Karabulut, and Z. Peng (2012), Velocity contrast across the 1944 rupture zone of the North Anatolian fault east of Ismetpasa from analysis of teleseismic arrivals, *Geophys. Res. Lett.*, *39*, L08307, doi:10.1029/2012GL051426.

Peng, Z., and J. Gomberg (2010), An integrated perspective of the continuum between earthquakes and slow-slip phenomena, *Nat. Geosci.*, *3*(9), 599–607, doi:10.1038/ngeo940.

Perfettini, H., and J.-P. Avouac (2004), Postseismic relaxation driven by brittle creep: A possible mechanism to reconcile geodetic measurements and the decay rate of aftershocks, application to the Chi-Chi earthquake, Taiwan, *J. Geophys. Res.*, *109*, B02304, doi:10.1029/2003JB002488.

Pousse Beltram, L., E. Pathier, F. Jouhanne, R. Vassallo, C. Reinoza, F. Audemard, M.-P. Doin, and M. Volat (2016), Spatial and temporal variations in creep rate along the El Pilar fault at the Caribbean-South American plate boundary (Venezuela), from InSAR, *J. Geophys. Res., Solid Earth*, *121*, 8276–8296, doi:10.1002/2016JB013121.

Ramsay, J. G. (1967), *Folding and Fracturing of Rocks*, 588 pp., McGraw-Hill, New York.

Reilinger, R., et al. (2006), GPS constraints on continental deformation in the Africa-Arabia-Eurasia continental collision zone and implications for the dynamics of plate interactions, *J. Geophys. Res.*, *111*, B05411, doi:10.1029/2005JB004051.

Reilinger, R., S. McClusky, D. Paradissis, S. Ergintav, and P. Vernant (2010), Geodetic constraints on the tectonic evolution of the Aegean region and strain accumulation along the Hellenic subduction zone, *Tectonophysics*, *488*(1–4), 22–30, doi:10.1016/j.tecto.2009.05.027.

Renard, F., D. K. Dysthe, J. Feder, K. Bjørlykke, and B. Jamtveit (2001), Enhanced pressure solution creep rates induced by clay particles: Experimental evidence in salt aggregates, *Geophys. Res. Lett.*, *28*(7), 1295–1298, doi:10.1029/2000GL012394.

Richard, J., J.-P. Gratier, M.-L. Doan, A.-M. Boullier, and F. Renard (2014), Rock and mineral transformations in a fault zone leading to permanent creep: Interactions between brittle and viscous mechanisms in the San Andreas Fault, *J. Geophys. Res. Solid Earth*, *119*, 8132–8153, doi:10.1002/2014JB011489.

Rousset, B., R. Jolivet, M. Simons, C. Lasserre, B. Riel, P. Milillo, Z. Çakir, and F. Renard (2016), An aseismic slip transient on the North Anatolian Fault, *Geophys. Res. Lett.*, *43*, 3254–3262, doi:10.1002/2016GL068250.

Rowe, C. D., A. Fagereng, J. A. Miller, and B. Mapani (2012), Signature of coseismic decarbonation in dolomitic fault rocks of the Naukluft Thrust, Namibia, *Earth and Planet. Sci. Lett.*, *333–334*, 200–210.

Rutter, E. H. (1976), The kinetics of rock deformation by pressure solution, *Philos. Trans. R. Soc. London, Ser. A*, *283*(1312), 203–219, doi:10.1098/rsta.1976.0079.

Samuelson, J., and C. J. Spiers (2012), Fault friction and slip stability not affected by CO_2 storage: Evidence from short-term laboratory experiments on North Sea reservoir sandstones and caprocks, *Int. J. Greenh. Gas Control*, *11*(SUPPL), 78–90, doi:10.1016/j.ijggc.2012.09.018.

Scholz, C. H. (2006), The strength of the San Andreas Fault: A critical analysis, in *Earthquakes: Radiated Energy and the Physics of Faulting*, *Geophys. Monogr.*, vol. 170, edited by R. Abercrombie et al., pp. 301–311, AGU, Washington, D. C.

Şengör, A. M. C., N. Görür, and F. Şaroğiu (1985), Strike-slip faulting and related basin formation in zones of tectonic escape: Turkey as a case study, in *Strike-Slip Deformation, Basin Formation, and Sedimentation*, *Soc. Sediment. Geol.*, pp. 227–264, SEPM, Tulsa, Okla.

Şengör, A. M. C., O. Tüysüz, C. İmren, M. Sakınç, H. Eyidoğan, N. Görür, X. Le Pichon, and C. Rangin (2005), The North Anatolian Fault: A new look, *Annu. Rev. Earth Planet. Sci.*, *33*(1), 37–112, doi:10.1146/annurev.earth.32.101802.120415.

Sibson, R. H. (1990), Faulting and fluid flow, in *Fluids in Tectonic Regimes of the Continental Crust: Short Courses Handbook*, edited by B. E. Nesbitt, pp. 93–132, Mineralogical Association of Canada, Québec City, Canada.

Sone, H., T. Shimamoto, and D. E. Moore (2012), Frictional properties of saponite-rich gouge from a serpentinite-bearing fault zone along the Gokasho-Arashima Tectonic Line, central Japan, *J. Struct. Geol.*, *38*, 172–182, doi:10.1016/j.jsg.2011.09.007.

Stein, R. S., A. Barka, and J. H. Dieterich (1997), Progressive failure on the North Anatolian fault since 1939 by earthquake stress triggering, *Geophys. J. Int.*, *128*, 594–604, doi:10.1111/j.1365-246X.1997.tb05321.x.

Stewart, M. A., R. E. Holdsworth, and R. A. Strachan (2000), Deformation processes and weakening mechanisms within the frictional-viscous transition zone of major crustal faults: Insights from the Great Glen Fault zone, Scotland, *J. Struct. Geol.*, *22*, 543–560.

Straub, C., H.-G. Kahle, and C. Schindler (1997), GPS and geologic estimates of the tectonic activity in the Marmara Sea region, NW Anatolia, *J. Geophys. Res.*, *102*(B12), 27,587–27,601, doi:10.1029/97JB02563.

Tanaka, H., K. Fujimoto, T. Ohtani, and H. Ito (2001), Structural and chemical characterization of shear zones in the freshly activated Nojima fault, Awaji Island, southwest Japan, *J. Geophys. Res.*, *106*(B5), 8789–8810, doi:10.1029/2000JB900444.

Temiz, U., Y. E. Gökten, and J. Eikenberg (2013), Strike-slip deformation and U/Th dating of travertine deposition: Examples from North Anatolian Fault Zone, Bolu and Yeniçağ Basins, Turkey, *Quat. Int.*, *312*, 132–140, doi:10.1016/j.quaint.2013.08.034.

Tenthorey, E., C. H. Scholz, E. Aharonov, and A. Léger (1998), Precipitation sealing and diagenesis: 1. Experimental results, *J. Geophys. Res.*, *103*(B10), 23,951–23,967, doi:10.1029/98JB02229.

Thomas, M. Y., J.-P. Avouac, J.-P. Gratier, and J.-C. Lee (2014a), Lithological control on the deformation mechanism and the mode of fault slip on the Longitudinal Valley Fault, Taiwan, *Tectonophysics*, *632*, 48–63.

Thomas, M. Y., J.-P. Avouac, J. Champenois, J.-C. Lee, and L. C. Kuo (2014b), Spatiotemporal evolution of seismic and aseismic slip on the Longitudinal Valley Fault, Taiwan, *J. Geophys. Res. Solid Earth*, *119*, 5114–5139, doi:10.1002/2013JB010603.

Titus, S. J., C. DeMets, and B. Tikoff (2006), Thirty-five-year creep rates for the creeping segment of the San Andreas Fault and the effects of the 2004 Parkfield earthquake: Constraints from alignment arrays, continuous Global Positioning System, and creepmeters, *Bull. Seismol. Soc. Am.*, *96*(4B), 250–268, doi:10.1785/0120050811.

van Noort, R., H. J. M. Visser, and C. J. Spiers (2008), Influence of grain boundary structure on dissolution controlled pressure solution and retarding effects of grain boundary healing, *J. Geophys. Res.*, *113*, B03201, doi:10.1029/2007JB005223.

Verbene, B. A., O. Plumper, D. A. Matthijs de Winter, and C. J. Spiers (2014), Superplastic nanofibrous slip zones control seismogenic fault friction, *Science*, *346*(6213), 1342–1344.

Wheeler, J. (2014), Dramatic effects of stress on metamorphic reactions, *Geology*, *42*(8), 647–650, doi:10.1130/G35718.1.

Wibberley, C. A. J., and T. Shimamoto (2003), Internal structure and permeability of major strike-slip fault zones: The Median Tectonic Line in Mie Prefecture, Southwest Japan, *J. Struct. Geol.*, *25*, 59–78.

Wilson, M., A. Tankut, and N. Guleç (1997), Tertiary volcanism of the Galatia province, north-west Central Anatolia, Turkey, *Lithos*, *42*(1–2), 105–121, doi:10.1016/S0024-4937(97)00039-X.

Wilson, M. J. (2004), Weathering of the primary rock-forming minerals: Processes, products and rates, *Clay Miner.*, *39*(3), 233–266, doi:10.1180/0009855043930133.

Yildirim, C., T. F. Schildgen, H. Echtler, D. Melnick, and M. R. Strecker (2011), Late Neogene and active orogenic uplift in the Central Pontides associated with the North Anatolian Fault: Implication for the northern margin of the Central Anatolian Plateau, Turquey, *Tectonics*, *30*, TC5005, doi:10.1029/2010TC002756.

Zubtsov, S., F. Renard, J.-P. Gratier, R. Guiguet, D. K. Dysthe, and V. Traskine (2004), Experimental pressure solution compaction of synthetic halite/calcite aggregates, *Tectonophysics*, *385*(1–4), 45–57, doi:10.1016/j.tecto.2004.04.016.

2.6 Supporting information S1

Journal of Geophysical Research

Supporting Information for

The implications of fault zone transformation on aseismic creep: example of the North Anatolian Fault, Turkey

Maor Kaduri[1], Jean-Pierre Gratier[1], François Renard[1,2], Ziyadin Çakir[3], and Cécile Lasserre[1]

[1]University Grenoble Alpes & CNRS, ISTerre, CS 40700, 38058 Grenoble cedex 9, France

[2]Department of Geosciences, Physics of Geological Processes, University of Oslo, box 1048, 0316 Blindern, Oslo, Norway

[3]Istanbul Technical University, Department of Geology, Istanbul, Turkey

Contents of this file

Text S1
Tables S1 to S4

Introduction

The present Supplementary Material contains additional information on the analytical methods used in the article, the description of the statistical method used to produce the plot of Figure 2h, and the tables of the locations of the outcrops shown on Fig. 1 (Table S1) and mineralogical compositions of fault zone samples shown in Figures 4e, 7d, 8e (Tables S2 to S4).

Text S1: Complements to the analytical methods

Powder X-ray diffraction analyses

In order to quantify the mineral content of each sample, X-ray diffraction (XRD) analyses were conducted. The samples were prepared in several steps. Firstly, a quantity of 1-5 grams of rock sample was crushed and homogenized. Secondly, the fraction <2mm was ground using a McCrone micronizing mill, and the resulting slurry oven-dried to reprecipitate soluble salts before being prepared as a randomly oriented mount. The clay mineralogy was determined on the average grain size of the ~1µm fraction. Oriented mounts were prepared by drying the resulting suspension on glass slides. The XRD patterns of powders were then recorded using either a SIEMENS Bruker D5000 or a D8 Advance X-Ray diffractometer, equipped with a SolX Si(Li) solid state detector from Baltic Scientific Instruments using Cu Kα1+2 radiation (λ =1.5406Å). The measurement conditions were: goniometer vertical θ-θ; generator power 40kV, 40mA; range 5°-90° with

0.026° step size; step time of 8 seconds for D8 and 16 seconds for D5000; divergence slit 0.6 mm; reception slit 0.2 mm; Soller slit 2.5°; detector energy window 8.05 keV, <350eV. Finally, the mineral semi-quantitative analysis was performed by the Rietveld method, using the software Profex 3.6.0, which is based on the B.G.M.N algorithm [Doebelin and Kleeberg, 2015].

X-ray fluorescence imaging

At the millimeter to centimeter scale, X-ray fluorescence (XRF) imaging and microanalyses were performed on thin sections using a micro-imaging X-ray fluorescence spectrometer (Eagle III), with spatial resolution of 30 μm per pixel. This technique provides maps of the distribution of chemical elements (oxide content). However, an absolute quantification of the element concentrations cannot be performed easily and this qualitative technique has to be confirmed by EPMA analyses. These maps were used to characterize microstructures because they can be applied to large samples (up to decimeter in size) in a shorter time and at a cheaper cost than EPMA, and the procedure could therefore be performed on a larger number of samples.

Electron microprobe chemical analyses

The chemical measurements were performed using an electron probe micro-analyzer (EPMA) JEOL JXA-8230, and the conductive coating on the thin section was made using a high-vacuum carbon evaporator (Quorum technologies) with Q150TE turbo-pump. Wavelength-Dispersive X-Ray Spectroscopy (WDS) was used to acquire both precise chemical analyses of selected phases and maps of elements. The raw data was then corrected using standard minerals. WDS was used for semi-quantitative chemical analysis to determine the main phase either by element or by oxide. WDS was then used to scan maps of elements in selected areas with the following operating conditions: acceleration voltage 15 keV, specimen current 100 nA, dwell time 11.2 ms and spatial resolution in the range 1-2μm pixel size.

Scanning electron microscopy

Electron microscopy images were acquired on a Hitachi S-2500 and on a JEOL JXA-8230 scanning electron microscope (SEM). Energy-dispersive spectroscopy (EDS) and backscattered electron (BSE) images were used. Unless otherwise stated, the semi-quantitative chemical analyses of a variety of minerals were normally made using EDS under 16kV acceleration voltage and 3μm beam diameter. In this framework, in order to study the meso-structure of shear zones, several mosaics of BSE-SEM images were created using Adobe Photoshop.

All these techniques were performed on the analytical platforms at the ISTerre laboratory at the University Grenoble Alpes and in the CMTC at Grenoble-INP.

Calculation of the probability function in Figure 2h

The probability P_L to find fracture spacing with size L (bin size) in the interval (L-ΔL, L+ΔL) is given by

$P_L = P(L-\Delta L <= L <= L+\Delta L) = N_L/N_L^{Tot}$

where N_L is the number of fracture spacing with size L. The total number of fracture spacing is given by $N_L^{Tot} = \sum_{L_{\min}}^{L_{\max}} N_L$; where the sum of all probabilities is by definition normalized to unity, such that $\sum_{L_{\min}}^{L_{\max}} P_L = 1$.

Table S1. Outcrops along the North Anatolian Fault that were investigated in the present study. Locations are also given on Fig. 1.

	Site name - Outcrop location (Latitude / Longitude)	**Lithology of host rock**
Locked sections	Mekece(Me) 40°27'10.00"N/ 30° 3'4.00"E	Limestone
	Ciciler (Ci) 40°26'16.68"N/ 30° 3'16.50"E	Limestone
	Taşkesti-2 (Ta2) 40°34'5.00"N/ 31° 0'4.00"E	Limestone
	Taşkesti-1 (Ta1) 40°34'54.00"N/ 31° 1'60.00"E	Limestone
	Bolu (Bo) 40°41'8.91"N/ 31°34'3.01"E	Limestone
	Demirciler (De) 40°41'44.68"N/ 31°41'27.00"E	Limestone
Creeping section	Gerede (Ge) 40°47'3.00"N/ 32° 6'30.00"E	Volcanic rock
	Soplan Mha 40°56'41.00"N/ 32°32'54.00"E	Volcanic rock
	Ismetpasa 40°51'55.00"N/ 32°35'41.00"E	Volcanic rock
	Hamamli-1 (Ha1) 40°52'12.19"N/ 32°39'8.78"E	Serpentine
	Hamamli-2 (Ha2) 40°52'22.80"N/ 32°39'55.34"E	Volcanic rock
	Cayli (Ca) 32°54'14.97"E, 40°54'48.63"N	No outcrop
	Yazioren (Ya) 40°56'1.59"N/ 33° 6'11.09"E	Volcanic and sediment mélange
	Sarialan (Sa) 40°57'58.51"N/ 33°21'37.55"E	Volcanic rock
	Aliç 40°58'51.56"N/ 33°30'4.48"E	Volcanic rock
	Mülayim (Mu) 41° 3'5.28"N/ 33°48'17.61"E	Metabasite/ophiolitic mélange

Table S2. Table of composition for Fig. 4e.

sample	Magnesite	Dolomite	Calcite	Quartz	Siderite	Smectite	Saponite	Mica	Muscovite	Hematite	Goethite	Talc	Kaolinite	Chlorite	Lizardite
G06	22	69		8					2						
G10	13.47	81.46		0.516		2.53				2.02					
G01	39.99	36.99		16.28		6.92									
G14	21	45.2		25.32		6.38				2.09					
G15	31.99	54.62		4.85		7.6				0.93					
G02	26.2	27.4		36.99		9.7									
G04	38			47		16									
G07	9.08	17.53		58.3		5.8				4.71		2.75	1.83		
G16	33	50					12			3					2
G1T	28	53				19									
G12	33.22	46.87		0.308		15.66				1.88			2.06		
G3B	36			39		25									
G3A	24	1		42	7	26									
G09	7.18	64.72		0.474		16.53								11.1	
G08	19.63	51.69				20.81					0.75		4.24	2.88	
G11	24.4	17.12	1.34			39		1.48			10.08		6.53		
G3T	6	15					79								
G13	6.52	3.91				45.48		6.94			16.27		20.88		
G 2T	5	5					54			1	36				

Table S3. Table of composition for Fig. 7d.

XRD/ Minerals	**4**	**3**	**1**	**2**
Labradorite	45.7		14	
Albite	12.12		24	9
Plagioclase		3		
Magnesite	0.62	23		22
Dolomite		18		
Siderite	4.11			
Ankerite	3.21			3
Quartz	1.19	9	11	15
Muscovite		6		9
Smectite	33	17	51	36
Kaolinite		24		
Chlorite				6

Table S4. Table of mineral composition for Fig. 8b.

XRD/ Minerals	**Clast**	**Foliated gouge**	**Granular gouge**
Anorthite		43.05	18.4
Labradorite	42.86		
Calcite			3.75
Quartz	33.6	4.55	17.9
Smectite	23.53	52.41	53.8
Kaolinite			0.98
Muscovite			4.1
Hematite			1.02

Chapter 3

3. Quantifying the partition between seismic and aseismic deformation along creeping and locked sections of the North Anatolian Fault, Turkey

Manuscript to be submitted to Pure and Applied Geophysics.

Quantifying the partition between seismic and aseismic deformation along creeping and locked sections of the North Anatolian Fault, Turkey

Maor Kaduri[1], Jean-Pierre Gratier[1], Cécile Lasserre[2], Ziyadin Çakir[3], François Renard[1,4,*]

[1] Univ. Grenoble Alpes, Univ. Savoie Mont Blanc, CNRS, IRD, IFSTTAR, ISTerre, 38000 Grenoble, France

[2] Université de Lyon, UCBL, ENSL, CNRS, LGL-TPE, 69622 Villeurbanne, France

[3] Istanbul Technical University, Department of Geology, Istanbul, Turkey

[4] The Njord Center, PGP, Department of Geosciences, University of Oslo, box 1048, 0316 Blindern, Oslo, Norway

[*]Correspondence should be addressed to François Renard (francois.renard@geo.uio.no)

Abstract

Shallow aseismic creep is a key deformation component along plate boundaries because it contributes to the energy budget during the seismic cycle. Several major active continental faults show spatial alternation of creeping and locked sections. One of the greatest challenges in fault mechanics is to understand which parameters control the transition from seismic to aseismic deformation in fault zones, such as lithology or stress-driven transformations at all scales. The present study focuses on the evaluation of the aseismic part of the total displacement along the North Anatolian Fault in Turkey. Finite strain was measured using various methods on samples collected on six outcrops located along locked and creeping sections of the fault. X-ray fluorescence and electron microprobe analysis methods were used to map mineral composition of fault rocks and to calculate the relative volume changes associated with creep. The relationship between finite strain and volume change reflects the evolution of the creep mechanisms with geological time from solution cleavage to grain boundary sliding to mixed diffusive and friction-controlled processes. Finite strain modeling reveals two spatial scales of strain that correspond to the alternation of two types of shear zones, with cleavages either oblique or sub-parallel to the fault zone. Using geodetic and geological data to evaluate the width of these shear zones the aseismic part of the total 80km displacement is finally evaluated. This aseismic part depends on fault lithology and varies from 0.002% in the locked zones (limestone rocks, Taskesti) to 25±16% in the creeping zones (volcanic rocks, Ismetpasa).

3.1 Introduction

Aseismic creep has been extensively documented along several active faults worldwide (Chen and Bürgmann, 2017; Harris, 2017). Active fault creep processes develop either as transient (mostly post-seismic) sliding or as permanent sliding. Post-seismic creep rate can evolve through time with various patterns : with an exponential or a power law decay, down to zero or to a residual constant creep velocity (Çakir et al., 2005). In some cases, shallow creep can accommodate the whole tectonic loading as along the permanent creeping section of the San Andreas fault (Savage and Burford, 1973). In cases where shallow creep only partly releases the tectonic loading, as along the North Anatolian, the Hayward or the Longitudinal Valley faults in Turkey, California and Taiwan, respectively (Çakir et al., 2005, Graymer et al. 2005, Thomas et al., 2014), large earthquakes may still occur at depth and propagate toward the surface.

Consequently, these contrasting creep behavior patterns may have different implications for seismic hazard assessment. It is therefore crucial to understand the spatio-temporal characteristics of creep and its mechanisms. Rock types can partly control fault creep behavior. For example, observations have shown that surface creep rates along the North Anatolian Fault are almost null along fault sections that are rich in massive limestones, but become significant along sections that host various kinds of volcanic rocks that were softened by progressive deformation processes (Kaduri et al., 2017). However, other important characteristics of creep, such as creep deformation duration during a single seismic cycle and over several seismic cycles, as well as the aseismic part of the total displacement during geological fault history, remain to be determined more accurately.

To make progress in understanding creep mechanisms, the displacement associated with creep processes must be evaluated. On one hand, the total displacement over the lifetime of a fault accommodated by both creep and earthquakes can be evaluated by measuring the offset of a number of geological markers (Emre et al., 2013). On the other hand, the displacement associated with creep processes can be deduced only from geodetic or geological strain measurements, giving the short-term interseismic strain and the long-term finite strain, respectively.

However, surface geodetic measurements include both the irreversible (ductile creep) and reversible (elastic) parts of the deformation. The distinction between creep and tectonic loading is generally made through simple modeling by considering an elastic half-space surrounding a fault plane (Savage and Burford, 1973; Okada, 1985). In addition, geodetic measurements are representative of slip in the past few years to decades only. Extending geodetic displacement measurements to the long term (geological times of several millions years) must include an assumption on the variations of the displacement rate with time, which is almost impossible to estimate, especially in areas associating seismic and aseismic processes. Consequently, in order to evaluate only the irreversible part of the large finite strain associated with the creep processes, complementary detailed finite strain measurements in the gouge and damage zone rocks of fault zones are required.

The aim of the present study is to quantify the displacement related to aseismic irreversible creep processes in both creeping and apparently locked sections along the North Anatolian Fault in Turkey, by measuring the associated geological finite strain in the gouge and damage zone rocks **(Fig. 1)**. In order to calculate this displacement, two types of data are required: the finite strain values and the width of the associated shear deformation (Ramsay, 1980; Ramsay and Graham, 1970). However, the measurement and the interpretation of such data are rather complex because strain and fault width values evolve with time and along the fault strike during deformation, since the beginning of the formation of the fault to the present days. Strike-slip creeping faults accumulate strain in the upper crust by plastic and viscoelastic mechanisms involving both shear deformation and mass transfer, developing what is known as compaction or dilatant shear zones (Ramsay, 1980; Ramsay and Graham, 1970). In such zones, the mineral composition and rock fabric change due to mass transfer, fluid circulation, chemical alteration and metamorphism (Gratier et al., 2013, 2011). Moreover, clay gouge comprising low friction minerals such as montmorillonite and saponite also develop (Carpenter et al., 2016; Kaduri et al., 2017; Lockner et al., 2011; Samuelson and Spiers, 2012). In addition, fault growth is not linear with displacement. Power law relationships between maximum displacement and fault width are often reported (Pennacchioni, 2005; Scholz, 2002). At the outcrop scale, irreversible shear strain gradients generally decrease to zero away from the fault over distances of several centimeters to several kilometers, and sometimes over distances of up to 25 km (Mavko, 1981). The lateral evolution of such strain profiles is often non-linear (Pennacchioni, 2005). Shear zone width evolution in time and space thus depends on the deformation mechanisms that combine simple shear, pure shear and volume change and that determine the displacement behaviors (Fossen and Cavalcante, 2017; Bos and Spiers, 2002; van der Pluijm and Marshak, 2010). Such heterogeneous shear zones can be classified into three categories based on the evolution of their width: increasing, decreasing or constant in time (Hull, 1988). The shape of displacement profiles across faults depends on whether the deformation process is strain hardening (deformation diffuses into the host rock) or strain softening (deformation is localized in narrow zones) (Vitale and Mazzoli, 2008). In particular, strain-softening processes involving simple shear with volume loss are consistent with clay gouge formation (Kaduri et al., 2017).

Measuring and interpreting finite strain and the width of the associated creeping shear from geodetic and geological observations are challenging tasks, especially when deformation involves very high strain values. Despite considerable uncertainties associated with both types of observations, the data presented in this study of the North Anatolian fault can be used to characterize: (i) the spatial correlation between the creep-related strain measured by geodetic and geological methods, (ii) the control of rock lithology on aseismic creep mechanisms and temporal evolution, (iii) the aseismic part of the total displacement on the fault.

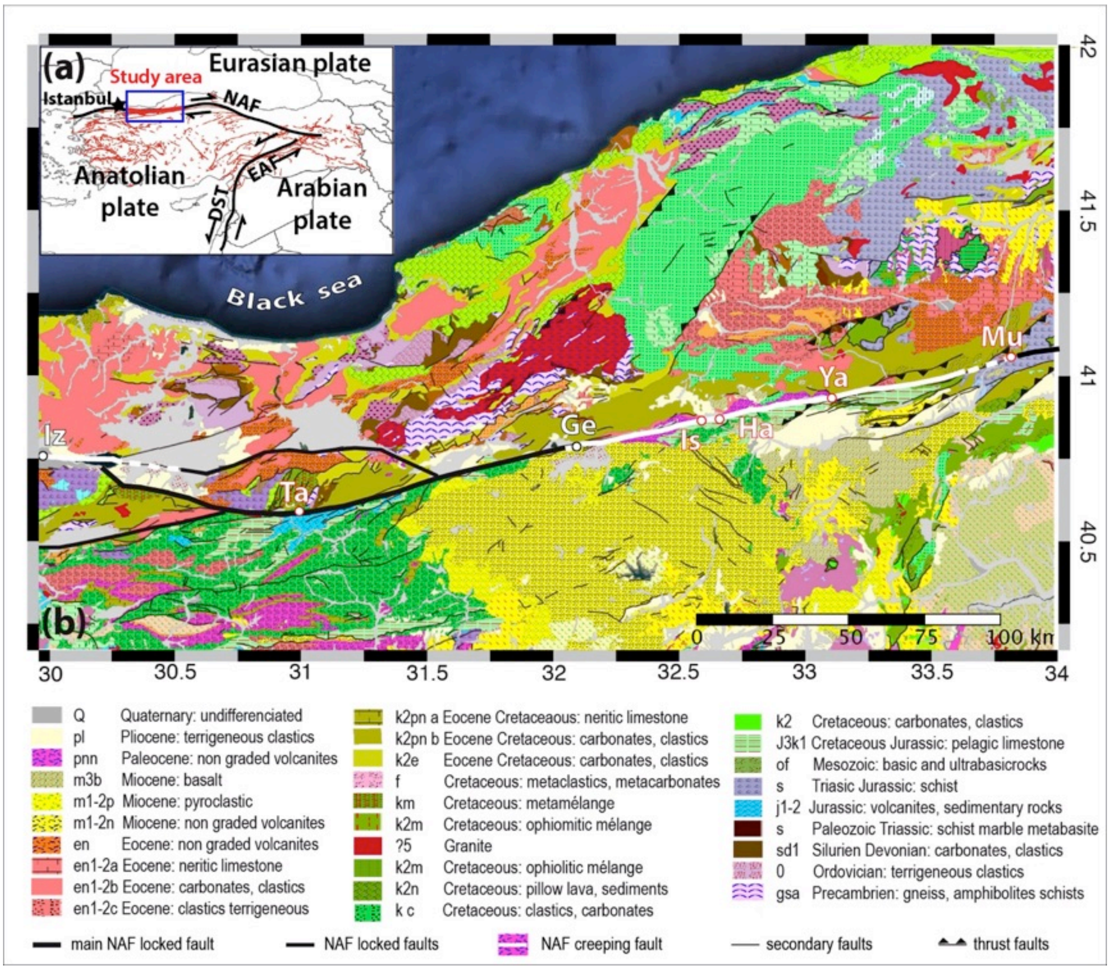

Figure 1. Structural and geological map of the study area along the North Anatolian Fault (NAF), modified from Kaduri et al. (2017). (a) Tectonic setting of study area, located east of Istanbul (blue rectangle with NAF in red (Emre et al., 2013). EAF: East Anatolian Fault, DST: Dead Sea Transform fault. (b) Geological map of the study area with names and outcrop locations indicated as red circles for the six studied outcrops: Iz=Izmit, Ta=Taskesti (40°34'54.00"N/ 31°1'60.00"E), Ge=Gerede (40°47'3.00"N/ 32°6'30.00"E), Is=Ismetpasa (40°51'55.00"N/ 32°35'41.00"E), Ha=Hamamli (40°52'12.19"N/ 32°39'8.78"E) Ya= Yazioren (40°56'1.59"N/ 33°6'11.09"E), Mu=Mülayim (41° 3'5.28"N/ 33°48'17.61"E). The presently creeping segments of Izmit (west) and Ismetpasa (east) are marked in white (Çakir et al., 2005; Cetin et al. 2014). The locked segments are black. The regional geological map is extracted from an interactive map of the Turkish geological survey (Akbas et al., 2016) available at http://yerbilimleri.mta.gov.tr/anasayfa.aspx. The legend gives the lithology of the formations that are cut by the studied North Anatolian Fault section.

3.2 Measuring creep-related deformation from fault zone outcrops: setting and approach

3.2.1 Seismotectonic setting

The North Anatolian Fault (NAF) in Turkey is a right-lateral strike-slip plate boundary. This major continental fault accommodates the relative motion between the

Anatolia plate, to the south, and the Eurasian plate, to the north. The NAF formed approximately 13 to 11 Ma ago in the east and slowly propagated westward (Şengör, et al. 2004). The long-term geological rate is 20±8 mm/yr (Şengör, et al. 2004), consistent with short-term geodetic rates, 24±2 mm/yr from GPS data (Reilinger et al., 2006) and 25±1.5 mm/yr from InSAR data (Cetin et al., 2014). The total cumulative displacement along the studied NAF segment (Fig. 1) since its initiation is of the order of 80 km (Janssen, et al., 1997; Armijo et al., 1999; Emre et al., 2013; Akbas et al., 2016). A sequence of large earthquakes propagated from east to west and ruptured over 1000 km of the fault during the 20th century (e.g. Emre et al., 2016), providing evidence of the potential of the fault to accumulate large seismic displacement. However, a striking feature of the NAF is the existence of two slip modes along the fault. Some sections are prone to large earthquakes (Stein et al., 1997) and remain locked in between earthquakes while others sections display aseismic creep that possibly initiated as post-seismic slip (Kaneko et al., 2013; Çakir et al., 2014; Cetin et al., 2014) and may behave as a succession of transient creep episodes (Bilham et al., 2016; Rousset et al., 2016). The relative contribution of seismic and aseismic displacement in the total 80 km displacement remains to be evaluated. This is the aim of this study.

At least two sections of the North Anatolian Fault inland have been identified in the recent years as aseismic creeping fault sections (Ismetpasa and Izmit sections, **Fig. 1)**. Based on an InSAR study of Envisat satellite data along descending orbits, it has been shown by Cetin et al. (2014) that the Ismetpasa creeping section runs from longitude 32.2° to 34.0°, with a maximum surface horizontal creep rate of ~20 mm/yr, located 30 km east of Ismetpasa, and a creeping depth of ~5 km. These results were recently revised from a new Envisat InSAR analysis including both descending and ascending data, which helped to obtain a better separation of the vertical and horizontal creep components. The Ismetpasa creeping section was found to be longer (running from 31.0° to 35.0°), with two peaks of maximum horizontal creep rate up to ~14 mm/yr, and creep extending down to 9 km depth (Hussain et al., 2016). A clear correlation between shallow creep rate and near-surface fault lithology has been demonstrated (Kaduri et al., 2017): the locked section west of the Ismetpasa creeping section is mostly composed of massive limestone and dolomite whereas the creeping section is composed of volcanic and ophiolite rocks including clay-rich gouges **(Fig. 1)**.

3.2.2 Fault sampling and strategy analysis

In order to calculate the aseismic part of the total displacement along both locked and creeping zones of the North Anatolian Fault, the finite strain and the creeping width for various lithologies were evaluated by investigating more than 30 outcrops, over a 400 km-long section between the city of Izmit to the west and the eastern end of the Ismetpasa creeping section to the east. Fault zone samples were collected and analyzed in detail from a dozen of well-preserved outcrops, along creeping and locked sections of the fault. Finally, six outcrops were selected for which abundant strain markers were available, one from the locked section and five from the creeping section **(Fig. 1)**. The focus was placed here on the evolution from initial rock to damaged rock and gouges, in order to characterize strain related to aseismic creep at different stages of fault evolution.

Strain was measured at various scales from thin sections to outcrop scales. Microstructural strain measurements were taken on hand samples, which were sawn and polished. Exposed surfaces were then prepared as thin sections for microscopy observations. All the samples were oriented with respect to the North. We developed image processing techniques based on MATLAB codes to calculate internal finite strain from particle distributions or deformation of geological objects (Ramsay, 1967) with two distinct approaches for samples along locked or creeping sections. Macrostructural strain measurements were derived from field studies in quarries that present outcrops more than 100 m wide, located within the NAF shear zone, of kilometric width. Measurements of the relations between fault and cleavage on thin sections and outcrops (Ramsay, 1980; Ramsay and Graham, 1970) allowed characterizing strain measurements at various scales from the thin section (0.01 mm to 10 cm) to the outcrop scales (10 cm to 1 km).

3.2.3 Strain measurement in shear zones accommodating aseismic creep

To simplify matters, both creeping and locked sections were considered to be ideal shear zones involving shear with volume change perpendicular to the fault zone (**Fig. 2a**) with:

$$\gamma = f\,(\lambda_1, \lambda_2, \Delta) \qquad (1)$$

where γ is the shear strain for a unit width of 1, λ_1 is the quadratic extension, λ_2 is the quadratic contraction and Δ is the volume (or surface area) change. The set of equations used to measure strain from the deformation of microstructural markers, such as cleavages or grains, and from local mass transfer are defined below.

The coordinate system was chosen so that the z-axis is horizontal and perpendicular to the shear zone, the x-axis is horizontal along the shear direction and the y-axis vertical, pointing at depth along the fault (**Fig. 2b**). Plane strain in 2D is assumed, thereby implying homogeneity along the **y**-axis (Ramsay, 1980; **Heilbronner** and **Barrett**, 2014; Fossen and Cavalcante, 2017).

The quadratic extension/contraction λ is defined in **Eq. 2** :

$$\sqrt{\lambda} = l_f / l_i \tag{2}$$

where l_f is the final length of a deformed object, and l_i its initial length. For simple shear in plane strain, a unit circle becomes distorted into an ellipse, which is defined by the lengths of the elongation axis and the shortening axis. The principal strain component can be described as a function of the shear strain (Ramsay, 1967), as defined in **Eq. 3** :

$$\lambda_{1,2} = \frac{\gamma^2 + 2 \pm \gamma\sqrt{\gamma^2 - 4}}{2} \tag{3}$$

where λ_1 is the quadratic extension, λ_2 is the quadratic contraction and with the shear strain $\gamma = \tan(\psi)$ for a unit width of 1. Then, by measuring λ_1 or λ_2 from microstructures the shear strain values are obtained from **Eq. 3**.

In addition, in plane strain, the product of the two principal strain values is related to the volumetric change as follows:

$$\sqrt{\lambda_1 \lambda_2} = 1 + \Delta \tag{4}$$

where, Δ is the volume (or surface area) change, which can also be written as $\Delta = (V_f - V_i)/V_i$, with V_i, V_f the initial and final volumes before and after deformation, respectively (Ramsay, 1967).

For simple shear followed by volume change the matrix of deformation transforms the undeformed vector (x, z) (initial state) to a new position after deformation (deformed state) (x', z'):

$$\begin{pmatrix} x' \\ z' \end{pmatrix} = \begin{pmatrix} 1 & \gamma_{s,\Delta} \\ 0 & 1 + \Delta \end{pmatrix} \cdot \begin{pmatrix} x \\ z \end{pmatrix} \tag{5}$$

where $\gamma_{s,\Delta}$ is the strain due to shear and dilation (Fossen and Tikoff, 1993), defined as:

$$\gamma_{s,\Delta} = \frac{\gamma\Delta}{\ln(1+\Delta)} \qquad (6)$$

and the principal strains are:

$$\lambda_{1,2} = \frac{1}{2}\left(1+\gamma^2+(1+\Delta)^2 \pm \sqrt{[1+\gamma^2+(1+\Delta)^2]^2-4(1+\Delta)^2}\right) \qquad (7)$$

where $\Delta = 0$ is a particular case of simple shear with **Eq.5** equal to **Eq.3** (as represented in **Fig. 2a)**.

The angle θ' of λ_1 measured from the shear direction (horizontal positive) (Ramsay, 1980) is given by:

$$\theta' = \frac{1}{2}\arctan\left(\frac{2\gamma(1+\Delta)}{1+\gamma^2-(1+\Delta)^2}\right) \qquad (8)$$

Both the aspect ratio between the principal strain axes $R(\gamma,\Delta) = \sqrt{\lambda_1/\lambda_2}$, and $\theta'(\gamma,\Delta)$ are nonlinear functions of γ and Δ (i.e. surfaces in a three-dimensional coordinate system). Such functions are known as $R-\theta'$ diagrams when plotted together (Fossen and Tikoff, 1993).

In a shear plane, passive line markers (e.g. cleavage or vein) originally making an angle α with the shear zone walls, are sheared to make a new angle α' (Ramsay, 1980) such that:

$$\cot(\alpha') = \frac{\cot(\alpha)+\gamma}{1+\Delta} \qquad (9)$$

Assuming that the cleavage is parallel to the quadratic extension λ_1 (Ramsay, 1967) θ' and α' have the same value. The total shear displacement $d_{\hat{a}}$ is then obtained by integration the shear strain along the z-axis (Ramsay, 1980), (**Fig. 2**):

$$d_{\hat{a}} = \int_0^w \gamma \cdot dz \qquad (10)$$

where, w is the width of the shear zone, and γ is the shear strain. This method of measuring the evolution of the angle between cleavage and shear zone is very efficient and allows evaluating very large shear strain values measured at scales from thin sections to outcrops.

3.2.4 Strain measurement along the locked section measured from stylolite and vein arrays

The strain contraction component can be calculated by two techniques. The first technique involves identifying veins shifted by stylolites (Gratier et al., 2013) and using **Eq. 11**:

$$\Delta l = l_{v2v}/\tan(\beta) \qquad (11)$$

where Δl is the thickness of the layer dissolved by the stylolite, l_{v2v} the distance between the vein walls, and β the angle between the direction of the vein and the stylolites peaks **(Fig. 2c)**. Then, the initial length of the vein is obtained by adding the shifted length to the final length of the shifted vein $l_i = l_f + \Delta l$, and the quadratic contraction can be calculated using **Eq. 2**.

The second technique involves using the maximum amplitude of the stylolite peaks and applying **Eq. 12**:

$$\sqrt{\lambda_2}_{stylolite}(\varphi) = \frac{L_{Tot}(\varphi)}{L_{Tot}(\varphi)+N_{Stylolite}(\varphi)\cdot\langle Amp_{max}(\varphi)\rangle} \tag{12}$$

where $\sqrt{\lambda_2}_{stylolite}$ is the quadratic contraction due to stylolite in direction φ, $N_{Stylolite}$ is the number of stylolite in direction φ, $\langle Amp_{max}\rangle$ is the average maximum peak height in direction φ, and L_{Tot} the total length of the sample in direction φ.

The extension component is measured perpendicular to the vein direction. The final length is defined from side to side and the initial length is the spacing between the veins. Finally, the contraction and extension components are combined and plotted in polar coordinates to define the strain ellipse.

3.2.5 Strain measurement along the creeping section

3.2.5.1 Strain measurements from boudinage and folding analysis on XRF chemical maps

Two-dimensional XRF chemical maps were acquired using a X-ray fluorescence spectrometer (Eagle III) (Kaduri et al., 2017). Strain markers were derived from these chemical maps, at representative sizes of several millimeters to centimeters. The strain values were extracted using either the angle or the initial and final lengths of markers as described below.

The extension component can be obtained from the measurement of boudinage microstructures. For example, the quadratic extension is calculated by i) measuring the initial length (l_i) by adding the length of each clast, and ii) calculating the final length (l_f) which is the length from the first to the last clast **(Fig. 2e)**.

The contraction component can be obtained from folded veins. In this case, the quadratic contractional strain can be estimated by measuring i) the initial length of the vein and ii) the length of an arc along a deformed object using **Eq. (13)**:

$$l_i = \sum_{i=1}^{n} ds_i = \int_0^{l_0} dx\sqrt{1+(dy/dx)^2} \tag{13}$$

where ds_i is the length of the section between two successive points and can be written as $ds_i = \sqrt{(x_i - x_{i-1})^2 + (y_i - y_{i-1})^2}$.

3.2.5.2 Strain measurements from grains geometry and orientation analysis on EPMA and XRF chemical maps

Two-dimensional chemical maps were acquired on several thin sections of fault zone material using Wavelength Dispersive Spectroscopy on an Electron Probe Micro Analyzer (WDS-EPMA). These maps have a width and length of several hundred micrometers. Based on these chemical maps of elements, mineral phases were identified and the following geometrical properties of individual grains were measured: the major and minor axes of each grain (r_{min}, r_{max}), the grain orientation φ_{Ros} defined clockwise relative to the North, and the coordinates of the center of each grain (x_c, y_c) **(Fig. 2g)**. These parameters were then used to calculate strain values at micro-scale (micrometer to millimeter). The same procedure was also applied on maps obtained by XRF analysis giving strain values at millimeters to centimeters scale.

3.2.5.3 Strain measurements from rock microstructure using the Fry and R-ϕ methods

Two well-established microstructural methods were used to analyze strain in hand samples and thin sections from rocks of the creeping sections, the Fry method and the R-ϕ method.

Fry method: Also known as center-to-center method (Fry, 1979), this method requires the spatial distribution of strain markers (represented as a cloud of points) to satisfy at least two conditions: to be homogeneous and isotropic (Genier and Epard, 2007). In this method, the center of every strain marker (e.g. oxide grains) is plotted with respect to the position of all other markers. A plot is built by locating one marker at the origin and plotting as dots the positions of all other markers. Then another marker is located at the origin and the positions of all other markers are plotted, until all markers have been considered. The result is a cloud of points that contains an empty space (i. e. void) at the origin and which represents the strain ellipse. Strain anisotropy is quantified using i) the aspect ratio R_{Fry} between the elongation axis (a) and the contraction axis (b) of the strain ellipse; and ii) the angle between the x-axis and the elongation axis also defined as φ_{Fry}. This method is similar to an auto correlation function, which can be used for the same type of object (Heilbronner, 2002; **Heilbronner** and **Barrett**, 2014). The normalized center-to-center method (Erslev, 1988; Erslev and Ge, 1990) improves the Fry method by taking the grain size into account. In the present study, the normalized method was used based on the microstructural data collected.

The strain ellipse parameters (R_{Fry}, φ_{Fry}) were measured by superimposing all minerals together (**Fig. 2h)**. The actual values of the principal strain axes were then obtained using $R_{Fry} = \sqrt{\lambda_1}/\sqrt{\lambda_2}$ in **Eq. 4**, with $\sqrt{\lambda_1} = \sqrt{R_{Fry}(1+\Delta)}$ and $\sqrt{\lambda_2} = \sqrt{(1+\Delta)/R_{Fry}}$.

R-φ method: This method was originally developed to analyze strain for perfectly rounded shape object such as oolites (Cloos, E.; Ramsay 1967; van der Pluijm and Marshak, 2010). However, it can also give some indication on strain processes that involve grain size reduction and grain alignment, by plotting the aspect ratio of the grains $R_{R\varphi}$ as a function of the angle of the grains $\varphi_{R\varphi}$, which ranges from +90° to -90° (positive/negative angles respectively above/below the horizontal axis). This technique produces a cluster of points whose highest spatial density corresponds to the maximum strain value.

In order to find the extreme values the data are binned with respect to the angle as follows. For each binned angle $\varphi_{R\varphi}$ in the interval $\varphi_{R\varphi} - \Delta\varphi_{R\varphi} < \varphi_{R\varphi} < \varphi_{R\varphi} + \Delta\varphi_{R\varphi}$, two kinds of data are calculated: i) the average values $\left(\langle R_{R\varphi}\rangle, \langle\varphi_{R\varphi}\rangle\right)$ and the standard deviation $\left(R_{R\varphi,STD} = \sqrt{\langle R_{R\varphi}^2\rangle - \langle R_{R\varphi}\rangle^2}\right)$, and ii) the maximum average values $\left(\langle R_{R\varphi,max}\rangle, \langle\varphi_{R\varphi,max}\rangle\right)$ (see **Fig 2i**).

3.2.5.4 Strain from volume change due to mass transfer evaluation

The relative mass change can be estimated by comparing the composition of insoluble and soluble minerals between protected (as undeformed as possible) and exposed (deformed) zones at the micro- to meso-scale within a given shear zone (**Fig. 2f**).

The relative mass change is:

$$dm/m = I_p/I_e - 1 \qquad (14)$$

where I_p and I_e are the concentration of all insoluble minerals in the protected and exposed zones, respectively (Gratier et al., 2013). If the rock density does not change, which is the case in the studied samples, the mass change is equivalent to the volume change.

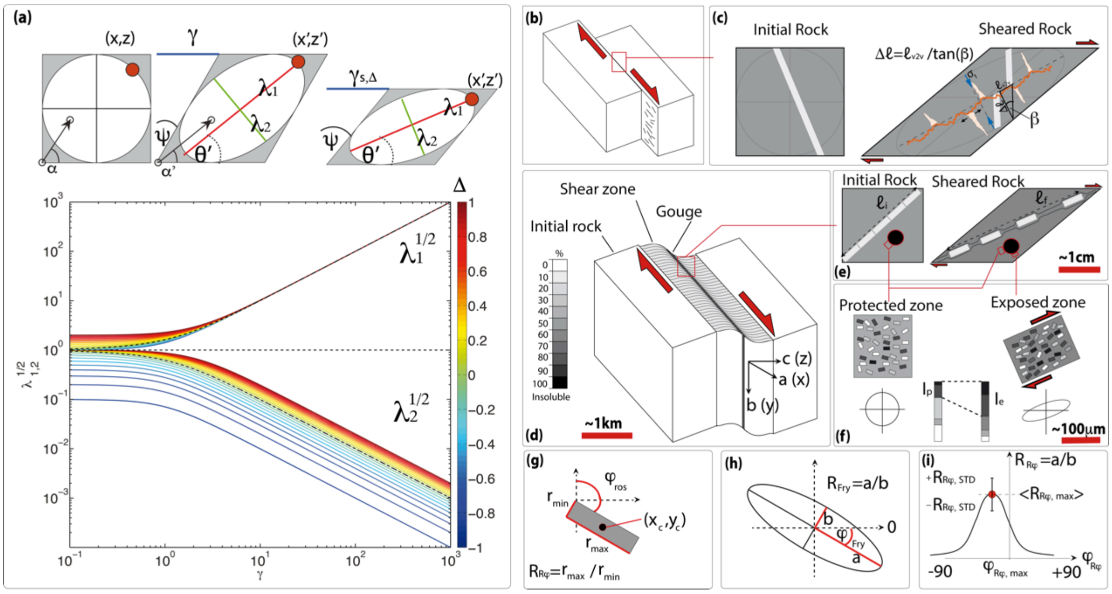

Figure 2. Strain measurements in shear zones. (a) Top: Schematic evolution of simple shear coupled to volume change, with distortion of a unit circle into an ellipse. Bottom: Principal strains as function of shear strain and volume change Δ, adapted from (Ramsay, 1967). (b) Idealization of a fault outcrop in a locked section (c) Characteristic strain markers: tectonic stylolite associated with veins. (d) Idealization of outcrop within the creeping zone with all states of deformation. The kinematic axes are: (a) the direction of shear; (ab) the shear plane; and (ac) the displacement plane. (e) An example of a boudinage strain marker at the meso-scale. (f) Magnification of protected and exposed zones with their mineral composition and strain ellipse. (g) A definition of measured parameters of a single grain: major and minor axes r_{min}, r_{max} the aspect ratio $R_{R\varphi}$ and the angle φ_{Ros}, and the location of the center of the grain (x_c, y_c). (h) Definition of a strain ellipse using the Fry method with major and minor axes a, b and the aspect ratio between them $R_{Fry}=a/b$ with the angle φ_{Fry}. (i) Parameters of the R-φ method: the plot of the aspect ratio of the grains as a function of the angle φ allows evaluating the maximum average values $\left(\langle R_{R\varphi,max}\rangle, \langle \varphi_{R\varphi,max}\rangle\right)$ and the standard deviation $R_{R\varphi,STD}$.

3.3 Result of finite strain measurements at selected sites

The structural strain markers differ from one outcrop to another although all consistent with dextral slip on the North Anatolian Fault. As a consequence, the strain values were extracted using different methods, depending on the particular type of strain markers along the shear zones. For five selected sites (Taskesti, Hamamli, Ismetpasa, Yazioren, Mülayim, **Fig. 1**), strain measurements at thin section scale are shown in **Figures 3, 4, 5, 6,** and **7** (for each outcrop, the mineral maps, mineral content histograms, Fry and rose diagrams have a similar color code). For the last selected site, Gerede (**Fig. 1**), strain measurements are integrated at the outcrop and regional scales **(Fig. 8**).

3.3.1 Taşkesti outcrop (locked section)

The Taşkesti outcrop **(Fig. 1)** exposes the fault zone in massive limestone formations, which are deformed by tectonic stylolites associated with veins as seen in a hand sample (**Fig. 3a**). Six thin sections in three orthogonal planes were cut from this sample. Two types of tectonic stylolites can be distinguished from the different color of their insoluble residues (either red or black color). The stylolites and veins were digitized revealing two generations of veins. The first generation is oriented sub-parallel to the shear plane (ab) and is crosscut by the second generation oriented obliquely (but in places also vertically and perpendicularly) to the shear plane. In places, some of the veins are dissolved and shifted perpendicularly to the stylolite plane, indicating the shortening direction. In other places, some of the horizontal veins are stylolitized, while some vertical stylolites are filled with calcite, indicating successive generations of stylolites and veins in non-coaxial deformation (**Fig. 3b**). **Figure 3c** shows the orientation of stylolite surface and peak (maximum amplitude) directions and the two generations of veins. In more detail, stylolite surfaces are oriented in all directions, with the highest density in the range N30 - N110. The first generation of veins is more frequent in the direction N110. The second generation of veins is distributed in a range of directions N90 - N180, with highest densities at N120 and N150 **(Fig. 3c**).

The total strain was measured from stylolites and veins as follows. Firstly, the extension was measured perpendicular to veins from both the hand sample and thin sections (**Fig. 3a, 3b**). The strain values obtained from the thin sections are slightly higher compared to the hand sample. Secondly, the contraction was quantified by two independent measurements using : i) shifted veins (**Eq. 11**) and ii) stylolite average amplitude (**Eq. 12**). Both methods give very similar results. **Figure 3d** shows the data from veins and stylolites with a fit of the strain ellipse. The main results from these analyses are that, at the scale of ~10 cm, the calculated mass change is $\Delta = 0.08$, and the shear strain values calculated from the stylolite values (as only the stylolites are representative of the creep process) are $\gamma = 0.5$ (with $\sqrt{\lambda_2} = 0.8$) and $\gamma = 0.2$ (with $\sqrt{\lambda_2} = 0.9$), corresponding to the maximum and the mean values, respectively.

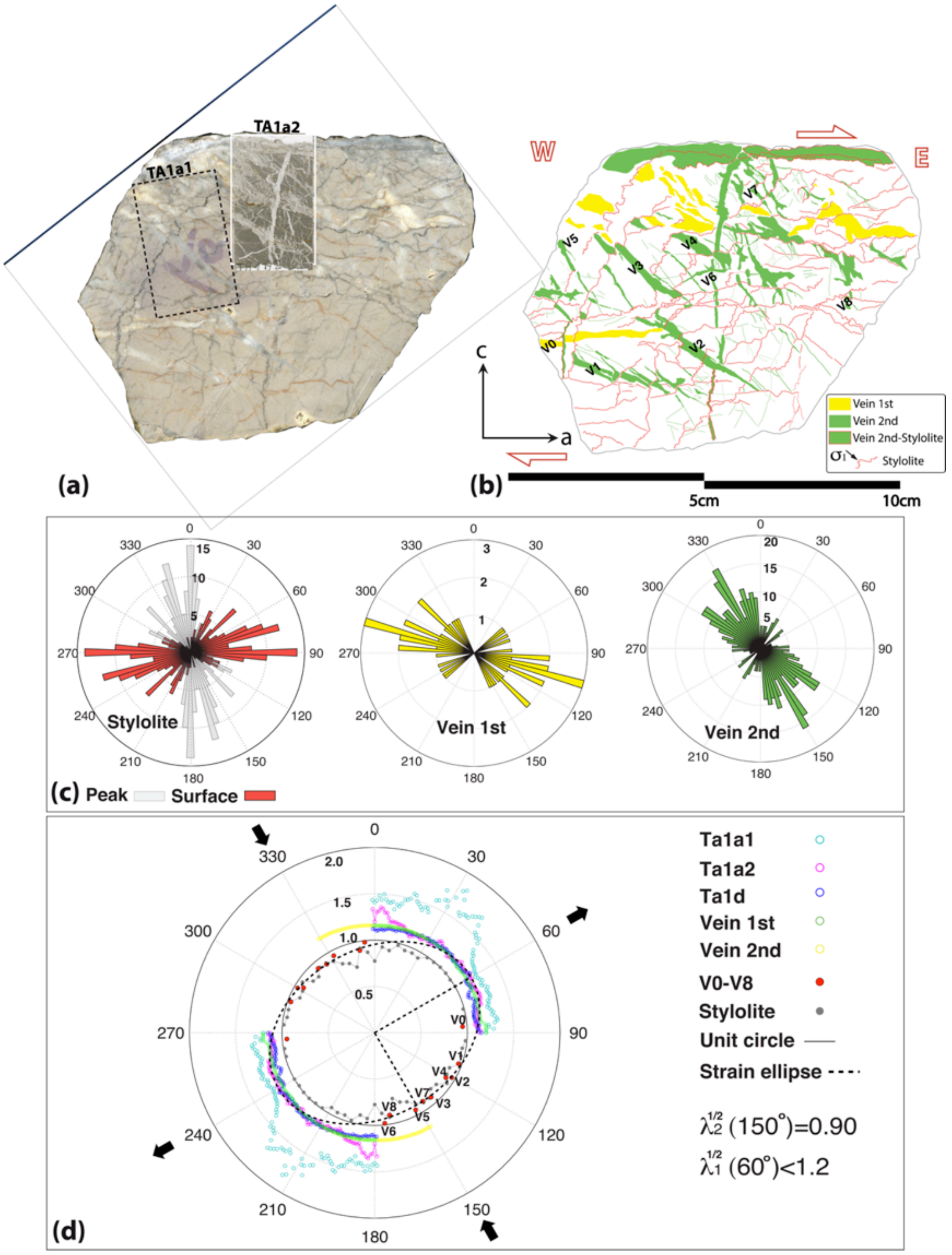

Figure 3. Taskesti outcrop. (a) Limestone hand sample in a horizontal displacement plane (ac, **Fig. 2d**) in the Taşkesti outcrop deformed by tectonic stylolites associated with two families of veins. Locations of the two thin sections Ta1a1 and Ta1a2 are indicated. A third thin-section, Ta1d, is not shown here. (b) Digitized tectonic stylolites and veins. (c) Rose diagrams representing the orientations of the tectonic stylolite surfaces (red) and peaks (gray), and the first and second generations of veins. (d) Strain ellipse based on stylolite and vein

data giving contraction and extension values (black arrows), respectively. The locations of individual veins v1 to v8 are given in (b).

3.3.2 Hamamli outcrop (creeping section)

The Hamamli outcrop **(Fig. 1)** exposes serpentinite rocks deformed by dissolution along cleavage surfaces associated with precipitation in veins (Kaduri et al., 2017). In places, the strain can be measured by the alignment of iron oxide minerals that agglomerate sub-parallel to the cleavages. The strain was measured along two planes: a shear plane on the fault (ab) and a displacement plane (ac) (**Fig. 2d**). The results are presented in **Fig. 4**. The strain values are $R_{Fry} = 2.25$ and $R_{Fry} = 3.20$ in the shear fault plane (ab) (**Fig. 4a**) and in the displacement plane (ac) (**Fig. 4b**), respectively. Rose diagrams of the iron oxides show alignments in the strain elongation direction in the displacement plane (**Fig. 4b**) but are slightly oblique to the strain elongation in the shear plane (**Fig. 4a**). This may be due to the effect of episodic oblique displacements along the fault surface. Because it was not possible to find an area that was less deformed than the studied samples, it was not possible to calculate the mass change. It is then simply assumed that the relative mass change between all the studied samples is 0. Assuming $\Delta = 0$, the actual strain parameter values for the shear fault plane are $\sqrt{\lambda_1} = 1.50$ and $\sqrt{\lambda_2} = 0.67$, and for the displacement plane $\sqrt{\lambda_1} = 1.79$ and $\sqrt{\lambda_2} = 0.55$. A maximum shear strain value in the displacement plane $\gamma = 1.26$ is derived from **Eq. 3** (**Fig. 2a**).

The R-φ method shows that $\langle R_{R\varphi} \rangle = 1.83$ in the shear - fault plane, and $\langle R_{R\varphi} \rangle = 2.2$ in the displacement plane. These values are in agreement with the results of the Fry method. The relatively large dispersion of the strain values is discussed in section **§4.2**.

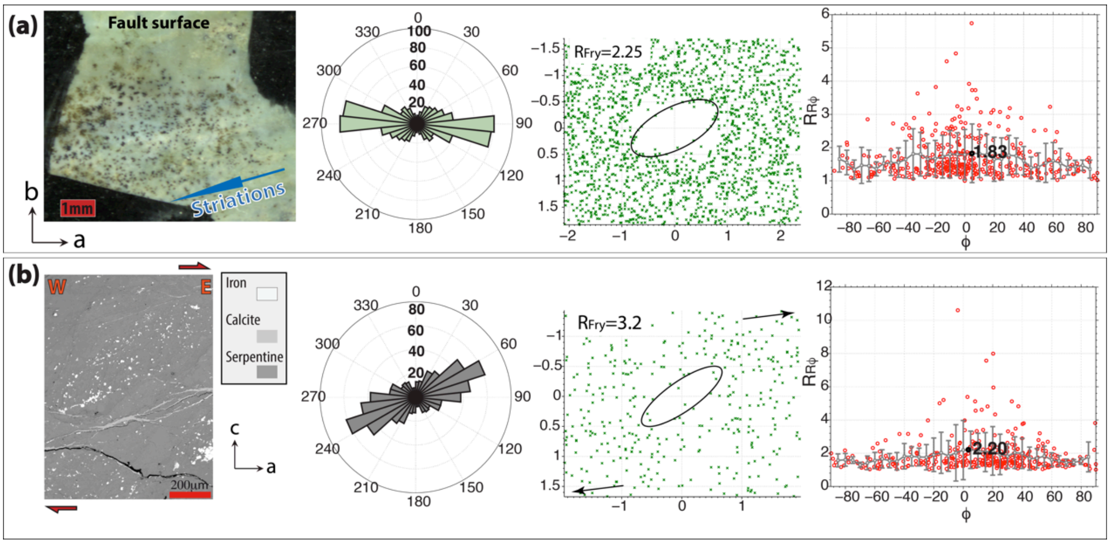

Figure 4. Hamamli outcrop: serpentine rocks show cleavage-foliation, and anisotropic clustering of iron oxide minerals in the cleavage. These microstructures are used to evaluate the strain values in two directions. (a) Strain analysis of a fault surface in vertical shear plane (ab), with the rose diagram of Fe oxides, and plots of the normalized Fry and R-φ methods. For this last method, the red dots are data measurements, gray solid lines are mean values with standard deviation. (b) Strain analysis with the same three methods in a horizontal displacement plane (ac).

3.3.3 Ismetpasa outcrop (creeping section)

The Ismetpasa outcrop **(Fig. 1)** exposes the fault where sandstone-shale units are juxtaposed with volcanic rocks. At this site, the deformation in the gouge is associated with tectonic layering with two types of deformed foliated rocks: F-gouge (fine-grained) and G-gouge (large-grained). The foliations are deformed around rigid plagioclase clasts, with some surrounding residual domains of the initial (undeformed) rock (**Fig. 5a**). **Figure 5a** shows a digitized horizontal thin section, parallel to the displacement plane (ac) of the shear zone, with XRF maps of Si and Al indicating both the composition variation between the gouge layers and grain alignment, as well as the overall train variation of these zones based on the Fry-method (**Fig. 5b**).

Unfortunately, there is no direct evidence of strain markers at meso-scale at this site. However, it was possible to calculate the strain distribution within this **Fig. 5a** thin section by combining Fry-method measurements and the relative mass change calculated from maps of mineral content. The mineral and structural analyses were based on seven maps of minerals acquired in exposed (the most deformed areas) and protected zones (the less deformed areas) of the thin section (see location in **Fig. 5a**). In both types of gouge there is a decrease in soluble mineral content from the protected zones to the exposed zones (**Fig. 5d**). The mineral assemblage is composed of albite, anorthite, orthoclase, calcite, magnesite, quartz, smectite, iron oxide and titanium oxide. Some of the maps were masked in order to obtain a more accurate evaluation of localized strain and minerals composition (**Fig. 5c**). The relative mass change is calculated for the two types of gouge layers (F-gouge and G-gouge) separately using masks, and excluding magnesite and calcite from the calculation considering that these minerals sealed the porosity of the rock more recently in the deformation process and at least after the process of massive deformation considered here (Kaduri et al., 2017).

The strain was measured using the Fry method and R_{Fry} values for few representative minerals (albite, anorthite, orthoclase, quartz, smectite). These values are plotted as a function of the relative mass change and show a near-linear trend (**Fig. 5e**). The values of R_{Fry} converted to quadratic contraction/extension$\sqrt{\lambda_{1,2}}$ using the Δ values, as described in section §**2.3**, show the actual successive change in the deformation as a function of the relative mass change. Among the maximum shear strain values is the one given by map 2 with $\gamma = 1.2$ with $R_{Fry} = 7.3$ and $\Delta = -0.66$ (**Fig. 5f**). The orientation of the grains in the exposed zones is most often aligned with the local foliation. Orientations may locally vary when there is some local folding (maps 4 and 6). On the contrary, the protected zones show random grain distribution with negligible preferred orientation: maps 7b and 3a, (**Fig. 5g**).

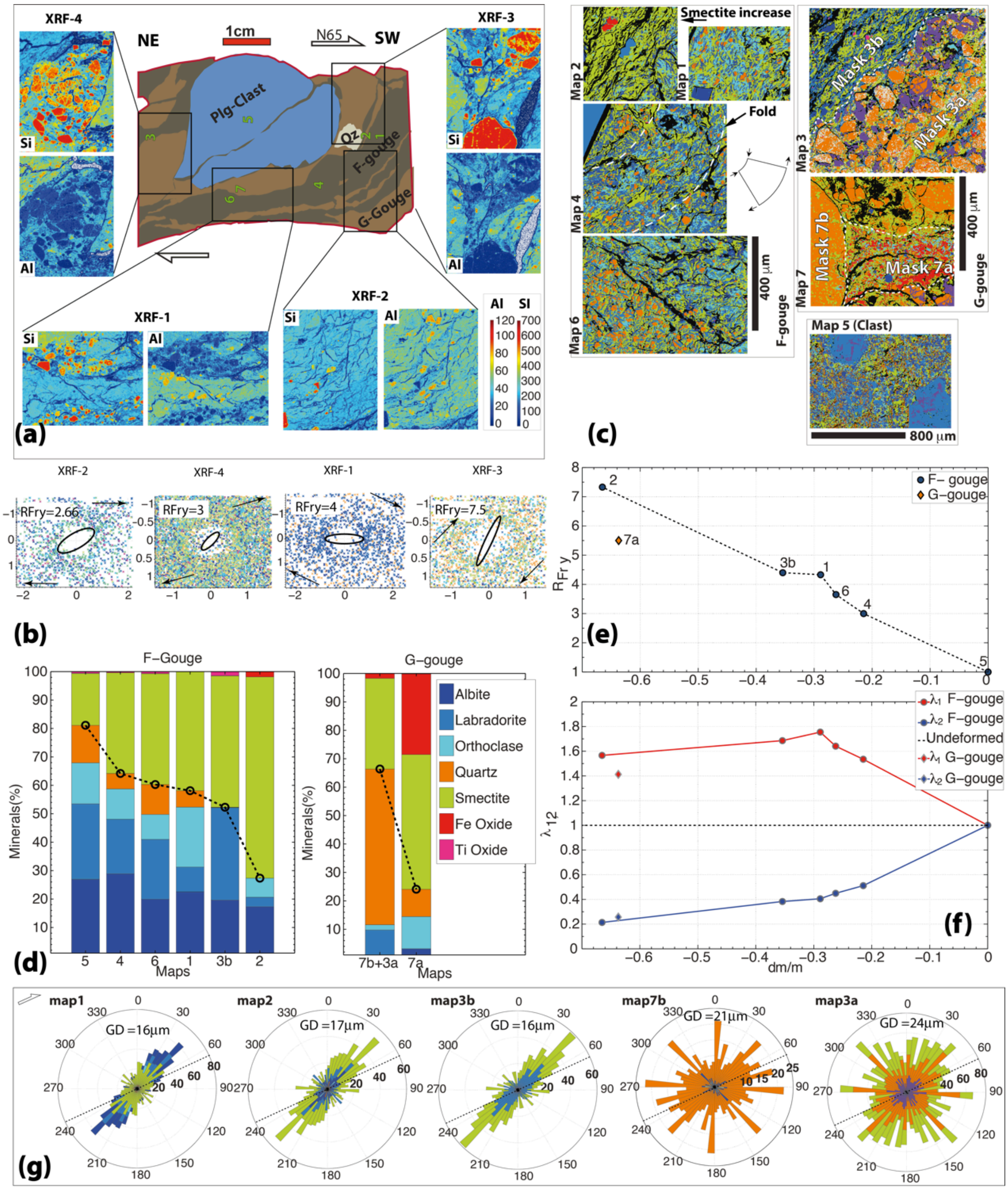

Figure 5. Ismetpasa outcrop. (a) Thin section with two types of gouge layers, foliated and granular gouge (F-gouge and G-gouge), around a rigid clast of plagioclase, with the location of mineral maps and XRF maps of silicon and aluminum in horizontal displacement plane (ac). (b) Fry method based on XRF maps. (c) Masked maps of minerals sorted by insoluble minerals for both F-gouge and G-gouge (each color corresponds to a different mineral, given in the legend in d). (d) Mineral content of the mineral map for F-gouge and G-gouge. (e) Strain measurements using the Fry method and R_{Fry} plotted as a function of the relative mass change. The references (protected zones) for F-gouge is map 5 and for G-gouge a combination of maps 3a and 7b. (f) Plot of the calculated quadratic contraction/extension as function of the relative mass change. (g) Rose diagrams of grain orientations from mineral maps with mean grain diameters (GD). The color code is the same in d and g.

3.3.4 Yazioren outcrop (creeping section)

The Yazioren outcrop **(Fig. 1**) exposes a shear zone in a mélange of carbonate and volcanic rocks with tectonic layering (rich in alumino-silicates) and apparent carbonate boudinage. A horizontal thin section parallel to the displacement plane (ac) of the shear zone was imaged by XRF in order to segment and measure strain markers. The strain measurement included two main steps. The first step was to measure the quadratic extension $\sqrt{\lambda_1}$ using boudinage. The second step was to measure the deformation recorded by the nearby matrix using the Fry method on maps of elements acquired from EPMA measurements.

Figure 6a shows a calcium map, which emphasizes the carbonate boudinage. The quadratic extension is measured along the preserved boudinage (1-8), and varies in the range 1.82-4.13. Several maps of minerals were then acquired (their location is marked with rectangles map1-map13 on **Fig. 6a**) in order to measure the strain values and the relative mass change in the deformed matrix located in the vicinity of the boudinage. The foliation is emphasized by the XRF aluminum map (**Fig. 6b**). In addition, the boudinaged clasts are dissolved by stylolites oriented perpendicular to the extension direction. In this case it was possible to measure the contraction component related only to stylolite formation (see **Eq. 12** and section **§2.3**), and the maximum value obtained is $\sqrt{\lambda_2}$=0.8.

The relative mass change was calculated using nine mineral maps acquired in different zones, one in the protected zone (i.e. initial rock), and eight in several exposed zones (i.e. deformed rock) along the boudinage **(Fig. 6a)**. **Figure. 6c** shows an example of a BSE-SEM image of carbonate clast with mineral maps at one exposed zone (map13) and one protected zone (pressure shadow contoured with a dashed line in map2). The mineral assemblage shows a reduction in soluble mineral content and a relative increase in insoluble mineral content (clay, chlorite, mica, anatase and pyrite) from the protected to the more exposed zones (**Fig. 6d**). This allows calculating the mass change relative to the protected zone **(**map2), (**Fig. 6g**). It must be noted that such mass change values are only minimum values since the protected zone is not an initial state but rather a less deformed state as attested by the preferred orientation of the grains (**Fig. 6h**). An average strain value was obtained by the Fry method at centimeter scale by using thresholded XRF elemental maps and we obtain $R_{Fry} = 2.75$ (**Fig. 6e**). Measuring R_{Fry} values at a smaller scale (100 microns) based on the mineral map reveals a good correlation between the R_{Fry} values of the deformed matrix in exposed zones and the extension of the boudinage $\sqrt{\lambda_1}$ (a fitted linear regression gives a slope equal to 0.9**, Fig. 6f)**. There is also a near-linear trend between these strain values evaluated by two different methods, $\sqrt{\lambda_1}$ and R_{Fry}, and the mass change **(Fig. 6g)**. Finally, based on these measurements from boudinage and Fry method, values of maximum shear strain were found to be in the range $\gamma = 0.5 – 1.5$.

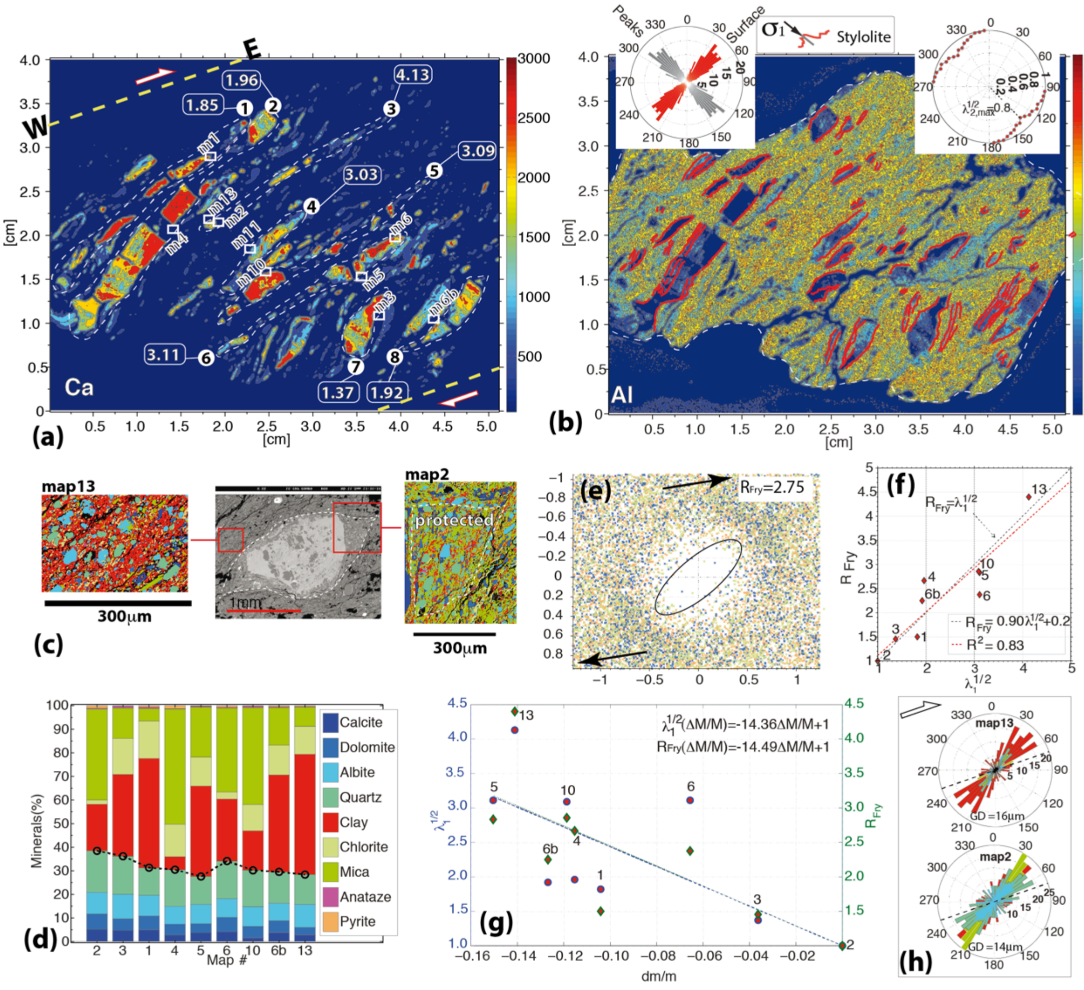

Figure 6. Yazioren outcrop. (a) Calcium map measured by XRF showing boudinage with variation in extensional strain in the range 1.82-4.13 in the horizontal displacement plane (ac). The locations of the mineral maps are indicated. (b) Aluminum map measured by XRF showing the foliation. In (a) and (b) color bars indicate relative content. (c) SEM-BSE images showing exposed and protected zones (in the middle), with mineral maps from the protected (left) and exposed (right) zones. The color-coding for the minerals is given in the legend of d). (d) Comparative mineral compositions, the dashed line separates soluble (mobile) and insoluble (non-mobile) minerals. (e) Fry diagram at centimeter scale on XRF data. (f) Correlation between the extension of the boudinage and R_{Fry} of the nearby matrix. (g) Extension values (from boudinage) and R_{Fry} (from mineral map) versus the relative mass

change. (h) Rose diagrams of grain orientations from mineral maps with mean grain diameters (GD).

3.3.5 Mülayim outcrop (creeping section)

In this outcrop **(Fig. 1)** the fault crosscuts a block of ophiolitic mélange embedded into schist, marble and metabasite units. Deformation was recorded on the basis of folded carbonate veins and aluminosilicate-rich tectonic layering. A horizontal thin section parallel to the displacement plane (ac) revealed a shear zone with cleavage - foliation sub-parallel to the fault and crosscut by carbonate veins in all directions (**Fig. 7a**). The cleavage can be seen on the XRF aluminum map (**Fig. 7b**). The first generation includes veins (100-500µm thick) sub-parallel to the cleavage and folded veins perpendicular to the cleavage, which are crosscut by the second generation of veins (~5mm thick) running perpendicularly/obliquely to the cleavage (in Riedel shear position). The folded veins crosscut two types of layers: a first one being rich in mica and clay and a second one being rich in albite and dolomite. The general extension due to the first veins parallel to the cleavage is $\sqrt{\lambda_1}(0°) = 1.05$, and for the second veins perpendicular/oblique to the cleavage $\sqrt{\lambda_1}(90°) = 1.2$. The shortening calculated from the folded vein at a sampling resolution of dx=100µm (extracted from Ca-XRF map), using **Eq.13,** shows $\sqrt{\lambda_2}|_{dx=100\mu m}(0°) = 0.45$. Taking into account the veins parallel to the cleavage, the contraction may be reduced to 1.05 x 0.45 = 0.47. **(Fig. 7a)**. This corresponds to a volume change of Δ= (1.2 x 0.47) – 1 = – 0.44 at the decimeter scale. At a smaller scale (microprobe analysis), due to the lack of clear evidence of undeformed (or at least less deformed protected zones), it was impossible to evaluate the relative mass change with confidence, despite foliation being visible.

Nonetheless, some strain evolution can be seen. At the micrometer scale, mineral maps show asymmetric centimeter-scale folds crosscut by a folded calcite vein with about the same $\sqrt{\lambda_2}$ values as that measured at larger scale (0.45). In order to compare the variation in strain along the fold, the Fry method is applied in three different zones: the hinge (H), an intermediate area (I) and the limb (L) of the fold **(Fig.7d)**. Results show a variation in local strain values measured by the parameter R_{Fry} **(Fig.7e)**. The deformation evaluated from the Fry method using large-scale XRF aluminum maps has a relatively high value R_{Fry} = 8.0 **(Fig. 7c),** corresponding to a shear strain $\gamma = 2$ when using the associated volume change of – 0.44 (see §**2.3)**. It must be noted that such shear strain value, higher at decimeter scale than at millimeter scale, implies the existence of some highly localized zones with very high strain values at the millimeter scale or below that we could not identify nor measure. Moreover, the general cleavage-foliation at the decimeter scale (**Fig. 7b**) is sub-parallel to the shear direction **(Fig. 7f)** and this can also be used to evaluate the amplitude of shear strain.

More precisely, the distribution of the orientation of clusters of grains containing aluminum may be fitted with two normal probability density functions (PDF, **Fig. 7f**). The first normal distribution represents the small angles where the long axis of the elongated grain clusters can be assimilated to cleavage planes and the second normal distribution describes the entire range of angles. The characteristics of these two distributions (mean angle with the shear zone and standard deviation) are given in **Fig. 7f.** These two normal distributions correspond to two sets of strain values. The first set is given by the R_{Fry} values ranging from 1.42 to 8 **(Fig. 7c, e),** for strain ellipses associated with grain orientations oblique to the shear zone. It has a maximum shear strain $\gamma = 2$. A second set of strain values corresponds to areas with a mean orientation of the cleavage almost parallel to the shear zone **(Fig. 7a).** Such very low angles indicate very large shear values (Ramsay, 1980). In section **4.2,** a forward modeling approach is presented that involves volume change and high shear strain in deformation zones and allows to compute the resulting shear strain γ. This model shows that γ may indeed reach very high values, up to $\gamma = 100$ depending on the volume change. We thus argue that the fault zone can be seen as a combination of (1) very narrow, localized shear zones with cleavage parallel to them and high strain values that can not be resolved by the Fry method, and (2) wider shear zones with cleavage oblique to them and lower strain values measurable by the Fry method. The ratio of the standard deviations of the two normal probability density functions for these narrow/high strain and wide/low strain shear zones (2.5° and 42°, respectively, Fig.7f) is assumed to correspond to the ratio of the cumulated widths of these two zones. This ratio is then 2.5/42=0.06 at the scale of a thin section.

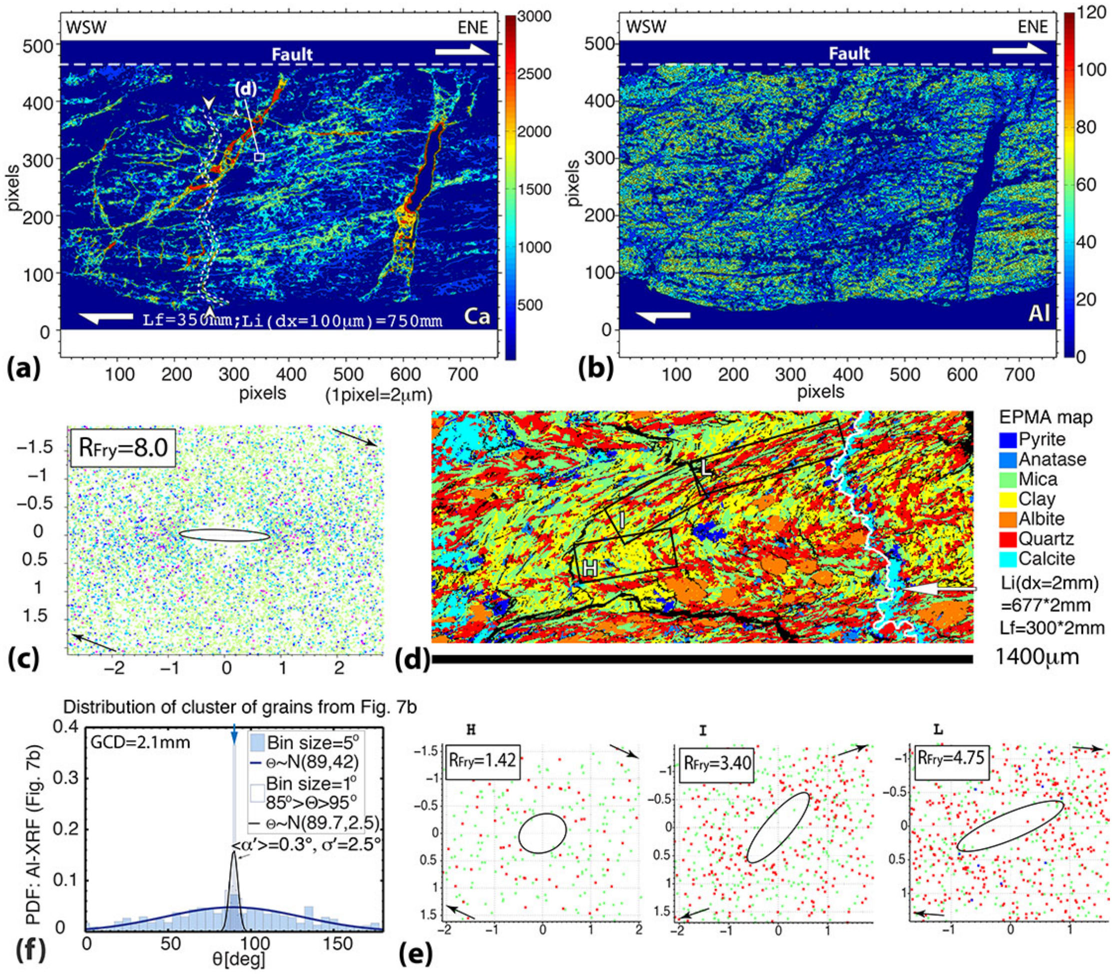

Figure 7. Mülayim outcrop. (a) Calcium map in the horizontal displacement plane (ac**)** measured by XRF with a folded calcite vein (ptygmatic vein) shown between arrows along dashed white lines. (b) Aluminum map in the same sample indicates sub-parallel cleavage-foliation rich in mica. In (a) an d (b), color bars indicate relative content. (c) Fry diagram based on XRF-maps. (d) Mineral maps with fold separated by masks in the hinge, the intermediate area and the limb with different cleavage angles (locations are given in **Fig. 7a**). (e) Fry diagram based on the selected zones of the mineral map with increasing values of $R_{Fry}$from hinge to limb. (f) Orientation distribution of clusters of grain containing Al (**Fig. 7b**) fitted by two normal probability density functions (PDF), with the mean diameter of the grain clusters containing aluminum (GCD). Parameters of the two distributions are <α'> the mean angle within the shear zone and σ' the standard deviation: <α'> = 1° and 0.3° and σ'= 42° and 2.5° for the wide and narrow distributions, respectively. (g) Rose diagrams of grain orientation in the areas of **Fig. 7e** from mineral maps, with the mean grain diameters (GD).

3.3.6 Gerede outcrop (creeping section)

The Gerede outcrop **(Fig. 1 and 8b**) is an abandoned quarry at the western end of the Ismetpasa creeping segment (Hussain et al., 2016; Cetin et al., 2014). It is located one kilometer south of the present-day active fault zone with several other major strike-slip faults in between mostly buried under quaternary sediments (Kaduri et al., 2017). The quarry presents a continuous 150 m-wide outcrop (**Fig. 8a**) that reveals a network of 5 to 30 cm thick clay-rich soft gouges with parallel-to-the-fault cleavage-foliation (**Fig. 8a-c-d**). These faults cross the volcanic units of the Galatia massif (Adiyaman et al., 2001), which are a mélange of dacite, andesite and trachy-basalts (Wilson et al., 1997). These different units are difficult to distinguish. In the gouges, they have been transformed by deformation (Kaduri et al., 2017). In the damage zones, they have been highly damaged with fractured blocks and very dense networks of vertical veins in all directions (**Fig. 8e**). Such sealed fractures are related to episodic inflow events of carbonate-rich fluids that were associated with the successive earthquakes that affected this NAF section (Kaduri et al., 2017).

Moreover, the deformation is heterogeneous with more or less rigid fractured blocks surrounded by foliated zones with intense deformation displaying a braided fault pattern at all scales, from thin section (**Fig. 5a**) to regional scale (**Fig. 8a**). The size of such rigid blocks decreases drastically in gouges and in zones with cleavage parallel to the shear fault but the boundaries of such zones are undulated and their widths vary along strike (**Fig. 8a-c-d**).

In thin sections, only some islands of volcanic rocks can be seen between the networks of veins. Consequently it is not possible to evaluate the strain and shear values using particle distribution as in the other studied outcrops. However, it is possible to evaluate the shear values from the angles between the cleavage and the shear planes as it was done at microstructural scale for the Mülayim outcrop (**Fig. 7f**). Such angles can be measured either directly on the field or in thin sections. It is not possible to measure the evolution of these angles along a continuous path all along the 150 m of the outcrop. However, the damage zones appear to be more layered in areas nearby the gouges than away from them (**Fig. 8c-d**).Thin sections show that in these areas nearby the gouges the orientation of the cleavage is parallel to the shear plane fault (**Fig. 8f-g-h**), whereas away from the gouge the cleavage is oblique to the fault (**Figs. 5g, 6h, 8e**). It is thus possible to evaluate the cumulative width of the shear zones with parallel cleavage at the scale of the outcrop. Such shear zones include all the gouges plus damage zones around them that have the same structural aspect as that seen on thin sections showing cleavage parallel to the fault (**Fig. 8f-g**). These zones are highlighted in near-transparent white in **Fig. 8a-c-d** and a cumulated width of 6 m is found along the 150 m width of the quarry.

Finally, the ratio between the cumulated widths of shear zones with parallel-to-the-fault cleavage and shear zones with oblique-to-the-fault cleavage may be evaluated as 6/150 = 0.04. This can be considered as a representative value at regional scale (100-1000m). This ratio is slightly lower than the one (0.06) at thin section scale (1-10cm) in the Mülayim outcrop (**Fig. 7f**), but of the same order of magnitude. It is worth noting that the dispersed narrowest gouges of centimeter width were not taken into account here considering that they represent only a minor part of the high strain shear zones. The evaluation of the shear strain values that are associated with cleavage sub-parallel to the fault is not easy. As previously mentioned, forward modeling is used in section **4.2** to show that values as high as $\gamma = 100$ are likely in such zones. This high shear strain value and the width of the shear zones with fault parallel cleavage are used in the estimation of the total fault displacement accommodated by creep during geological times in section **4.3**.

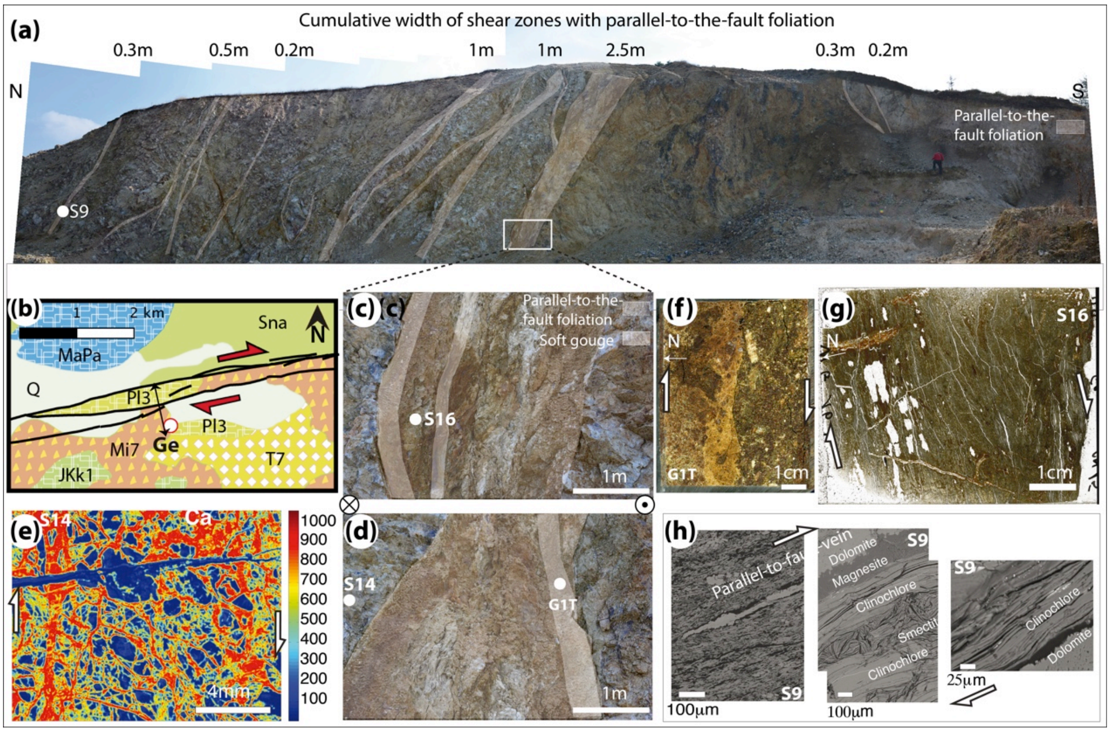

Figure 8. Gerede outcrop. (a) Photograph of the 150 m-wide outcrop showing the fault network and the location and widths of zones (shaded in white) with parallel-to-the-fault cleavage/foliation. (b) Geological map: Q=Quaternary, Pl3=Pleistocene conglomerate sandstone, M7=Miocene agglomerate tuff, T7=Eocene andesite basalt, MaPa=Cretaceous limestone, Sna=Cretaceous limestone, JKk1=Jurassic limestone. (c) Zone with parallel-to-the-fault cleavage and soft gouge in the upper part of the quarry: see location in (a). (d) Zone with parallel-to-the-fault cleavage and soft gouge in the lower part of the quarry (not seen in a). (e) Chemical map of Ca elements using XRF with typical network of calcite - dolomite veins parallel and perpendicular to the cleavage. The blue perpendicular-to-the-fault vein is a late

magnesite vein. (f) Parallel-to-the-fault cleavage in thin section of soft gouge. (h) Parallel-to-the-fault cleavage in thin section nearby the gouge (see location in c). (g) Parallel-to-the-fault cleavage in SEM image with dolomite and magnesite veins parallel to the fault and to the cleavage - foliation (layers of clinochlore and smectite).

3.4 Discussion

3.4.1 Deformation mechanisms and effect of rock lithology determined from the relationship between shear strain and volume change

The aim here is to discuss the relationship between strain and mass-volume change (**Fig. 9**) that can be used to characterize both the deformation mechanisms and the effect of rock lithology. The first observation is the wide variation in measured shear strain values: the ratio between the principal strain axes (R) ranges from close to 1 in the massive limestone of Taşkesti (**Fig. 3**), to 7.5 (Ismetpasa, **Fig. 4**) and 8 (Mülayim, **Fig. 7**) in volcanic rocks. Even at the same site, the strain values vary widely, for example from 1.4 to 8 in Mülayim at micrometer to millimeter scales. Strain values are even much larger (40 times higher) if strain values at decimeter to hectometer scales are taken into account, derived from the angles of the cleavage with the shear zone as in Mülayim (**Fig. 7f**) or Gerede (**Fig. 8**). This is discussed in details in the next section **(§4.2**) as at these scales, variation in strain versus mass and volume changes cannot be quantified from a single value

It is worth noting that the calculated mass change is a relative value. It is obtained by comparing a deformed "exposed" area with a "protected" area which is either undeformed (in the best case) or which is just less deformed. It is also important to mention that the calculation is relative to a given volume, which is the volume of the studied sample. Finding a mass decrease, for example, means that some part of the mineral was removed by mass transfer during deformation at the scale of the studied sample where the system is open. Finding no mass change does not mean that no mass transfer occurred but could mean that the transfer occurred at a size smaller than the sample size and that the system is closed at the size of the studied samples, with, for example, the same amount of dissolution and reprecipitation in the case of a pressure solution process. Moreover, as the rock density does not significantly change, mass change is equivalent to volume change. These preliminary definitions being given, the relations between strain and volume change can now be discussed.

Two types of samples show almost no (or very little) volume change in **Fig. 9**, but their significance is completely different. Along the locked section in the Taşkesti massive limestones, the deformation near the fault is not associated with any significant volume change at the measured outcrop scale (cm to dm) **(Fig. 3)**. The calculated volume change is $\Delta = 0.08$, with extension and shortening values of $\sqrt{\lambda_1} = 1.2$ and $\sqrt{\lambda_2} = 0.9$, respectively. Therefore, the system appears to be almost closed. But there is no way of knowing whether the calcite that dissolved in stylolites is the same as that reprecipitated in the veins. So the systems could just as well have been opened with successive steps of dissolution and vein sealing. From the observations (**Fig. 3**), it is clear that the deformation conditions (fluid composition and temperature) have evolved with time as indicated by the different colors of the insoluble stylolite residues (red or black). There are also at least two generations of veins indicating that the stress field changed slightly during shear deformation. Plastic deformation can be also seen in veins where calcite deformed later by mechanical twinning. This complexity is probably linked to the major effect of successive earthquakes along this section (Kaduri et al., 2017). Other samples are displayed without volume change in **Fig. 9**, which corresponds to the Mülayim outcrop. In this case, a network of spaced cleavage at micrometers scale was observed sub-parallel to the shear zone (**Fig. 7b**) with alternating zones more or less rich in soluble and insoluble species that are likely to indicate mass transfer. However, it was not possible to find an area representative of an initial state so it was not possible to evaluate volume change below millimeter size. But at this Mülayim site volume change of -44%. have been measured at decimeter scale using folds and veins markers.

At other sites as Ismetpasa (**Fig. 5e-f**) and Yazioren (**Fig. 6g**), a clear correlation was measured between the strain calculated with the Fry method and rigid objects elongation and the volume change, indicating that the same pressure solution mechanism is responsible for the deformation. However the correlation exists for relatively small values of volume change (less than 30% in Ismetpasa, **Fig. 5f**). Above these volume change values the strain increases without increase of the volume change. The explanation is related to an evolution in the deformation mechanism. The pressure solution process evolves with increasing strain (Gratier, et al., 2013; Kaduri et al., 2017). Soluble species (here mainly quartz and feldspars) are dissolved along solution cleavage surfaces leading to the passive concentration of insoluble species (phyllosilicates) in an open system. The dissolution process probably initiates along single solution cleavage planes near rigid objects (**Fig. 5a**) and develops progressively further away. In the context of an active fault, this dissolution is probably activated by seismic fracturing and comminution processes (Steward et al., 2000; Imber et al., 2001; Jefferies et al., 2006). At this stage, the tectonic layering process, seen as a cleavage-foliation in all the largely deformed samples (**Figs. 5, 6, 7**), developed as a self-organized process as a result of stress-driven chemical effects. This process of dissolution of soluble elements and passive concentration of insoluble elements has been reproduced experimentally (Gratier et al., 2015). It contributes to the commonly observed anisotropy of fault rocks (Collettini, et al., 2009). Then, at a later stage when only a small amount of soluble species remains and/or when the grain size is sufficiently reduced, the deformation process switches to grain boundary sliding. This mechanism can always be a pressure solution process at grain size scale in order to accommodate relative grain displacement (Ashby and Verrall, 1973), the distance of transfer being reduced to the size of the asperities along the grain boundaries. Consequently, the strain rate of such viscous behavior probably increases significantly for a given stress state (Gratier et al., 2013). The system can then evolve to a combined frictional and viscous flow behavior (Bos and Spiers, 2002) or depend only on the friction of individual minerals and on the geometry of their assemblage if no mass transfer is possible anymore (Lockner et al., 2011; Sone et al., 2012; Carpenter et al., 2016).

At the Hamamli site, the deformation measured in serpentinites is also relatively small (**Fig. 4**) : the strain ratio deduced from R-**φ** and Fry methods is ranging from 2.25 to 3.2. It was not possible to calculate a volume change as no area less deformed than any other was found. The behavior of this outcrop is in-between that of the limestones (Taşkesti) and that of the volcanic rocks (Ismetpasa, Yazioren, Mülayim). This indicates that in the absence of significant tectonic or metamorphic transformations, the serpentines do not appear to be weak rocks.

The contrasting behavior of the limestone versus the volcanic rocks may be explained by the contrasting behavior of monomineralic (limestone) rocks and polymineralic (volcanic) rocks (Kaduri et al., 2017). Monomineralic rocks do not deform at grain scale in the locked section (**Fig. 3**) and are hardly deformed at grain scale in some parts of the creeping zone except by dissolution along microstylolites at veins (**Fig. 3,**

6) or at quartz clast boundaries (**Fig. 5a**). Conversely, polymineralic rocks in the creeping section show very efficient dissolution at grain scale leading to the dissolution of a large part of the more soluble grains (**Figs. 4, 5, 6, 7**). The reason for this is that diffusion at the contact surface between two identical minerals, whose boundaries are most often healed, is much slower than diffusion at the contact surface between minerals of different nature, where the fluid phase boundary is more continuous (Zubtsov et al., 2004). The difference of behavior is even greater if one of the minerals is a phyllosilicate, which prevents healing (Bos and Spiers, 2000; Zubtsov et al., 2004) or activates dissolution (Renard et al., 2001). This concept that creep deformation is controlled by lithology is supported by a wide range of observations in several major creeping faults (Graymer et al., 2005; Sone et al., 2012; Richard et al., 2014; Thomas et al., 2014; Kaduri et al., 2017).

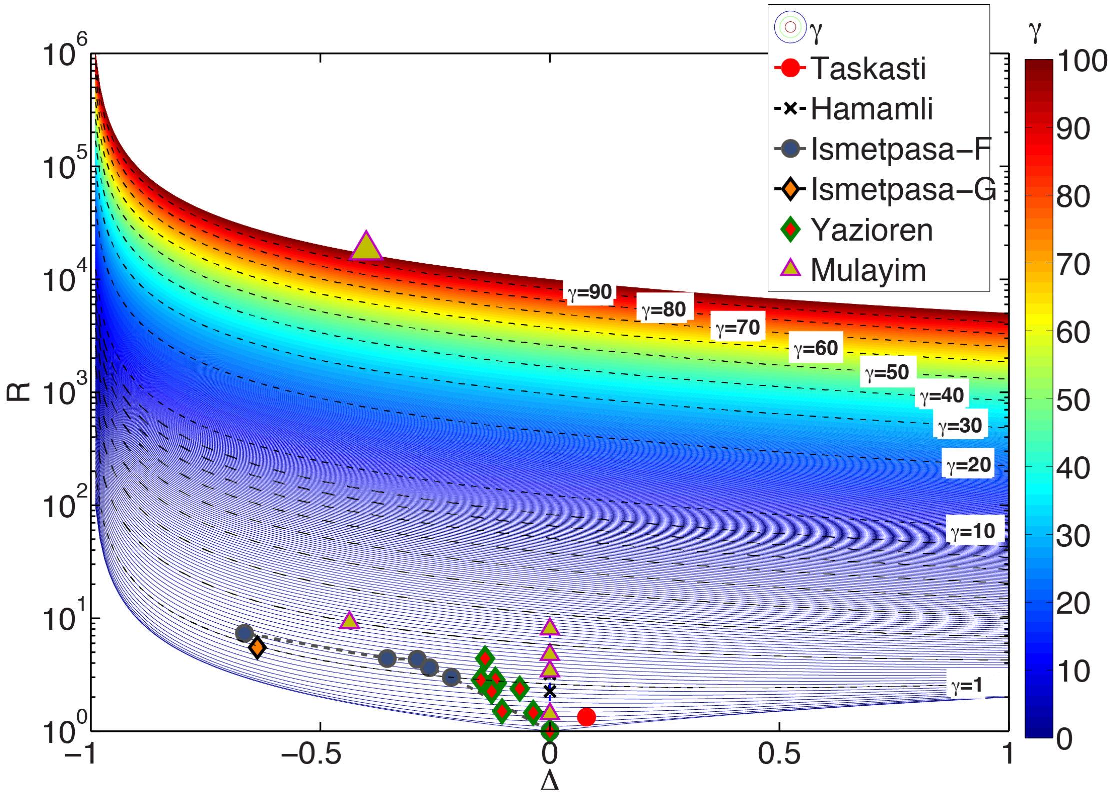

Figure 9. Plot of all finite strain and mass-volume change measurements calculated from various microstructural methods. The principal strain axis aspect ratio (R) is plotted versus the relative mass and volume change (Δ) and the finite shear strain (lines of various color from γ =0 -blue- to γ =100 -dark red). Highly contrasted shear strain values γ are found at the Mülayim site, depending on the measurement methods, ranging from 1.5±1 to 100 using Fry method (small triangle) or angle between cleavage and shear zone (large triangle), respectively (see also **Fig. 10**). Other symbols refer to sites in **Figs. 3** (Taşkesti), **4** (Hamamli), **5** (Ismetpasa), **6** (Yazioren) and **7** (Mülayim).

3.4.2 Considering the wide range of strain values in order to calculate the aseismic displacement

Two parameters are needed in order to calculate the displacement associated with creep processes at the scale of the fault zone: the value of the finite creep-related strain and the width of the shear zone (**Eq. 10**). This subsection addresses the first parameter (Ramsay, 1980; Ramsay and Graham, 1970). The evaluation of the creeping zone width is discussed in section **4.3** as well as the modeling of the total aseismic displacement.

3.4.2.1 The challenge of strain measurements in case of strain and volume change

As shear strain has a very wide range of values, its evaluation may be highly dependent on the strain measurement method. For example in Mülayim **(Fig. 9)**, the values of γ given by R_{Fry} reach 2 at maximum (when considering the volume change), although very low angle values between cleavage-foliation and shear zone are observed, indicating that much higher γ values should be expected. When the γ values are calculated from the distortion of cleavage planes that initiated at 45° and whose angle θ' decreases with finite deformation down to very small values of 1°, 0.5° or 0.1°, the values of γ may reach values of 57, 114, or 572, respectively (see **Eqs. 8 - 9**). Consequently, estimating γ from θ' is extremely challenging for high strain values, due to the difficulty of measuring θ' with enough accuracy when it is smaller than 1°. Measuring γ becomes even more challenging when volume change is involved. For instance, when considering $\theta' = 1°$, with $\Delta = 0$ or $\Delta = -0.7$ (using **Eq. 8**), γ changes significantly from $\gamma = 57$ to $\gamma = 17$, respectively. This uncertainty is difficult to reduce because the evaluation of the volume change depends to a large extent on the size of the measured area and on the possibility of finding an initial undeformed state (see **§4.1**).

With the Fry method, the main challenge of measuring high strain values is that the elliptic void in the cloud of points becomes very narrow and elongated and it becomes more and more difficult to identify it when the strain increases. This is particularly the case when considering the development of localized deformation zones with alignment of insoluble minerals such as oxides **(Figs. 4-7)**. There are two types of explanations: (i) strain localization of insoluble minerals such as oxides may be associated with mass loss when all the soluble species are dissolved within a very narrow layer (as in some solution cleavage plane), leading to grain alignment at a small scale and sub-parallel foliation at a larger scale **(Figs. 4-7)**, or (ii) mechanical localization may also occur at scales smaller than the grain size. This last effect is more challenging to quantify in non-cohesive materials like gouge, but has been observed in high-deformation structures such as C-S structures (Powell, 1979). Both mechanisms of mass loss or strain localization lead to highly heterogeneous deformation with alternating parallel high and low γ domains, which might possibly be overprinted by sequences of earthquakes in fault zones. In order to test these effects, forward modeling of aggregate deformation including both mass and volume change Δ and high values of γ is proposed in the following sub-section.

3.4.2.2 Forward modeling of high strain and volume change in shear zones

This section investigates how calculated shear strain γ and volume variation Δ are influenced by the statistical properties of the variables θ' and α' measured in the field (**Eqs. 8 , 9**), and how these variables are correlated. α' is the deformed angle of a line with an initial angle of α with respect to the shear direction and θ' is the angle between the principal extension axis and the shear direction (**Fig. 2a**). The aim of this forward model is to develop a technique for measuring large strain values based on grain orientation in natural samples, by knowing the average $\langle\alpha'\rangle$ and the standard deviation σ' of the probability density functions of the final strain values, without knowing the initial state of strain, which is a common issue in natural field measurements.

The model is described in detail in the annex **A2**. **Figure 10a** shows the shearing of a set of random vectors with $\gamma = 5, 10, 100$ and with $\Delta = +0.5, 0, -0.5$, as well as their Rose diagrams with the calculated values of $\langle\alpha'\rangle$ and σ' after applying **Eq. 5**. **Figure 10b** shows the initial state of $\langle\alpha\rangle$ and σ (upper plots) transformed into the final state $\langle\alpha'\rangle$, and σ' (lower plots). The results are presented as surfaces in the range $0 < \gamma < 100$, and $-1 < \Delta < 1$. The deformed state is shown with iso-contours of $\langle\alpha'\rangle$ and σ'. By knowing the value of Δ, γ can be determined and vice versa. Note that both values of $\langle\alpha'\rangle$ and σ' decay rapidly for $\gamma > 10$ for any Δ (**Fig. 10b**).

An example of natural deformation is shown in the curves of **Fig. 10b**. It is based on the fit by a normal probability density function of the distribution of the orientation of clusters of grains, that are parallel to the cleavage, at small angles with the shear zone

(85°>Θ>95°, with <α'> = 0.3° and σ'= 2.5° in **Fig. 7f**). Iso-contours of $\langle \alpha' \rangle$ and σ' corresponding to this example are drawn in the Δ versus γ diagrams (red and green lines, respectively, at bottom part of **Fig. 10b**). These diagrams may be used to calculate the shear strain γ this value being highly dependent on the amount of volume change Δ. When using the iso-angle curves $\langle \alpha' \rangle = 0.3°$ (in red, **Fig. 10b**), the shear strain ranges from 190 with $\Delta = 0$ up to 100 when $\Delta = -0.44$ (corresponding to the volume change as calculated at decimetric scale in the Mülayim site**, (Fig. 7).** This is consistent with the use of **Eq. 9** from which we found $\gamma = 106$ with the same α' and Δ values. It was not possible to evaluate the volume change at smaller scales in this sample owing to the lack of an undeformed reference area**.** However, for other samples at all scales (micrometer to decimeter), values of Δ for the most deformed samples range between -0.16 and -0.66 **(Fig. 9)**. The value of $\Delta = -0.44$ is therefore considered to be a conservative value. Consequently, we take $\gamma = 100$ as a conservative shear strain value for zones with cleavage sub-parallel to the shear zone. It must be noted that the use of iso-angle curve $\sigma' = 2.5°$ gives $\gamma = 3$, which is clearly not consistent with the preceding result using $\alpha' = 0.3°$ and **Eq. 9**. The reason is that the measured value of σ' is too high compared to the theoretical value associated with $\gamma = 100$. This could be because σ' measurement is scale-dependent and that the scale of the localized deformation is smaller then the size of the grains (see discussion in the annex).

From this modeling procedure the coexistence of two ranges of shear strain values at the same location may be explained if the whole creeping zone is composed of parallel deformation zones with contrasting strain values: (i) shear zones with cleavage oblique to the shear zone in which the classical Fry method may be used and gives reliable results, and (ii) shear zones where cleavages are sub-parallel to the shear zones with sub-grain shear localization in which the Fry method cannot be used, and for which measuring the angle of cleavage with the shear zone is a more efficient method for measuring total volume change and shear strain. These intensely deformed zones include gouges but also some parts of the damage zones that contain cleavage planes sub-parallel to the shear zone **(Fig. 8**), as discussed above in the case of the Gerede outcrop. The model provides evidence of the coexistence of these two types of grain cluster orientation distribution (**Fig. 7f**): one with a large spectrum of angles with respect to the shear zone and high standard deviation values, as is the case for relatively low shear strain values, and another with very low angles of cleavage with respect to the shear zone and very low standard deviation values, as is the case for high shear strain. So, in order to evaluate the total displacement of the creeping zone, these two types of deformation zones must be integrated (see section **4.3**, and schematic drawing **Fig. 11g**).

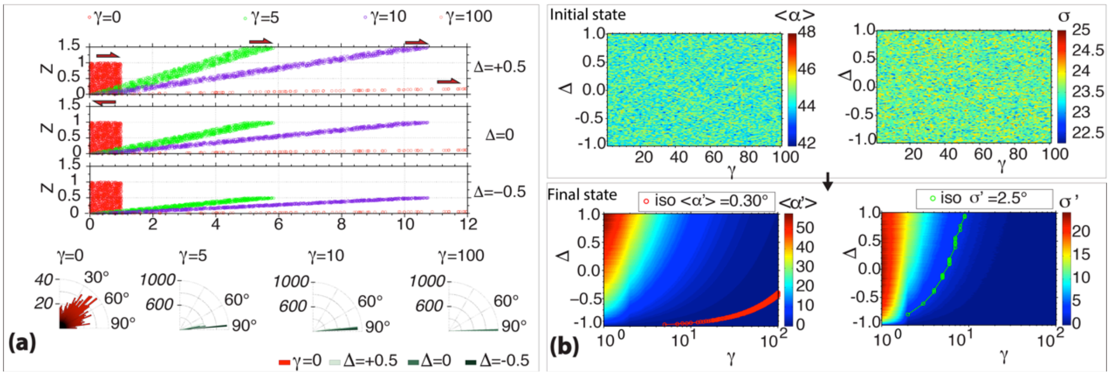

Figure 10. Forward modeling of shear zone with volume change and high shear strain values. (a) Set of random points (x, y) in the interval $0<x, y<1$ deformed by simple shear γ followed by volume change Δ. (b) Top (from left to right): initial states (before deformation) of $\langle\alpha\rangle$ and σ are represented as homogeneous random white noise and each point on these surfaces deforms with a given γ and Δ into a final state. Bottom (from left to right): final state (after deformation) of $\langle\alpha'\rangle$ and σ' (color bars have units in degree). Both $\langle\alpha'\rangle$ and σ' decrease with increasing γ and Δ, with iso-angle contours. A natural example is plotted on these diagrams corresponding to **Fig. 7f,** with iso-angle curves <α'> = 0.3° (in red) and σ'= 2.5° (in green).

3.4.3 Calculation of the aseismic part of the total displacement along locked and creeping sections of the North Anatolian Fault

In this section, the relative contribution of aseismic displacement in the total cumulative displacement, along locked and creeping sections of the North Anatolian Fault, is estimated. At the continental scale, rocks deform both by reversible deformation (elastic tectonic loading) and by irreversible deformation (ductile or brittle) that involves plastic dissipative processes and that depends on the system size (Karmakar et al., 2010). The use of a combination of geodetic and geological data is proposed in order to evaluate the width of the creeping zone, then combined with strain measurements at the outcrop scale to estimate the aseismic part of the total displacement on the fault (Ramsay, 1980) **(Eq. 10)**.

3.4.3.1 Modeling creep behavior during present days

Geodetic data used in this section are horizontal surface velocity maps across the North Anatolian Fault from the InSAR analysis of Cetin et al. (2014). These maps are calculated from Envisat satellite data acquired between 2003 and 2010. Horizontal velocity profiles perpendicular to the fault were extracted from these maps and modeled using:

$$V(z) = \frac{S}{\pi} arctan\left(\frac{z}{d_1}\right) + C\left(\frac{1}{\pi} arctan\left(\frac{z}{d_2}\right) - H(z)\right) \qquad (15)$$

where V is the surface, horizontal velocity along profile, S is the tectonic loading rate below a locking depth d_1, C is the creep rate from the surface down to a depth d_2, z is the distance perpendicular to the fault, and H is the Heaviside function (Hussain et al., 2016). The corresponding shear strain rate $\dot{\varepsilon}_{xz}$ along the profile is the spatial derivative of the velocity profile:

$$\dot{\varepsilon}_{xz} = \frac{\partial V(z)}{\partial z} = \frac{S}{\pi} \cdot \frac{d_1}{d_1^2+z^2} + C\left(\frac{1}{\pi} \cdot \frac{d_2}{d_2^2+z^2} - \delta(z)\right) \qquad (16)$$

where x is the axis along fault (see coordinate system in **Fig. 2d**).

Figure 11 a-b shows theoretical surface velocity profiles expected across a fault that : i) slides at a rate of 20 mm/yr below 15 km (tectonic loading) and is locked above, ii) creeps between the surface and a depth of 2 km at a rate of 10 mm/yr and is locked below between 2 km and 15 km, iii) combines both slip processes. The corresponding theoretical strain rate profiles are also derived **Fig. 11c**. **Figures 11d-e** show two horizontal velocity profiles derived from Cetin et al. (2014), perpendicular to the fault (30 km-wide and 240 km-long), and intersecting it at two sampling sites in creeping zones: Ismetpasa and Hamamli. Data are corrected from the tectonic loading at depth, assumed to be 20 mm/yr below 15 km, so that the profiles correspond only to the shallow creep signal. Superimposed on these profiles are forward models derived from the fault creep model of Cetin et al. (2014) (black lines on **Fig. 11d-e** are computed from the right-hand term of **Eq.15** considering only shallow creep). The creep rate is considered to be uniform from the surface to a given depth (10 mm/yr down to 2 km depth). The tectonic loading rate being about 25 mm/yr in average for the entire North Anatolian Fault (Reilinger et al., 2006; Cetin et al., 2014) and 20 mm/yr near Ismetpasa (Cetin et al., 2014), the shallow creep at present days accommodates about 40-50% of the tectonic loading.

These forward models on **Fig. 11d-e** are derived to obtain shear strain rate profiles **(Fig. 11f**) at the sampling sites in order to:

1) Evaluate the relevance of a two normal distributions model we derived from the geological observations. This model suggest that the entire shear creep displacement is partitioned into two types of shear deformation bands: wide shear zones with cleavage oblique to the fault zone (damage zone in the present days), and narrow shear zones with cleavage sub-parallel to the fault zone (gouge in the present days), as shown schematically in **Fig. 11g**.

2) Calculate the width of the wide shear zone in the past assuming that it keeps the same width all along the deformation process.

We thus propose to fit the geodetic strain rate model of **Fig. 11f** (green curve) at Ismetpasa and Hamamli with a superposition of two normal distributions representing the cumulative width and shear strain associated with both types of shear zones (e.g. damage and gouge zones). The shear components can be approximated with normal distributions $\gamma \sim N(0, \sigma^2)$ so that:

$$\gamma(z) = \sum_k \gamma_{0,k} \cdot e^{-z^2/2\sigma_k^2} \quad (17)$$

where γ is the shear strain, and index k refers to the type of shear zone. The width of the shear zone is considered to be $W_k = 2\sigma_k$. Postulating that the shear strain is the only time dependent variable $\gamma(t)$, the shear strain rate $\dot{\gamma}$ obtained by deriving **Eq. 17** over time is $\dot{\gamma}(z) = \sum_k \dot{\gamma}_{0,k} \cdot e^{-z^2/2\sigma_k^2}$.

Considering that strain rate and width values are independent for the damage zone and the gouge zone, we first invert the strain rate and width of the damage zone: $\dot{\gamma}_d = 1.6 \cdot 10^{-6} yr^{-1}$, and W_d = 4.4 km, respectively (**Fig. 11f,** orange normal distribution). This value of several kilometers for the width of the damage zone is consistent with the kilometer scale fault zones width observed in the field (**Fig. 8b**). The low resolution (pixel size 20 m east-west, 4 m north-south) and high noise level (**Fig. 11d-e**) of InSAR satellite data do not allow to provide a strain rate model in the fault near field that is precise enough to properly estimate the width of the gouge zone. We thus fix this width to W_g=1 m based on field measurements from Kaduri et al. (2017). The strain rate of the gouge zone is finally estimated as follow. The cumulated displacement rate along a fault, $\dot{D}$, is given by the integration of the two normal distributions over a z-axis perpendicular to the fault plane, in a range $(-\infty, +\infty)$ (placing **Eq. 17** in **Eq. 10**):

$$\dot{D} = \dot{\gamma}_g \cdot \int_{-\infty}^{\infty} e^{-z^2/2\sigma_g^2} dz + \dot{\gamma}_d \cdot \int_{-\infty}^{\infty} e^{-z^2/2\sigma_d^2} dz$$

$$= \dot{\gamma}_g \cdot \sigma_g \cdot \sqrt{2\pi} + \dot{\gamma}_d \cdot \sigma_d \cdot \sqrt{2\pi} \qquad (18)$$

Assuming that $\dot{D}$ is 10 mm/yr based on the InSAR analysis of Cetin et al., 2014), **(Fig. 11b-c)**, and given the values of $\dot{\gamma}_d$ and W_d obtained above, we estimate that $\dot{\gamma}_g = 0.89 \cdot 10^{-3}\ yr^{-1}$ from **Eq. 18,** with $W_k = 2\sigma_k$. It is worth noting that this partition of the displacement rate between damage zone and gouge is strongly dependent on the width of the gouge we imposed, and significant improvements on the detail of this partition would rely on a better spatial definition of the present days geodetic measurements. However, our formalism allows representing in a consistent framework both structural geology and geodesy data, which have different spatial and temporal scales.

3.4.3.2 Modeling the creeping behavior in the past since the beginning of the fault sliding

Two types of strain distributions must be taken into account when calculating the displacement associated with creep processes since the beginning of the fault sliding (**Fig. 11g**): (i) a distribution that represents the low strain and wide shear zones with cleavage oblique to the fault zone, with γ_{wsz} and W_{wsz} as shear strain and width characteristics, respectively, and (ii) a distribution that represents the high strain and narrow shear zones with cleavage sub-parallel to the fault zone, with γ_{nsz} and W_{nsz} as shear strain and width characteristics. Geodetic data allows evaluating the width of the wide shear zone W_{wsz} to be 4.4 km (**Fig. 11f**). The strain measurements on field samples (**Fig. 9**) give a shear strain value $\gamma_{wsz} = 2$ (when including the volume change) that is considered here as the maximum value of γ for the wide shear zone. For the narrow shear zones, geological data give complementary information. A conservative shear strain γ_{nsz}= 100 has been evaluated from the forward modeling of such shear zones with volume change (see **§4.2.2)**. In addition, the width ratio between the high strain and narrow shear zones with cleavage sub-parallel to the fault zone (W_{nsz}) and the low strain and wide shear zones with cleavage oblique to the fault zone (W_{wsz}) has been estimated at regional scale in the Gerede quarry to be about 0.04 **(Fig. 8).** Consequently, considering a width of the wide shear zone between 1 km and 4.4 km, the width of the narrow zones can vary from 0.04 x 1000 = 40 m to 0.04 x

4400 = 176 m. All these strain and width values allows to evaluate bounds on the total displacement associated with aseismic creep, by integrating the shear strain values of the two normal distributions across the fault. The maximum and minimum aseismic displacement is calculated using **Eq. 18** with γ instead of $\dot{\gamma}$. The maximum displacement results from the combination of the maximum displacement associated with the low strain and wide shear zone (using the maximum values $\gamma_{wsz} = 2$ and W_{wsz} = 4.4 km, equivalent to σ_{wsz}=2.2 km), which is 11 km, and of the maximum displacement associated with the high strain and narrow shear zone (maximum values $\gamma_{nsz} = 100$ and W_{nsz} =176m, equivalent to σ_{wsz}= 88m), which is 22 km, leading to a total maximum displacement of 33 km. Similarly, the minimum displacement is estimated using the minimum values of γ_{wsz} and W_{wsz} for the low strain and wide shear zone ($\gamma_{wsz} = 2$; W_{wsz} = 1 km), giving 2.5 km of displacement, and the minimum values of γ_{nsz} and W_{nsz} for the high strain and narrow shear zone ($\gamma_{nsz} = 100$; W_{nsz} = 40 m), giving 5 km of displacement, leading to a total minimum displacement of 7.5 km. The estimated total aseismic displacement thus ranges between 41% and 9%, or 25±16%, of the total displacement of 80 km during geological times.

Finally, the behavior of the locked zones in the past was also modeled, using the Taskesti outcrop in limestone as representative of such zones. From geological observations of this outcrop **(Fig. 3)**, the width of the narrow shear zone W_{nsz} is estimated to 1 m with an associated shear strain γ_{nsz} of 0.5, using the maximum contraction of the stylolites $\sqrt{\lambda_2} = 0.8$. The width of the wide shear zone W_{wsz} may be estimated to be about 10 m that represents the maximum width in which we observe tectonic stylolites. The associated γ_{wsz} may be deduced from a calculation of post-seismic creep rate that has been done in a previous study (Kaduri et al., 2017), for which the creep rate ratio between narrow and wide shear zones was estimated to be about 100. We use this value here to evaluate a $\gamma_{\mathrm{wsz}} = 0.005$. The corresponding total aseismic displacement for the locked zones is thus estimated to be less than 1.5 m (total aseismic displacement for the narrow and wide shear zones cumulated) or 0.002% of the total displacement of the North Anatolian Fault. This indicates that the displacement accommodated by creep in limestone is almost negligible.

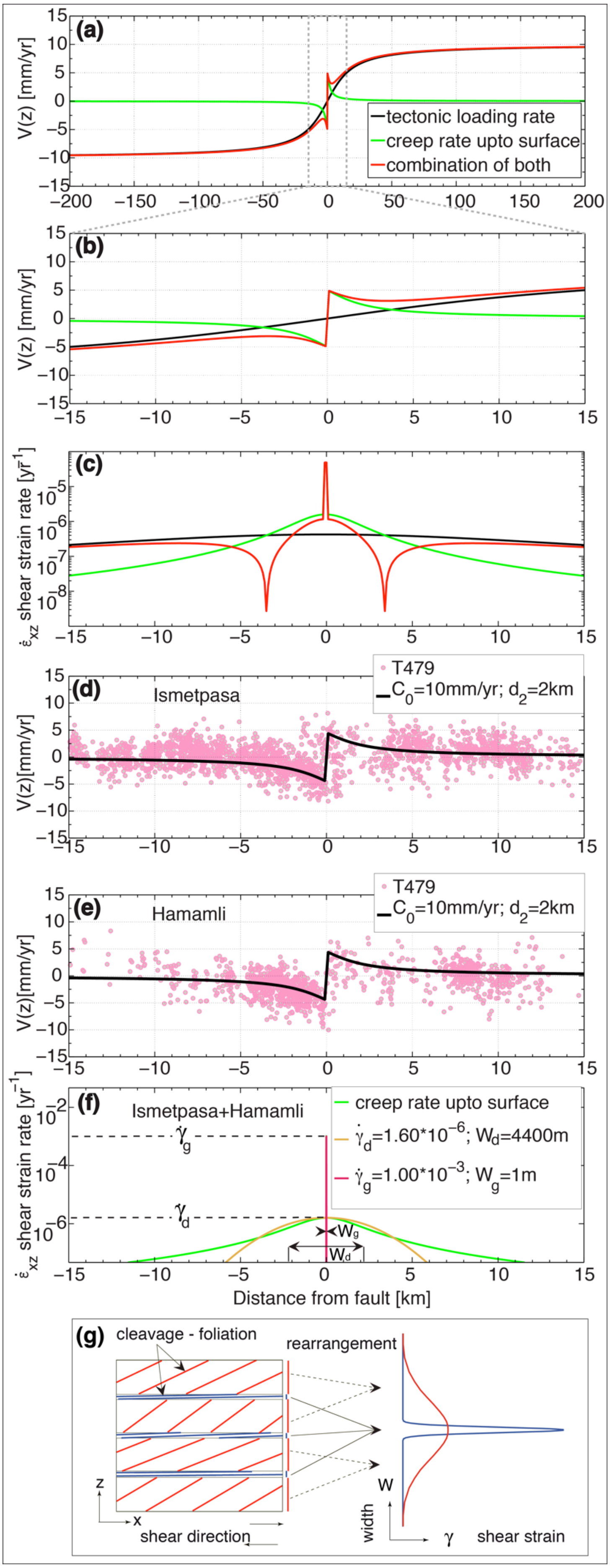
(a)
V(z) [mm/yr]
tectonic loading rate
creep rate upto surface
combination of both
(b)
V(z) [mm/yr]
(c)
$\dot{\varepsilon}_{xz}$ shear strain rate [yr^{-1}]
(d)
Ismetpasa
V(z)[mm/yr]
T479
C_0=10mm/yr; d_2=2km
(e)
Hamamli
V(z)[mm/yr]
T479
C_0=10mm/yr; d_2=2km
(f)
Ismetpasa+Hamamli
$\dot{\varepsilon}_{xz}$ shear strain rate [yr^{-1}]
creep rate upto surface
$\dot{\gamma}_d$=1.60*10^{-6}; W$_d$=4400m
$\dot{\gamma}_g$=1.00*10^{-3}; W$_g$=1m
$\dot{\gamma}_g$
$\dot{\gamma}_d$
W$_g$
W$_d$
Distance from fault [km]
(g)
cleavage - foliation
rearrangement
z
x
shear direction
W
width
γ
shear strain

Figure 11. Aseismic strain along the North Anatolian Fault. (a) Horizontal surface velocity as a function of distance from fault (black profile is for a fault locked at the surface and creeping at depth, green profile is for a fault creeping at the surface and locked at depth, red profile is the combination of both). (b) Zoom on (a). (c) Surface strain rate as a function of distance from fault, derived from (b). (d) & (e) Geodetic horizontal creep rate profiles perpendicular to the North Anatolian Fault across Ismetpasa and Hamamli outcrops, respectively; the data (dots) and model (black lines) are taken from Cetin et al. (2014). (f) Strain rate profiles derived from creep rate models in (d) & (e). These profiles are fitted with the superposition of two normal distributions to model the shear strains and the widths of the gouge and the damage zones for Ismetpasa-Hamamli outcrops. (g) Schematic representation of the strain distribution in the creeping zone, which is made up of parallel zones of various strain values that are represented by two normal distributions of the shear strain.

3.5 Conclusion

The quantitative evaluation of the aseismic part of the total displacement along the North Anatolian Fault provides rheological and methodological insights on creep mechanisms and strain measurements.

- In the early stages of the deformation, solution cleavage operates in an open system with the departure of soluble species within the whole creeping zone. Then pressure solution operates at grain boundary sliding scale in a closed system when the grain size decreases and when soluble minerals are partially removed. At a later stage the deformation process evolved to a mixed diffusive and friction controlled sliding. An end member mechanism involves sliding friction when the soluble minerals have been completely removed or can no longer be dissolved in gouges. In parallel in damage zones, early creeping zones are progressively strengthened by the multiples sealed fractures associated with inflow of carbonates linked to earthquakes that affected the fault zones.
- From a methodological point of view, we show that the measurement of finite strain in shear zones, which can reach very large strain values, is strongly dependent on the methodology. Methods based on the analysis of particles distribution, such as the Fry method, do not allow evaluating strain ratio higher than 8 and consequently shear strain higher than about 2. Conversely, using the evolution of cleavage angle with the shear zone allows measuring very large strain values up to 100 or more. However, in both cases, evaluation of the mass and volume change is crucial and must be integrated in the calculation.
- A forward modeling procedure was developed to simulate high shear strain γ coupled to volume change Δ. It shows that both the shear angle and its standard

deviation drastically decrease with increasing shear strain. Observed natural deformation can only be explained if creep zones are partitioned into parallel deformation zones with contrasting shear strain characteristics: (i) wide shear zones with cleavage oblique to the shear zone in which the Fry method may be used and gives reliable results and (ii) narrow shear zones with cleavage planes sub-parallel to the shear zones, with sub-grain shear localization in which measuring the angle of the cleavage with the shear zone is a more efficient method of evaluating the shear strain values.

- Finally, finite shear strain characteristics evaluated from geological analyses were used in parallel with geodetic data in order to calculate the total cumulated aseismic displacement that has been accommodated by creep. Modeling the creep behavior during the present days allows validating the model of the two types of shear zones and evaluating the maximum width of the creeping zone. Modeling the creeping behavior since the beginning of the fault sliding allows calculating an aseismic part of the total 80km displacement of 25±16% in the creeping (volcanic) zone and 0.002% in the locked (limestone) zones, showing the crucial effect of the lithology in the seismic versus aseismic partition.

Acknowledgements: This project was funded by the European Union's, Seventh Framework Programme for research technological development and demonstration under grant agreement no. 316889 (ITN FlowTrans) and by the Norwegian Research Council grant n° 250661 'HADES' to FR. The authors thank Nathaniel Findling, Valerie Magnin and Valentina Batanova for technical support with sample preparation and XRD and EPMA analytical measurements at ISTerre.

References

Ashby, M., Verrall, R., 1973. Diffusion-accommodated flow and superplasticity, Acta Metall. 11(2), 149-163.

Armijo, R., Meyer, B., Hubert, A., Barka, A., 1999. Westward propagation of the North Anatolian fault into the northern Aegean: Timing and kinematics. Geology 27, 267-270. doi:10.1130/0091-7613.

Armijo, R., Meyer, B., Hubert, A., Barka, A., 2000. Westward propagation of North Anatolian fault into the northern Aegean:Timing and kinematics: Comment and Reply, Geology, 28(2), 188, doi:10.1130/0091-7613.

Bilham, R., Ozener, H., Mencin, D., Dogru, A., Ergintav, S., Çakir,Z., Aytun, A., Aktug., B., Yılmaz, O., Johnson, W., Mattioli, G.S., 2016. Surface creep on the North Anatolian Fault at Ismetpasa, Turkey, 1944 ‑ 2016, J. Geophys. Res. Solid

Earth, 121, 7409-7431.

Bos, B., Spiers, C. J., 2002. Frictional-viscous flow of phyllosilicate-bearing fault rock: Microphysical model and implications for crustal strength profiles. J. Geophys. Res. 107, doi:10.1029/2001JB000301.

Bos, B., Spiers, C. J., 2000. Effect of phyllosilicates on fluid-assisted healing of gouge-bearing faults, Earth Planet. Sci. Lett., 184(1), 199–210, doi:10.1016/S0012-821X(00)00304-6.

Çakir, Z., Akoglu, A.M., Belabbes, S., Ergintav, S., Meghraoui, M., 2005. Creeping along the Ismetpasa section of the North Anatolian fault (Western Turkey): Rate and extent from InSAR. Earth Planet. Sci. Lett. 238, 225–234. doi:10.1016/j.epsl.2005.06.044.

Çakir, Z., Ergintav, S., Akoğlu, A.M., Çakmak, R., Tatar, O., Meghraoui, M., 2014. InSAR velocity field across the North Anatolian Fault (eastern Turkey): Implications for the loading and release of interseismic strain accumulation. J. Geophys. Res. Solid Earth 119, 7934–7943. doi:10.1002/2014JB011360.

Carpenter, B.M., Ikari, M.J., Marone, C., 2016. Laboratory observations of time-dependent frictional strengthening and stress relaxation in natural and synthetic fault gouges. J. Geophys. Res. Solid Earth 121, 1183-1201, doi:10.1002/2015JB012136.

Cetin, E., Çakir, Z., Meghraoui, M., Ergintav, S., Akoglu, A.M., 2014. Extent and distribution of aseismic slip on the Ismetpa?a segment of the North Anatolian Fault (Turkey) from Persistent Scatterer InSAR. Geochemistry, Geophys. Geosystems 15, 2883–2894. doi:10.1002/2014GC005307.

Chen, K.H., Bürgmann, R., 2017. Creeping faults: Good news, bad news? Rev. Geophys. 55(2), 282-286. doi:10.1002/2017RG000565.

Cloos, E., 1947. Oolite deformation in South Mountain Fold Maryland Geol. Soc. Am. Bull. 58, 843-917.

Collettini, C., Niemeijer, A., Viti, C., Marone, C., 2009. Fault zone fabric and fault weakness, Nature, 462(7275), 907–910, doi:10.1038/nature08585.

Emre, Ö., Duman, T.Y., Özalp, S., Elmacı, H., Olgun, Ş., Şaroğlu, F., 2013. Active Fault Map of Turkey with an Explanatory Text. 1:1,250,000 Scale. General Directorate of Mineral Research and Exploration (MTA), Ankara-Turkey.

Emre, O., Duman, T.Y., Ozalp, S., Saroglu, F., Olgun, S., Elmaci, H., Can, T., 2016. Active fault database of Turkey. Bull. Earthq. Eng. 1–47. doi:10.1007/s10518-016-0041-2.

Erslev, E., 1988. Normalized center-to-center strain analysis of packed aggregates. J. Struct. Geol. 10, 201–209. doi:10.1016/0191-8141(88)90117-4.

Erslev, E., Ge, H., 1990. Least-squares center-to-center and mean object ellipse fabric analysis. J. Struct. Geol. 12, 1047–1059. doi:10.1016/0191-8141(90)90100-D.

Fossen, H., Tikoff, B., 1993. The deformation matrix for simultaneous simple shearing, pure shearing and volume change, and its application to transpression-transtension tectonics. J. Struct. Geol. doi:10.1016/0191-8141(93)90137-Y.

Fossen, H., Cavalcante, G.C.G., 2017. Shear zones – A review. Earth-Science Rev., 171, 434-455, doi:10.1016/j.earscirev.2017.05.002.

Fry, N., 1979. Random point distributions and strain measurement in rocks. Tectonophysics, 60, 89–105. doi:10.1016/0040-1951(79)90135-5.

Genier, F., Epard, J.L., 2007. The Fry method applied to an augen orthogneiss: Problems and results. J. Struct. Geol. 29, 209–224. doi:10.1016/j.jsg.2006.08.008.

Gratier, J., Dysthe, D.K., Renard, F., 2013. The role of pressure solution creep in the ductility of the Earth ' s upper crust, Advances in Geophysics. 54, 47-179, doi:10.1016/B978-0-12-380940-7.00002-0.

Gratier, J.P., Richard, J., Renard, F., Mittempergher, S., Doan, M.L., Di Toro, G., Hadizadeh, J., Boullier, a. M., 2011. Aseismic sliding of active faults by pressure solution creep: Evidence from the San Andreas Fault Observatory at Depth. Geology 39, 1131–1134. doi:10.1130/G32073.1.

Gratier, J.-P., Noiriel, C., Renard, F., 2015. Experimental evidence for rock layering development by pressure solution, Geology, 43(10), 871–874, doi:10.1130/G36713.1.

Graymer, R.W., Ponce, D.A., Phelps, G.A., Wentworth, C.M., 2005. Three-dimensional geologic map of the Hayward fault, northern California : Correlation of rock units with variations in seismicity, creep rate, and fault dip, Geology, 33, 521–524. doi:10.1130/G21435.1.

Harris, R.A., 2017. Large earthquakes and creeping faults. Rev. Geophys. 55, 169–198. doi:10.1002/2016RG000539.

Heilbronner, R., 2002. Analysis of bulk fabrics and microstructure variations using tesselations of autocorrelation functions. Comput. Geosci. 28, 447–455. doi:10.1016/S0098-3004(01)00088-7

Heilbronner, R., Barrett, S., 2014. Image Analysis in Earth Sciences Microstructures and Textures of Earth Materials, Springer Science and Business Media, Berlin.

Hull, J., 1988. Thickness-displacement relationships for deformation zones 10, 431–435. doi:10.1016/0191-8141(88)90020-X

Hussain, E., Hooper, A., Wright, T.J., Walters, R.J., Bekaert, D.P.S., 2016. Interseismic strain accumulation across the central North Anatolian Fault from iteratively unwrapped InSAR measurements. J. Geophys. Res. Solid Earth 121, 9000–9019. doi:10.1002/2016JB013108

Imber, J., Holdsworth, R.E., Butler, C.A., Strachan, R.A., 2001. A reppraisal of the Sibson-Scholz fault model: the nature of the frictionnal to viscous (brittle-ductile) transition along a long-lived crustal-scale fault, Outer Hebrides, Scotland, Tectonics 20, 601-624.

Janssen, C., Michel, G.W., Bau, M., Lüders, V., and Mühle K., 1997. The North Anatolian Fault Zone and the Role of Fluids in Seismogenic Deformation, J. Geol., 105(3), 387–404, doi:10.1086/515934.

Jefferies, S.P., Holdsworth, R.E., Wibberley, C.A.J., Shimamoto, T., Spiers, C.J., Niemeijer, A.R., Lloyd, G.E., 2006. The nature and importance of phyllonite development in crustal-scale fault cores: an example from the Median Tectonic Line, Japan, Journal of Structural Geology, 28, 220-235.

Kaduri, M., Gratier, J.-P., Renard, F., Çakir, Z., Lasserre, C., 2017. The implications of fault zone transformation on aseismic creep: Example of the North Anatolian Fault, Turkey. J. Geophys. Res. Solid Earth., 122, 4208–4236, doi:10.1002/2016JB013803

Kaneko, Y., Fialko, Y., Sandwell, D.T., Tong, X., Furuya, M., 2013. Interseismic deformation and creep along the central section of the North Anatolian Fault (Turkey): InSAR observations and implications for rate-and-state friction properties. J. Geophys. Res. Solid Earth 118, 316–331. doi:10.1029/2012JB009661

Karmakar, S., Lemaître, A., Lerner, E., Procaccia, I., 2010. Predicting Plastic Flow Events in Athermal Shear-Strained Amorphous Solids. Phys. Rev. Lett. 104, 215502. doi:10.1103/PhysRevLett.104.215502

Lockner, D., Morrow, C., Moore, D., Hickman, S., 2011. Low strength of deep San

Andreas fault gouge from SAFOD core. Nature 472, 82–85. doi:10.1038/nature09927

Mavko, G.M., 1981. Mechanics of Motion on Major Faults. Annu. Rev. Earth Planet. Sci. 9, 81–111. doi:10.1146/annurev.ea.09.050181.000501

Okada, Y., 1985. Surface deformation due to shear and tensile faults in a half-space. Bulletin of the seismological society of America, 75(4), 1135-1154.

Pennacchioni, G., 2005. Control of the geometry of precursor brittle structures on the type of ductile shear zone in the Adamello tonalites, Southern Alps (Italy) 27, 627–644. doi:10.1016/j.jsg.2004.11.008.

van der Pluijm, B.A., Marshak, S., 2010. Earth Structures: An Introduction to Structural Geology and Tectonics, 2nd Edition. W.W. Norton Company, New York.

Powell, C.M., 1979. A morphological classification of rock cleavage. Tectonophysics 58, 21–34. doi:10.1016/0040-1951(79)90320-2

Ramsay, J.G., 1980. Shear zone geometry: A review. J. Struct. Geol. 2, 83–99. doi:10.1016/0191-8141(80)90038-3

Ramsay, J.G., 1967. Folding and fracturing of rocks. McGraw-Hill, New York.

Ramsay, J.G., Graham, R.H., 1970. Strain variation in shear belts. Can. J. Earth Sci. 7, 786–813. doi:10.1139/e70-078

Reilinger, R. et al., 2006. GPS constraints on continental deformation in the Africa-Arabia-Eurasia continental collision zone and implications for the dynamics of plate interactions, J. Geophys. Res. Solid Earth, 111(5), 1–26, doi:10.1029/2005JB004051.

Renard, F., Dysthe, D.K., Feder, Bjørlykke, K., Jamtveit B., 2001. Enhanced pressure solution creep rates induced by clay particles: Experimental evidence in salt aggregates, Geophys. Res. Lett., 28(7), 1295–1298, doi:10.1029/2000GL012394.

Richard, J., Gratier, J.-P., Doan, M., Boullier, A., Renard, F., 2014. Rock and mineral transformations in a fault zone leading to permanent creep: Interactions between brittle and viscous mechanisms in the San Andreas Fault. J. Geophys. Res. Solid Earth 119, 8132–8153. doi:10.1002/2014JB011489

Rousset, B., Jolivet, R., Simons, M., Lasserre, C., Riel, B., Milillo, P., Çakir, Z., Renard, F., 2016. An aseismic slip transient on the North Anatolian Fault, Geophys. Res. Lett., 43(7), 3254–3262, doi:10.1002/2016GL068250.

Samuelson, J., Spiers, C.J., 2012. Fault friction and slip stability not affected by Co2 storage: Evidence from short-term laboratory experiments on North Sea reservoir sandstones and caprocks. Int. J. Greenh. Gas Control, 11, 78–90. doi:10.1016/j.ijggc.2012.09.018

Savage, J.C., Burford, R.O., 1973. Geodetic determination of relative plate motion in central California. J. Geophys. Res. 78, 832–845. doi:10.1029/JB078i005p00832

Scholz, C.H., 2002. The Mechanics of Earthquake Faulting, 2nd Edition. Cambridge University Press, Boston.

Şengör, A. M. C., O. Tuysuz, C. Imren, M. Sakinc, H. Eyidogan, N. Gorur, X. LePichon, and C. Rangin (2004), The North Anatolian fault: A new look, Annu. Rev. Earth Planet. Sci., 33, 1–75.

Sone, H., Shimamoto, T., Moore, D.E., 2012. Frictional properties of saponite-rich gouge from a serpentinite-bearing fault zone along the Gokasho-Arashima Tectonic Line, central Japan. J. Struct. Geol. 38, 172–182. doi:10.1016/j.jsg.2011.09.007

Stein, R.S., Barka, A., Dieterich, J.H., 1997. Progressive failure on the North Anatolian fault since 1939 by earthquake stress triggering. Geophys. J. Int. 128, 594–604. doi:10.1111/j.1365-246X.1997.tb05321.x

Stewart, M.A., Holdsworth, R.E., and Strachan, R.A., 2000. Deformation processes and weakening mechanisms within the frictional-viscous transition zone of major crustal faults: insights from the Great Glen Fault zone, Scotland, Journal of Structural Geology, 22, 543-560.

Thomas, M.Y., Avouac, J.-P., Gratier, J.-P., Lee, J.-C., 2014. Lithological control on the deformation mechanism and the mode of fault slip on the Longitudinal Valley Fault, Taiwan. Tectonophysics 632, 48–63. doi:10.1016/j.tecto.2014.05.038.

Vitale, S., Mazzoli, S., 2008. Heterogeneous shear zone evolution : The role of shear strain hardening / softening. J. Struct. Geol. 30, 1383–1395. doi:10.1016/j.jsg.2008.07.006.

Zubtsov, S., Renard, F., Gratier, J.P., Guiguet, R., Dysthe, D.K., Traskine, V., 2004. Experimental pressure solution compaction of synthetic halite/calcite aggregates. Tectonophysics 385, 45–57. doi:10.1016/j.tecto.2004.04.016.

3.6 Supplementary material

Appendix A1. Supplementary Information for the methods' section (§2): Numerical recipes and data processing

Measuring the extension of veins using image processing

The extension values marked by vein networks are calculated using a three-step procedure. For a given image (optical image of a thin section or microprobe image of minerals), the first step is to segment it from color to binary levels, where a blue level represents the rock matrix and a white level is a vein. The second step is to calculate the strain for each horizontal line for a given orientation of the image **(Fig. A1.a-c)**, the initial length being the sum of the spacing's between the veins and the final length being the total length. The mean strain value of each extension diagram is used for all possible orientations. In the third and last step, those mean strain values are plotted as a function of the rotational angle in polar coordinates, and a strain ellipse is fitted to the data **(Fig A1.d)**.

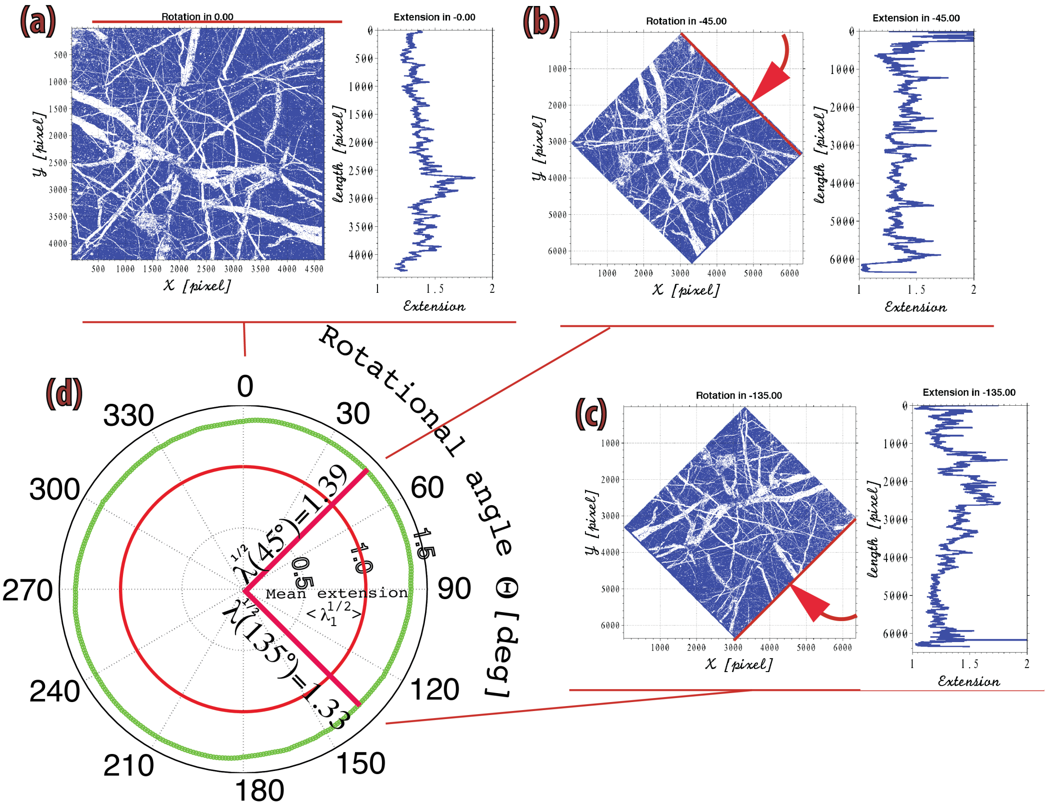

Figure A1. (a, b, c) Optical images of a thin section transformed into a binary image and representation of the extensional strain along the vertical axis for each angle of rotation. Host rock is in blue, veins are in white. (d) In polar coordinates the green ellipse is the mean extension as function of rotational angle and the unit circle is represented in red. Here, the deformation is almost isotropic, showing extension in all directions with a maximum at N45.

Measuring the construction of stylolite using image processing (§2)

Additional strain calculations were performed by measuring the maximum amplitude of the stylolite peaks and the number of stylolite for angle φ. These parameters are measured with a bin size of 5°. **Figure A2.** Shows the average maximum peak height $\langle Amp_{max}\rangle$ (top) and the number of stylolites $N_{Stylolite}$ (bottom) in direction φ. Those values plugged in **Eq. 12** in order to calculate $\sqrt{\lambda_2}_{stylolite}$before plotting in **Fig. 3d**.

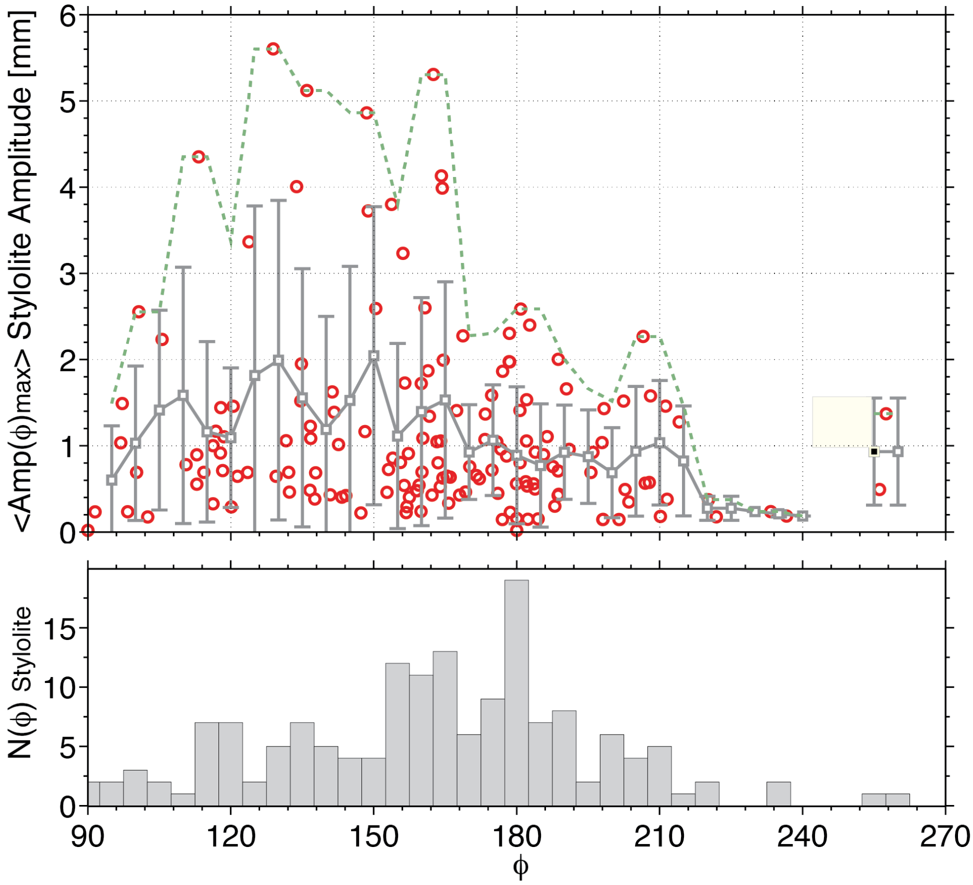

Figure A2. Top: the red circles are the maximum amplitude of each stylolite peaks, the gray line with the vertical bears corresponds to the average and standard deviation of the maximum amplitude of the stylolite peaks (with bin size of 5 degree) and the green dashed line is the maximum value. Bottom: a histogram of the number of stylolite as function of the orientation φ, those values were plugged in **Eq. 12** and presented in polar coordinates system in **Fig. 3d**.

Strain measurements using the Fry method and the normalized Fry method

The principle of the strain analysis using the classical Fry method (Fry, 1979), also called the center-to-center method, is based on the distribution between the centers of objects. The positions of these centers are systematically related to the finite strain ellipse and can be described easily with three objects. One considers here three circular grains with tetrahedral void **(Fig. A3a)**. In case of dissolution between two grains boundaries only, the distance is shortened in one direction and is slightly extended in the perpendicular direction **(Fig. A3b)**. If the center of each grain is located at the axis origin, and the other grain centers are plotted, the void between the points represent the strain ellipse. When deformation is equal to zero will obtain a circle **(Fig. A3c)**. When the deformation is not null one will obtain the strain ellipse **(Fig. A3d)**.

The normalized Fry method (Erslev, 1988) works in similar way to the classic Fry method when considering the grain size. The diagrams produced are unit-less. Maps of minerals are usually composed of several minerals with a wide range of grain sizes. Hence, this type of data requires considering grain size in the calculation in order to distinguish better the void prior to ellipse fitting. In this study, a similar algorithm is applied on the gains extracted from the map of minerals. The diagrams are produced for each mineral separately, and then all these diagrams are superposed into a single diagram. In this approach the normalized center-to-center distance between object with index i and object with index j, $\widehat{D}_{ij}$, is defined as the distance between the objects D_{ij} divided by the sum of their radii as follows **(Fig. A4a)**:

$$\widehat{D}_{ij} = \frac{D_{ij}}{r_i + r_j} \qquad \text{(A.1)}$$

where, the radius of an object with index i (or j) is: $r_i = \sqrt{r_{i,min}^2 + r_{i,max}^2}$ **(Fig. A4b)**. In addition, the calculation is performed for all objects with $i \neq j$.

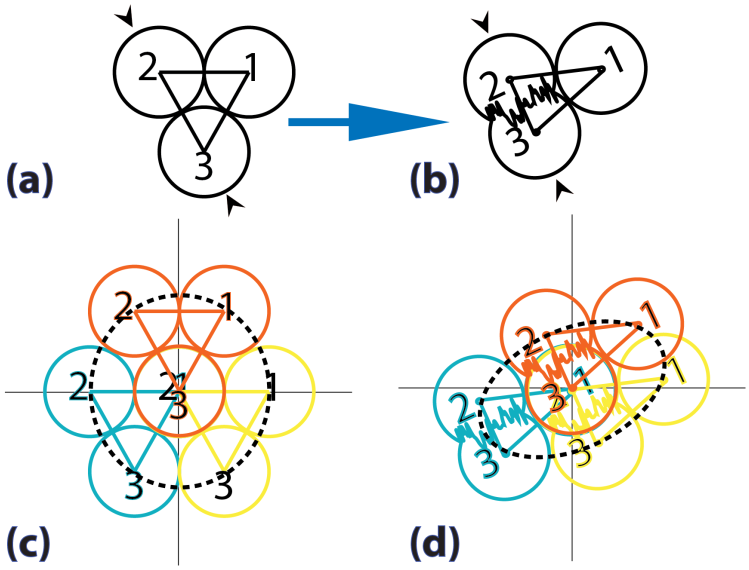

Figure A3. Sketch of Fry method (Fry, 1979),: (a) Three grains with a tetrahedral void represent a non-deform object (b) The three grains after dissolving one contact. (c) The Fry diagram of a non-deformed object leads to a circle (dashed line) (d) The Fry diagram of a deformed object leads to an ellipse of deformation (dashed line).

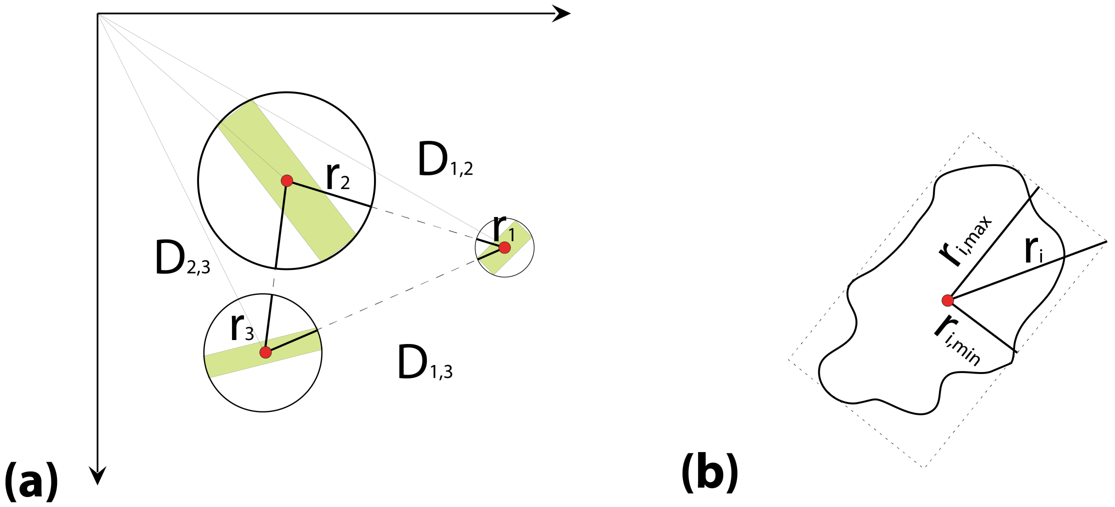

Figure A4. Sketch of the normalized Fry method (Erslev, 1988): (a) Three grains with different sizes and distances. (b) The vector diagram defines the radius of amorphous object.

Relative Mass change using mineralogical maps (EPMA)

The relative mass change estimates are based on mineralogical maps from the protected and exposed zones in the rock **(Fig. 2f and Eq. 14)**, which were calculated from WDS-EPMA maps of elements. In the map of elements, some holes are filled with epoxy glue such that:

$$\sum_{i=1}^{n} a_i + epoxy = 100\%, \qquad \text{(A.2)}$$

where, a_i- is the surface area fraction of mineral i. Therefore, it is necessary to exclude the epoxy glue surface area from the measurements and renormalize the minerals assemblage so that the total is equal to 100%, as follows

$$100 \cdot \sum_{i=1}^{n} a_i / \sum_{i=1}^{n} a_i = 100\% \qquad \text{(A.3)}$$

Then, the mineral content is separated into mobile (soluble) and immobile (insoluble) minerals, and the calculations of I_p (protected zones) and I_e (exposed zones) are made by the addition of all soluble and insoluble minerals surface fractions.

Algorithm for processing mineralogical data

This algorithm receives as an input the maps of elements acquired with EPMA-WDS (or from XRF). These data are converted into strain and relative mass change as an output. In this work, all strain analysis as well as geometrical properties and minerals content measurement are performed using image processing techniques for which several Matlab codes were written. Some of steps are fully or semi automatized according to the following algorithm **(Fig. A5a)**:

Step-1: Convert EMPA-WDS (or XRF) maps of elements **(Fig. A5b)** into map of minerals **(Fig. A5c)**. This step was made using XmapTools or by threshold the oxide content intensity map of each element and superimpose them together into map of minerals. The minerals were detected using both a mineral list composition from XRD analysis, and oxide content from automatic calculation with EMPA-WDS.

Step-2: Separate between soluble and insoluble minerals and calculate the relative mass change between protected and exposed zones.

Step-3: Extract geometrical data (as described in **§2.5.2** and **Fig. 2g)** from binary image of each mineral **(Fig. A5d)**.

Step-4: For each phase, plot the Rose diagrams of grain orientations and the Fry diagram **(Fig. A5e)**.

Step-5: Use **Eq. 8 & 9** and plot this data on a $R - \Delta$ diagram (e.g. **Fig. 8)** in order to calculate the strain γ.

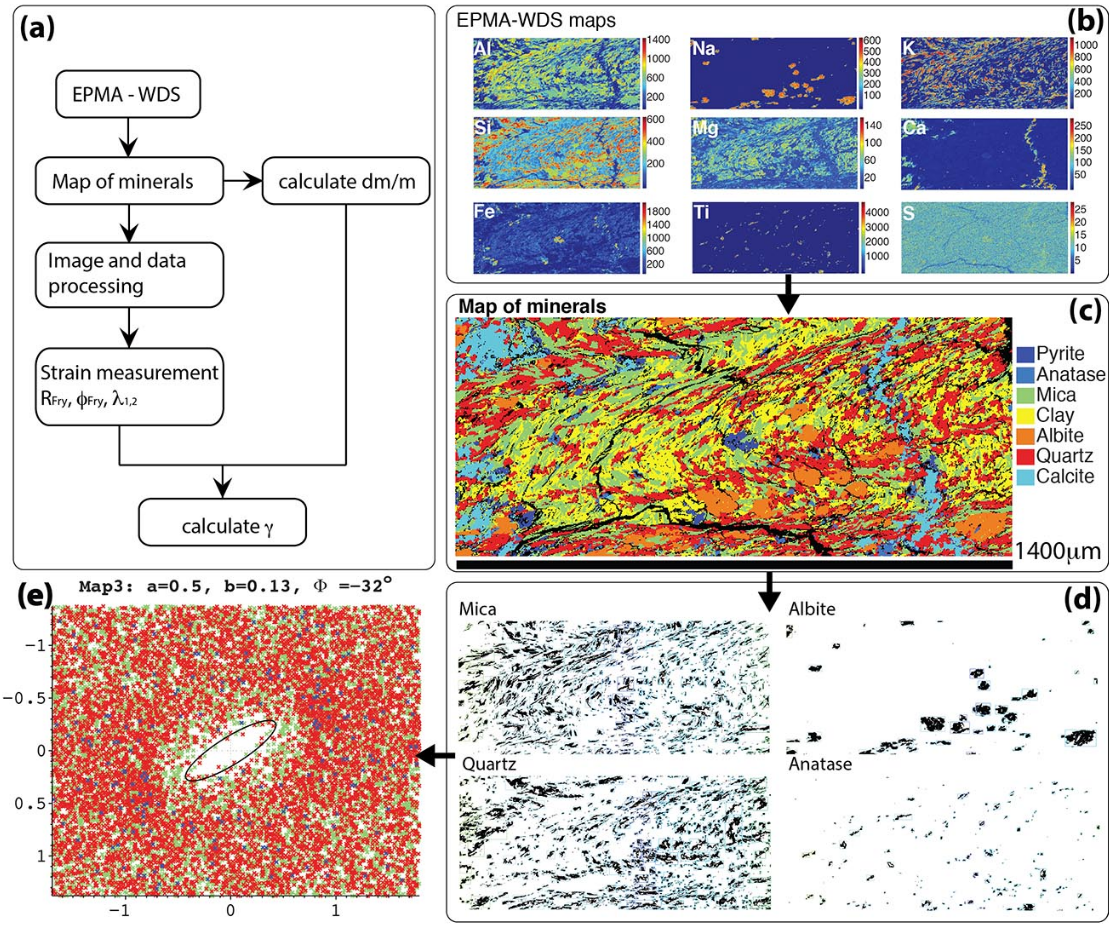

Figure A5. (a) Flowchart of the data processing technique. (b) EPMA-WDS maps of elements. (c) Map of minerals. (d) Digitized phases (binary images). (e) Fry diagram.

Appendix A2. Supplementary Information for the forward modeling

The supplementary material contains:

- A method of forward modeling of high strain and volume change in shear zones. The results of this modelling approach are presented in the section 4.2.2;
- One supplementary figure that expands the concepts presented on the Figure 10.

The model assumes homogenous deformation induced by simultaneous volume change and simple shear where θ' and α' are counterclockwise angular displacements from the shear direction (positive x-axis) (Ramsay, 1980), see **Fig. A6a**. Investigating the statistical behavior for a set of individual strain markers may provide better indicators to reconstruct the upper limit of γ values that could be measured from field data and to quantify the reliability of the strain calculated from these measurements.
The model is based on the concept that each individual set of strain vectors is chosen randomly, so that each set has the same probability of being chosen at any stage during the sampling process on natural data (e.g. measurement of grain orientation and cleavage). In this model the deformation matrix is applicable to sets of random vectors. We consider a cube that represents the initial state (**Fig. A6a**). This cube contains a cloud of one thousand points (with indices 1<i<1000 for this run) whose spatial coordinates are generated randomly in the range $0 < x_i, y_i < 1$, (or $0 < r_i < \sqrt{2}$ and $0° < \alpha_i' < 90°$ in polar coordinates). In the initial state, each point is reproduced by choosing randomly $\langle\alpha\rangle$ and its standard deviation σ before applying a strain with parameters γ and Δ. This process ensures that the input value is a homogenous white noise. However, any other input distribution is possible, such as the initial arrangement of strain markers in a rock. This initial distribution is transformed into a deformed state $\langle\alpha\rangle(\gamma,\Delta) \overset{D}{\rightarrow} \langle\alpha'\rangle(\gamma,\Delta)$. Accordingly, the average angles $\langle\alpha'\rangle(\gamma,\Delta)$ and the standard deviation $\sigma'(\gamma,\Delta)$ are calculated based on $\alpha(\gamma,\Delta)$ and $\sigma(\gamma,\Delta)$ and represented as surfaces (**Fig. A6b**, bottom plots). Because of the applied strain, each point moves to a new position x_i', y_i' by applying the deformation matrix (**Eq. 5)**. The new points are considered as a set of vectors that start from the origin (0, 0). For each vector, the angle α_i' with respect to the x-axis is calculated.

Then, the average value of the distribution of these angles, $\langle\alpha'\rangle$, and the standard deviation σ' are calculated. These calculations are performed for a large number of values of γ and Δ in the range $0 < \gamma < 100$, and $-1 < \Delta < 1$, respectively. As an example, **Figure 10a** shows the shear of a set of random vectors with $\gamma = 5, 10, 100$ and with $\Delta = +0.5, 0, -0.5$, as well as their Rose diagrams with the calculated values of $\langle\alpha'\rangle$ and σ' after applying **Eq. 5**. **Figure S1b** shows the initial state of $\langle\alpha\rangle$ and σ (upper plots) transformed into the final state $\langle\alpha'\rangle$, and σ' (lower plots). The results are presented as surfaces in the range $0 < \gamma < 100$, and $-1 < \Delta < 1$. Results show that the deformed state form contours with constant values of $\langle\alpha'\rangle$ and σ'. These iso-contours correspond to iso-angle curves and by knowing the value of Δ, γ can be determined and vice versa. Note that both values of $\langle\alpha'\rangle$ and σ' decay rapidly for $\gamma > 10$ for any Δ (**Fig. A6b**).

The relationship between the distribution of initial angles $\langle\alpha\rangle$ and that of final angles $\langle\alpha'\rangle$ after applying a deformation with parameters γ and Δ, is described by (**Eq. 9**). This equation gives an exact result in an ideal case only because angles measured in natural objects will show values of $\langle\alpha'\rangle$ and σ' that contain some noise. In order to investigate the behavior of **Eq. 9** in the presence of noise, **Eq. 9** is rearranged in the following form:

$$C_\alpha(\gamma, \Delta) = ln\left(\frac{(1+\Delta)\cdot\cot(\alpha')-\cot(\alpha)}{\gamma}\right) \qquad \text{(A1)}$$

where $C_\alpha(\gamma, \Delta)$ defines a correlation surface, which shows in an ideal case $C_\alpha(\gamma, \Delta) = \ln(1) = 0$ (**Eq. A1**) and $C_\alpha(\gamma, \Delta) \neq 0$ when some noise is present in the input data. A high correlation between noise-free and noisy input data is obtained when $C_\alpha(\gamma, \Delta) \to 0$. **Figure 10c** shows the average and the standard deviation values of the angle in **Eq. A1** where both correlation surfaces $C_{\alpha=\langle\alpha\rangle}(\gamma, \Delta) = ln\left(\frac{(1+\Delta)\cdot\cot(<\alpha'>)-\cot(<\alpha>)}{\gamma}\right) \neq 0$ and $C_{\alpha=\sigma}(\gamma, \Delta) = ln\left(\frac{(1+\Delta)\cdot\cot(\sigma'\ )-\cot(\sigma)}{\gamma}\right) \neq 0$ being strongly dependent on γ and having constant behavior with respect to Δ, when both γ and Δ are varied. Note that the values of $C_{\alpha=\langle\alpha\rangle}$ decay with γ and tend toward zero approximately for $\gamma > 30$, while the values of $C_{\alpha=\sigma}$ increase with γ. This evolution reflects the fact that the distribution of angles becomes narrower with increasing γ values because the gap between σ and σ' increases. In addition, the aspect ratio between θ' from **Eq. 8** and $\langle\alpha'\rangle$, $\theta'/\langle\alpha'\rangle$, shows similar behavior (with linear phase offset). These results demonstrate that the presence of noise in natural data has a greater effect on the calculated value of γ than on the calculated value of Δ (**Fig. A6d**).

Figure A6e shows the angle of the principal extension axis $\sqrt{\lambda_1}$ with respect to the shear direction θ' as function of the aspect ratio of the principal axis R for different values of Δ and γ. This representation is also known as the $R - \theta'$ diagram (Fossen and Tikoff, 1993). The data of the model are plotted on this diagram to validate the results obtained on the model with theoretical values. For the initial state, the angle and standard deviation $\langle\alpha\rangle \pm \sigma$ (red and pink curves, **Fig. A6e**) are scattered (as expected from a random white noise) with a wide range of σ. For the final state, the values of $\langle\alpha'\rangle \pm \sigma'$ (black and gray curves, **Fig. A6e**) are plotted individually for several γ values (γ =5, 10, 20, 30, 40, 50 and 100). In all of these cases, the values of $\langle\alpha'\rangle \pm \sigma'$ decrease systematically with R, and become progressively constant when $\gamma > 1$. In general, for a given value of γ, the values of $\langle\alpha'\rangle$ align with θ' along the theoretical values of γ contours, while σ' gradually decreases as γ increases. Note that for a given value of R, the range of θ' in the interval $(\langle\alpha'\rangle - \sigma', \langle\alpha'\rangle + \sigma')$ is not a bijective function of Δ. This fact implies that relying on measuring α'only is not sufficient to determine γ with confidence and the properties of the distribution of α' must be taken into account. As a consequence, relying on measuring only α' on natural data might be misleading when $\Delta \neq 0$. To conclude, high values of strain γ can be measured in natural data if and only if the standard deviation σ' is small when θ' or $\alpha' \rightarrow 0°$. Otherwise, if $\alpha' \rightarrow 0°$ and σ' is large, then it is postulated that the deformation is localized on a sub-grain scale and cannot be estimated from the measurement of grain alignments because either only a small proportion of the total deformation is measured or the measurements should be performed at smaller spatial scales.

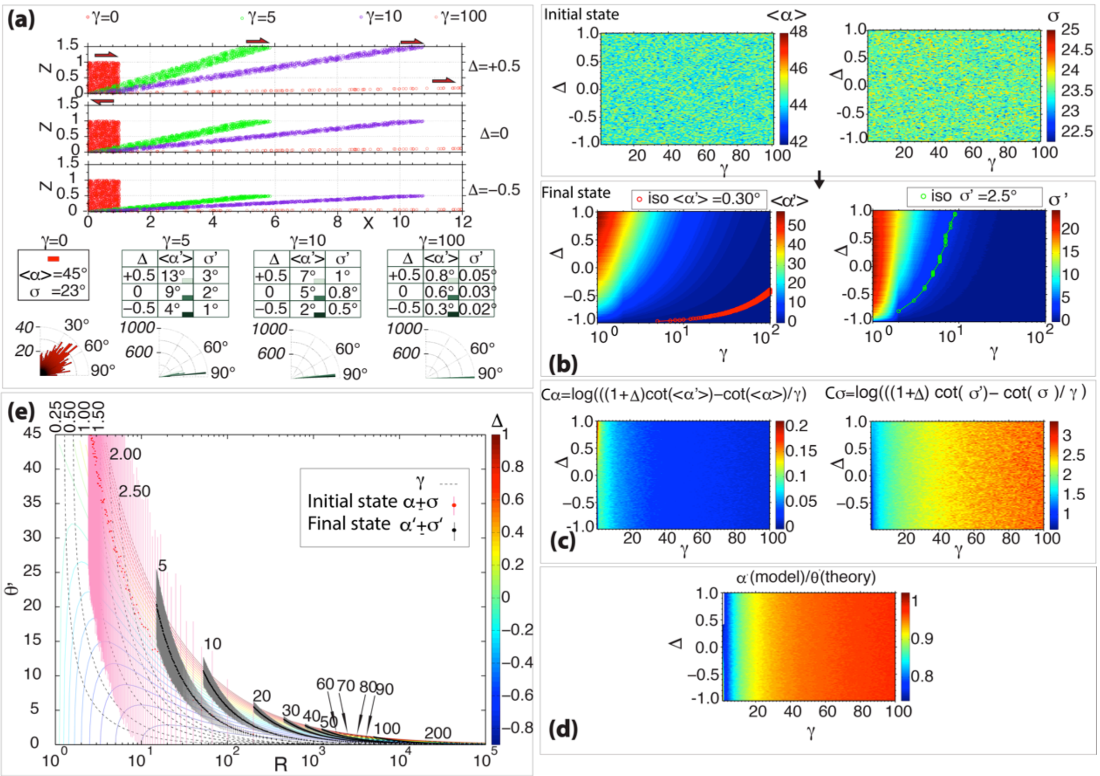

Figure A6. Forward modeling of shear zone with volume change and high shear strain values. (a) Set of random points (x, y) in the interval 0<x, y<1 deformed by simple shear γ followed by volume change Δ. (b) Top (from left to right): the initial states (before deformation) of $\langle\alpha\rangle$ and σ are represented as homogeneous random white noise and each point on these surfaces deforms with a given γ and Δ into a final state. Bottom (from left to right): the final state (after deformation) of $\langle\alpha'\rangle$ and σ' (color bars have units in degree). Both $\langle\alpha'\rangle$ and σ' decrease with increasing γ and Δ, with iso-angle contours. A natural example is plotted on these diagrams with iso-angle curves $\langle\alpha'\rangle = 0.30°$ (in red) and $\sigma' = 2.50°$ (in green). These curves display the distribution of the orientation of grain clusters that become parallel to the cleavage with very low angle with respect to the shear direction **(Fig. 7b-f)**. (c) From left to right: $C_{\alpha=\langle\alpha\rangle}(\gamma,\Delta)$ and $C_{\alpha=\sigma}(\gamma,\Delta)$ correlation surfaces. (d) Diagram of the aspect ratio between $\langle\alpha'\rangle$ from the model and θ' from theory. Note that all correlation surfaces show that the correlation increases with γ and remains constant for Δ. (e) $R-\theta'$ diagram for various values of Δ (color bar) and γ (dashed lines), with modeled data $\langle\alpha\rangle$ and θ in red and pink, and $\langle\alpha'\rangle$ and θ' in black and gray, respectively.

Chapter 4

4. Conclusions and perspectives

4.1 Main conclusions

In summary, this work has been conducted in three stages. The first stage was devoted to fieldwork and fault rocks sampling along the locked and the creeping sections of the North Anatolian Fault (NAF). Along this plate boundary between Europe and Anatolia, more than thirty outcrops were visited and sampled, providing a unique dataset of fault zone rocks. The second stage was to perform laboratory analytical measurements on these samples, including XRD, XRF, SEM, EPMA and X-ray tomography. The third stage was to build conceptual models from quantitative perspective, by using advanced strain analysis approaches and forward modeling in order to quantify the partition between seismic and aseismic displacement along the NAF. The main aims were: (1) to address the question of which parameters influence the slip mode (creep versus earthquake) along the NAF including the initial lithology of the rocks; (2) to collect evidence based on chemical analyses and structural characterization from micro scale up to the entire shear zone/tectonic scale, in order to reveal the mechanisms of creep along the NAF; (3) to propose a synthesis based on field observations at various scales that help to better understand the origin of the creeping section of the NAF; and (4) to build a conceptual model based on compactional simple shear that describes creep mechanism and its evolution in time and space. The following conclusions are derived from the two manuscripts presented in **Chap. 2 & 3**.

1 - There is a clear correlation between shallow creep and near-surface fault gouge composition. The locked fault segments contain of massive limestones without any clay gouge, while the creeping segments are located in volcanic units that show decimeter-thick clay gouges with high phyllosilicate and clay minerals content.

2 - Quantitative relationships between shear strain and mass change show how deformation mechanisms have evolved with time in the creeping zones along the North Anatolian Fault. In a first stage, solution cleavage operates in an open system with the departure of soluble species from the whole creeping zone in the early stages

of the deformation. Pressure solution and grain boundary sliding operates in a closed system at grain scale when the grain size decreases and when soluble minerals are partially removed. At a later stage of the fault zone evolution, the deformation process evolves to a mixed diffusive and friction controlled sliding. An end member mechanism involves sliding friction when the soluble minerals have been completely removed or can no longer be dissolved.

3 - The clay gouges in the creeping segments result from a progressive change of the initial volcanic rocks during their deformation by compactional simple shear. A wide damage zone is initially formed by shearing during the first stage of displacement, leading to layering development obliquely then sub-parallel to the fault that accommodates part of the aseismic displacement by pressure solution creep. Soluble minerals, mainly quartz and feldspars, are dissolved and evacuated for the most part by fluid advection out of the deforming zone during interseismic periods, leading to passive concentration of weak minerals, such as phyllosilicates, in the gouges.

4 - The finite strain measurement at various scales and with various methods led to a large range of shear strain values from $\gamma = 2.0$ when using Fry methods, up to $\gamma = 100$ when measuring cleavage sub-parallel to shear zones. A forward modeling procedure was used to simulate high shear strain (γ) coupled to mass change (Δ). It shows that both the shear angle and its standard deviation drastically decrease with increasing shear strain. Observed natural deformation can only be explained if creep zones are partitioned into parallel deformation bands with contrasting shear strain characteristics: (i) wide shear bands with cleavage oblique to the shear zone in which the Fry method may be used and gives reliable results, and (ii) narrow shear bands with cleavage planes sub-parallel to the shear zones with sub-grain shear localization in which measuring the angle of the cleavage with the shear zone is a more efficient method of evaluating the shear strain values.

5 - Finally, finite shear strain characteristics evaluated from geological analyses were used in parallel with geodetic data in order to calculate the total cumulated aseismic displacement that has been accommodated by creep. Modeling the creep behavior during the present days allows validating the model of the two types of shear zones and evaluating the maximum width of the creeping zone. Modeling the creeping behavior since the beginning of the fault sliding allows calculating an aseismic part of the total 80km displacement of 25±16% in the creeping (volcanic) zone and 0.002%

in the locked (limestone) zones, showing the crucial effect of the lithology in the seismic versus aseismic partition.

4.2 Perspectives and suggestions for further research

New perspectives of research are suggested in the following four sections that integrate the various aspects of the work presented in this PhD: field measurements, data processing and numerical modeling.

4.2.1 Improving strain field measurements in order to better compare the data at various scales

The field measurements carried out during my PhD were focused on outcrops along the fault, with sampling of damage rocks and gouges. The orientations of the various structures such as fractures and cleavages were measured in each sampling site. However, when processing the geochemical data **(Chap. 2, Fig. 7f & 10k)**, in order to evaluate the characteristics of the two Gaussian distributions that represent two different types of shear zones (associated with either low or high shear strain values), it appears that several hundred measurements of cleavage orientations are needed to better evaluate these Gaussian characteristics. Consequently, in order to better compare the data at outcrop scale (centimeters to decameters) with the data at regional scale (hectometers to kilometers), it would be necessary to measure cleavage orientations at regional scale with a very dense measurement network. Several hundred measurements of cleavage orientation should be taken, for example, from each outcrop, which is a challenging task due to the poor exposure of the outcrops.

4.2.2 Make strain measurements in 3D in order to better characterize the transition from isotropic to anisotropic rocks

In the present study, strain analyses were performed in 2D using maps of minerals. However, this analysis can be extended in 3D by performing chemical analysis using X-ray microtomography. In this case, the Fry method can be applied directly in three dimensions such that the vacancy in the center can be fitted to an ellipsoid (see **Chap. 3 §2.5.3)**. Alternatively the 2D Fry method can be made on three orthogonal planes, combining then the three ellipses into one ellipsoid. During my

PhD, several 3D images of rocks samples were acquired using high resolution X-ray microtomography at the European Synchrotron Radiation Facility in Grenoble. These data are not discussed in the two papers **(Chap. 1 & 2).** For instance **Fig. 4.1** below shows microtomography data from the two sites of Ismetpasa and Mulayim. As for the previous methods, the microstructures that appear in Ismetpasa can be characterized by the spatial distribution of the grains. The granular gouge is identified by plagioclase and quartz **(Fig. 4.1a)**, while the foliated gouge is identified by oxides **(Fig. 4.1b)**. In Mulayim, the carbonate veins network **(Fig. 4.1c)** as well as the oxide alignment along the foliation **(Fig. 4.1d)** can be distinguished. Data processing of 3D strain measurements will not just allow achieving better quantification, but will also provide a possibility to characterize the degree of anisotropy in all directions, for example by calculating the tensor of anisotropy in 3D, or by investigating the link between tensor of anisotropy and the strain tensor.

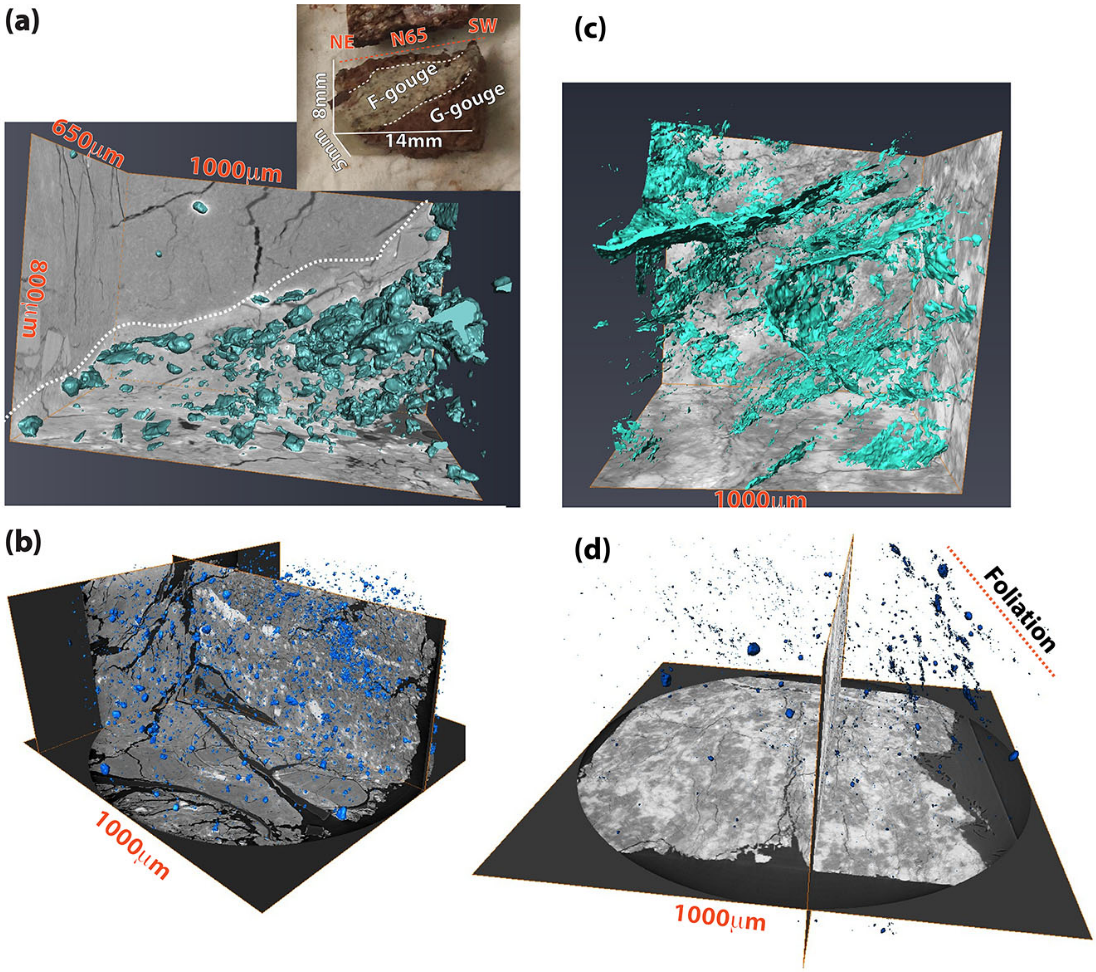

Figure 4.1 (a-b) X-ray microtomography images of a gouge sample from Ismetpasa outcrop. (a) Oriented sample with granular and foliated gouge (inset); grain of labradorite and quartz marked in green indicate the granular gouge (bottom). (b) Oxides (in blue) are dispersed in

the foliated gouge. (c-d) X-ray tomography images of a gouge sample from Mulayim outcrop. (c) Carbonate veins network marked in green. (d) Oxide particles marked in blue are aligned in the direction of the foliation in 3D.

4.2.3 Integrating physical laws in the forward modeling in order to better understand the creep process

The proposed forward modeling **(Chap. 3, §4.2.2)** can be extended by integrating physical laws. In its present state, the model only considers the strain evolution. It could be possible to integrate the stress vs. strain-rate creep relations deduced for example from ring shear experiments (Bos and Spiers, 2002) or from indenter experiments (Gratier et al., 2009). It would also be possible to integrate the fact that the development of solution seams leads to a self-organized process that localizes the dissolution along the solution seams leading to anisotropic structures (Gratier et al., 2015). Integrating such a rock anisotropy development could modify the evolution of the relations between strain values, mass change and shear displacement.

4.2.4 Quantifying the transition between isotropic and anisotropic rocks

Tectonic layering is one of the most common structural features along major faults with large displacement, usually indicating high shear strain values. Understanding the associated strain values and mass change evolution with time will help to shed light on open questions related to the seismic cycle, the evolution of shear zones and the partitioning of slip modes. The following questions could be addressed: (1) is the transition from seismic to aseismic mode controlled by structural transformations related to layering formation? (2) What is the relationship between the spacing of tectonic layering and physical parameters such as shear strain, mass change, friction and mineral composition? And how do these parameters evolve as a function of time?

These questions could be solved first by using field measurements, data processing and forward modeling that integrates physical laws. The main point is to know where the stress-driven dissolution occurs either as a diffusive process throughout the whole rock or as a very localized process along the boundary of the developing layers. Depending on the answer, the evolution from isotropic to anisotropic rocks by tectonic layering would be completely different.

Furthermore, it is possible to address this point by considering the concept of phase transition from initial rock to gouge. Layering of gouge is observed in all the outcrops of the creeping section (Kaduri et al., 2017). It is indicative of high strain localization, which can form either as a result of mechanical aggregation or chemical alteration or both (Barnhoorn et al., 2005; Gratier et al., 2015), see **Chap. 2 § 3**. The question is to know if for some shear strain values above a critical threshold $\gamma>\gamma_c$ the distribution of minerals will change from isotropic to anisotropic as a result of layering formation. It may even be suggested that the transition from seismic to aseismic behavior is correlated to a transition from isotropic to anisotropic state. If the initial distribution of minerals shows a random spatial organization, when the shear strain γ increases above a critical value γ_c, weak mineral grains will start to separate from strong mineral grains. As a result, the fault zone will develop with an alternation of layers of strong and weak grains, with high and low friction values, respectively. As most of the creep deformation occurs within the weak layers, such a mechanical transition could remind percolation models used in statistical physics (Barabási and Stanley, 1995), where a correlation length increases when a dynamical system reaches a critical point. Because stress is proportional to strain, the evolution of a correlation length ξ could be as follows:

$$\xi \sim (\gamma - \gamma_c)^{-\nu} \qquad (1)$$

where ξ is the characteristic spacing of layers in the gouge, γ is the shear strain, γ_c is the critical shear strain, and ν is a scaling exponent. When $\gamma<<\gamma_c$ the deformation is controlled by fracturing and dispersed pressure solution. Because of the isotropy of the spatial distribution of insoluble and soluble minerals the total friction will remain high and the fault will be prone to earthquakes. When $\gamma>>\gamma_c$, the differentiation of insoluble and soluble minerals will lead to the formation of a layered gouge and a stable sliding along sub-parallel weak surfaces. Evaluating the evolution of the parameters of **Eq. 1** with time will help solving this question of the transition between isotropic and anisotropic rocks.

References

Barabási, A.-L., Stanley, H.E., 1995. Fractal Concepts in Surface Growth.

Barnhoorn, A., Bystricky, M., Kunze, K., Burlini, L., Burg, J.P., 2005. Strain localisation in bimineralic rocks: Experimental deformation of synthetic calcite-anhydrite aggregates. Earth Planet. Sci. Lett. 240, 748–763. doi:10.1016/j.epsl.2005.09.014

Bos, B., Spiers, C. J., 2002. Frictional-viscous flow of phyllosilicate-bearing fault rock: Microphysical model and implications for crustal strength profiles. J. Geophys. Res. 107. doi:10.1029/2001JB000301.

Gratier, J.-P., Noiriel, C., Renard, F., 2015. Experimental evidence for rock layering development by pressure solution. Geology 43, 871–874. doi:10.1130/G36713.1

Gratier, J.-P., Guiguet, R., Renard, F., Jenatton, L., and Bernard, D. (2009) A pressure solution creep law for quartz from indentation experiments, Journal of Geophysical Research, 114, B03403, doi:10.1029/2008JB005652.

Kaduri, M., Gratier, J.-P., Renard, F., Çakir, Z., Lasserre, C., 2017. The implications of fault zone transformation on aseismic creep: Example of the North Anatolian Fault, Turkey. J. Geophys. Res. Solid Earth. doi:10.1002/2016JB013803

Appendix A1. Supplementary Information for the fieldwork, lab measurements and geological maps

	Ref. Fig. 1	Site name Outcrop location (Latitude / Longitude)	Lithology Damage rock	Damage zone description and associated microstructures
Locked section	1	Mekece 40°27'10.00"N/ 30° 3'4.00"E	Limestone Volcanic	Limestone contact with basaltic rock associated with calcite twin, tectonic stylolites and veins.
	2	Ciciler 40°26'16.68"N/ 30° 3'16.50"E	Limestone	32m wide of damage zone, in places small amount of black gouge.
	3	Taşkesti 1 40°34'5.00"N/ 31° 0'4.00"E	Limestone	~50m wide damage zone, with mirror slip surfaces and associated fractures.
	4	Taşkesti 2 40°34'54.00"N/ 31° 1'60.00"E	Limestone	Tectonic stylolites and veins.
	5	Hacisuley Manbey 40°45'15.00"N/ 30°54'39.00"E	Mélange	---
	6	Bolu 40°41'8.91"N/ 31°34'3.01"E	Limestone	Cataclastic deformation.
	7	Demirciler 40°41'44.68"N/ 31°41'27.00"E	Limestone	Mirror slip surfaces with tectonic stylolites and veins.
	8	Yenicag 40°45'31.00"N/ 31°56'35.00"E	Limestone	N/A
Creeping section	9	West of Gerede 40°47'3.00"N/ 32° 6'30.00"E	Carbonated volcanic rock	Wide fault zone with several clay gauge layers.
	10	Soplan Mha 40°56'41.00"N/ 32°32'54.00"E	Gypsum	Folding and cleavage.
	11	West of Ismetpasa (near a gas station) 40°51'55.00"N/ 32°35'41.00"E	Volcanic rock	Foliated and granular gouge zone.
	12	Hamamli 40°52'12.19"N/ 32°39'8.78"E	Serpentine	Mirror faults with cleavage and veins.
	13	East of Hamamli 40°52'22.80"N/ 32°39'55.34"E	Volcanic conglomerate	8-30cm thick clay gouge.
	14	Kabakkoy 40°55'5.27"N/ 32°58'17.62"E	Andesitic and basaltic	N/A
	15	Yazioren 40°56'1.59"N/ 33° 6'11.09"E	Mélange	20m wide shear zone with 2m thick anastomosing cleavages.
	16	East of Bayramoren 40°57'14.00"N/ 33°13'24.60"E	Mélange	N/A
	17	Sarialan 40°57'58.51"N/ 33°21'37.55"E	Mélange	50 cm anastomosing cleavage.
	18	East of Alic 40°58'51.56"N/ 33°30'4.48"E	Mélange	N/A
	19	East of Mülayim 41° 3'5.28"N/ 33°48'17.61"E	Metabasite and Ophiolitic mélange	50 cm clay gouge?

Table A1. Locations of available outcrops along the North Anatolian Fault that have been investigated in the present study including: location, lithology, fault architecture and microstructure. Height outcrops are located on locked segments, and eleven outcrops are located on the Ismetpasa creeping segment. The outcrops are indicated as white spots in the Figure 1 with their reference numbers.

Symbol	Unit	Age
Q*	Quaternary deposit	Upper Pleistocene - Holocene
Pl3*	Conglomerate, sandstone unit	Pleistocene
Mi1	Sandstone-conglomerate and siltstone unit	Lower Miocene
Mi4	Dacite, andesite and basalt unit	Middle- upper Miocene
Mi5	Basalt unit	Upper Miocene
Mi6	Andesite unit	Middle- upper Miocene
Mi7*	Agglomerate tuff unit	Middle- upper Miocene
T6	Sandstone, shale and conglomerate unit	Upper Lutetian - upper Eocene
T7*	Andesitic and basaltic unit	Upper Lutetian - upper Eocene
M1*	Ophiolitic mélange	Aptian? - Lower Senonian
M2*	Sandstone shale unit	Lower and middle Eocene
M3*	Peridotite unit	Mesozoic
MaPa*	Limestone unit	Mastrichtian and Paleocene
G	Granite unit	-
Sn1	Pyroclastic rock-lava (andesite-basalt) unit	Campanian
Sn2	Andesite unit	Campanian and Maastrichtian
Sna*	Limestone, detrital rock, volcanic rock sometime mélange with ophiolitic rock	Lower Senonian
UK2	Shale unit	Upper Cretaceous
UK3*	Sandstone, shale, agglomerate, lava, red clayey limestone tuffite unit	Albian to lower Senonian
JKk1*	Limestone unit	Upper Jurassic and lower Cretaceous
J1	Sandstone-shale-pyroclastic rock unit	Lower-middle Jurassic
Kb*	Basalt unit	Upper Cretaceous
K*	Sandstone shale unit	Lower and upper Cretaceous
TRJ*	Schist, marble and metabasite unit	Palaeozoic?, Triassic, lower and middle Jurassic
GJ	Granitoid unit	Palaeozoic - Jurassic
PTra	Sandstone- siltstone and conglomerate unit	Permian and Triassic
D	Dolomitic limestone and clayey limestone unit	Devonian
D1	Conglomerate and siltstone unit	Lower Devonian
SD	Limestone and sandstone-shale units	Sillurian - Ordovian
OS	Sandstone and conglomerate unit	Sillurian - Ordovian
Of1	Ultramafic and tectonic units	-

Table A2. Geological units found in outcrops along the North Anatolian Fault. Their symbols, lithological units and age are recompiled from the 1/100,000 geological map (Herece and Akay, 2003). The mark * refer to units that have been sampled.

#	Label	Name of area	Site name
1	H24a1	ADAPAZARI	Mekece, Ciciler
2	G25c3	ADAPAZARI	
3	G26d4	ADAPAZARI	Taskasti
4	G25c2	ADAPAZARI	
5	G27d1	BOLU	Bolu
6	G27d2	BOLU	Demirciler
7	G27c2	BOLU	
8	G25b3	ADAPAZARI	Hacisuley Manbey
9	G27b3	BOLU	Yenicag
10	G28a4	BOLU	Before Grede
11	G28a3	BOLU	
12	G29a4	BOLU	Gas-Station-1, Ismit Pasa
13	G29a3	BOLU	Hamamili , Ismit Pasa
14	G29a1	BOLU	Solan-Mha
15	G29a2	BOLU	
16	G30a2	CANKIRI	
17	G30b1	CANKIRI	
18	G31a1	CANKIRI	
19	G31a2	CANKIRI	
20	F31d4	KASTAMONU	
21	F31d3	KASTAMONU	
22	F31c4	KASTAMONU	
23	F31c3	KASTAMONU	
24	F32d4	KASTAMONU	
25	F32d3	KASTAMONU	
26	F32c4	KASTAMONU	
27	F32c3	KASTAMONU	

Table A3. List of geological maps 1/25,000 used during fieldwork.

Date	Location	Hand sample	Description	Thin section	XRD	XRF	SEM	EPMA
27.10.2013	West of Gerede	1	Green gouge		✓			
		2	Red gouge		✓			
		3	White gouge		✓			
		4	80N, N110	BG4A, BG4B	✓		✓	
05.10.2014	West of Gerede	1	N135/80S	WG1	✓		✓	
		2	N95/Vertical	WG2	✓		✓	
		3	N95/Vertical	WG3	✓		✓	
		4	N105/Vertical	WG4	✓		✓	
		5*	N105/Vertical	WG5a, WG5b	✓		✓	
		6	N130/Vertical	WG6	✓		✓	
		7	N50-65SE/65	WG7	✓	✓	✓	✓
		8	Green Gouge		✓			
		9	N65/N70	WG9	✓		✓	
		10	N75/Vertical (Block)	WG10	✓		✓	
		11	Rigid block		✓			
		12	Rigid block	WG12	✓		✓	
		13	SE/N130	WG13R	✓		✓	
		14	N165	WG14L	✓	✓	✓	✓
	Lower part	1*	N108/10E	WG1T		✓	✓	
		2*	N108/10E	WG2T				
		3*	N108/10E	WG3T		✓		
		4*	N108/10E	WG4T				
	West of Gerede	15*	N112/WE 10E fault surface N100/N70	WG15T	✓			
20.5.2015	West of Gerede	16*	N95/70; gouge	WG16a	✓			
	Gas station Q		W-E N90, vertical	GS1H1, GS1H2, GS1V				
	Gas	1*	N65	Gas1	✓		✓	✓

	station							
		2*	N60/80	Gas2	✓			
		3*	170N	Gas3	✓		✓	✓
		4*	N50	Gas4	✓		✓	✓
28.10.2013	Hamamili	1*	N90, vertical	HA1A, HA1B	✓	✓	✓	✓
		2*	N90, EW oblique lineation		✓		✓	
		3	70N, parallel to the cleavage	HA3H	✓			
		4*	N60/vertical; parallel (vertical) to the cleavage	HA4A, HA4B	✓			
		5	N105, Vertical	HA5H1, HA5H2, HA5V				
05.10.2014	Hamamli	1	N70/vertical gouge		✓			
		2	N70/Vertical gouge		✓			
		3	N70	HA3	✓	✓	✓	
07.10.2014	Hamamli	4*	N60/NE5 fault 60/SE65; gouge	HA4T	✓	✓	✓	
		5	hard	HA5	✓			
		6	N35/vertical		✓			
		7	highly deformed		✓			
		8	soft		✓			
		9	hard		✓			
		10	white		✓			
		11*	pulverized rock	HAP1, HAP2	✓			
06.10.2014	Bayrmoren	1*	cleavage N100, N105, N110	BA1	✓			
		2*	cleavage	BA2				

			N100,N105, N110					
	Yaziran	3*	cleavage N100, N105, N110	BA3a, BA3b	✓	✓	✓	
07.10.2014	Kabakkoy	1	60/Vertical	KA1				
		2*	70/85S grey gouge contact N70/70S	KA2				
		3*	N60/SW60 cleavage	KA3				
08.10.2014	East of Mulayim	1*	N60/50N	MU1		✓		
		2*	N65/horizontal	MU2T	✓	✓		
09.10.2014	East of Alic	1	parallel cleavage		✓			
	Sarialan	1*	cleavage with striation	SA1	✓	✓	✓	
		2*	65/N70	SA2				

Table A4. List of hand samples along the creeping section with location in the corresponding outcrop (see Table 1) and indication on which part of the fault they were collected (gouge, damage zone, and host rock). The rock composition was obtained from XRD analyses. The micro-scale observations are listed (SEM, XRF imaging, EPMA). The symbol * correspond to samples that were consolidated with epoxy glue.

Name	Dimensions [mm] x [mm]	Spot size [µm]	Dwell time [msec]	X,Y [µm]
BA3a	13.2 x 10.3	30	500	26
BA3a ALL	50.5 x 39.4	100	400	99
BA3b	15 x 11.7	30	500	30
MU2T-good	13.6 x 10.6	30	500	27
WG3T	13.0 x 10.1	30	500	26
SA1	14.0 x 11	30	500	28
HA3	14.6 x 11.4	30	500	29
HA4T	14.3 x 11.1	30	500	28
MU1	10.8 x 8.4	30	400	21
MU1 UP	39.4 x 30.8	100	400	77
MU1 Down	39.4 x 30.8	100	400	77
WG1T	14.6 x 11.4	30	500	29
Gas1 -map1	13.8 x 10.8	30	300	27
Gas1 -map2	13.6 x 10.6	30	300	27
Gas1 -map3	13.6 x 10.6	30	300	27
Gas1 -map4	13.6 x 10.6	30	300	27
WG07	43.9 x 34.3	100	500	86
WG14	18.2 x 14.2	30	200	36
HM1A	8.1 x 6.3	30	300	16

Table A5. List of samples imaged using X-ray fluorescence mapping (voltage 20kV and current 300 µA).